

In the format provided by the authors and unedited.

Deep glacial troughs and stabilizing ridges unveiled beneath the margins of the Antarctic ice sheet

Mathieu Morlighem  ^{1*}, Eric Rignot  ^{1,2}, Tobias Binder³, Donald Blankenship⁴, Reinhard Drews  ^{3,5}, Graeme Eagles  ³, Olaf Eisen  ^{3,6}, Fausto Ferraccioli⁷, René Forsberg⁸, Peter Fretwell⁷, Vikram Goel  ⁹, Jamin S. Greenbaum  ⁴, Hilmar Gudmundsson  ¹⁰, Jingxue Guo¹¹, Veit Helm³, Coen Hofstede³, Ian Howat¹², Angelika Humbert  ^{3,6}, Wilfried Jokat  ³, Nanna B. Karlsson  ^{3,13}, Won Sang Lee  ¹⁴, Kenichi Matsuoka  ¹⁵, Romain Millan¹, Jeremie Mouginot  ^{1,16}, John Paden¹⁷, Frank Pattyn  ¹⁸, Jason Roberts  ^{19,20,21}, Sebastian Rosier¹⁰, Antonia Ruppel²², Helene Seroussi  ², Emma C. Smith  ³, Daniel Steinhage  ³, Bo Sun¹¹, Michiel R. van den Broeke  ²³, Tas D. van Ommen^{19,20,21}, Melchior van Wessem  ²³ and Duncan A. Young  ⁴

¹Department of Earth System Science, University of California, Irvine, CA, USA. ²Jet Propulsion Laboratory, California Institute of Technology, Pasadena, CA, USA. ³Alfred Wegener Institute Helmholtz Centre for Polar and Marine Research, Bremerhaven, Germany. ⁴Jackson School of Geosciences, UT Austin, Austin, TX, USA. ⁵Department of Geosciences, University of Tübingen, Tübingen, Germany. ⁶University of Bremen, Bremen, Germany.

⁷British Antarctic Survey, Cambridge, UK. ⁸Technical University of Denmark, Kongens Lyngby, Denmark. ⁹National Centre for Polar and Ocean Research, Vasco, Goa, India. ¹⁰Northumbria University, Newcastle upon Tyne, UK. ¹¹Polar Research Institute of China, Shanghai, China. ¹²School of Earth Sciences, Ohio State University, Columbus, OH, USA. ¹³Geological Survey of Denmark and Greenland, Copenhagen, Denmark. ¹⁴Korea Polar Research Institute, Incheon, South Korea. ¹⁵Norwegian Polar Institute, Tromsø, Norway. ¹⁶Institut des Géosciences de l'Environnement, CNRS, Université Grenoble Alpes, Grenoble, France. ¹⁷Center for Remote Sensing of Ice Sheets, University of Kansas, Lawrence, KS, USA. ¹⁸Université libre de Bruxelles, Brussels, Belgium.

¹⁹Australian Antarctic Division, Kingston, Tasmania, Australia. ²⁰Antarctic Climate & Ecosystems Cooperative Research Centre, Tasmania, Australia.

²¹Institute for Marine and Antarctic Studies, University of Tasmania, Hobart, Tasmania, Australia. ²²Federal Institute for Geosciences and Natural Resources, Hanover, Germany. ²³Institute for Marine and Atmospheric Research, Utrecht University, Utrecht, Netherlands. *e-mail: Mathieu.Morlighem@uci.edu

Supplementary Information for

Deep glacial troughs and stabilizing ridges unveiled beneath the margins of the Antarctic ice sheet

M. Morlighem et al.

correspondence: mathieu.morlighem@uci.edu

This PDF file includes:

1	Mapping method and error estimation	2
1.1	Important notes	2
1.2	Data	2
1.3	Fast flowing sectors	4
1.4	Slow moving sectors	6
1.5	Ice-free land	7
1.6	Ocean bathymetry	7
1.7	Ice Shelf thickness	7
1.8	Mosaicking	8
2	Error Analysis	9
2.1	Fast flowing sectors	9
2.2	Slow moving sectors	9
2.3	Ice-free land	9
2.4	Ocean bathymetry	9
2.5	Cavities under ice shelves	9
3	Sea level potential	10
4	BedMachine Antarctica v1 dataset	15
5	Comparison with existing datasets	15
5.1	Comparison with Bedmap2	15
5.2	Local slopes and roughness	69
5.3	Marine Ice Sheet Instability	69
Bibliography		71

1 Mapping method and error estimation

1.1 Important notes

In BedMachine Antarctica, all heights are referenced to mean sea level (using the geoid EIGEN-6C4). To convert the heights to heights referenced to the WGS84 ellipsoid, simply add the geoid height using the geoid provided in the netCDF file:

$$z_{\text{ellipsoid}} = z_{\text{geoid}} + \text{geoid} \quad (\text{S1})$$

The surface elevation and ice thickness are in *ice equivalent* as they include a firn air content correction. The elevation of the top of the snow, which is provided by REMA [Howat *et al.*, 2019], can be calculated by adding the firn depth correction provided in the netCDF:

$$s = s_{\text{BedMachine}} + d_{\text{firn}} \quad (\text{S2})$$

1.2 Data

We use different mapping methods depending on the region as shown in figure S1.

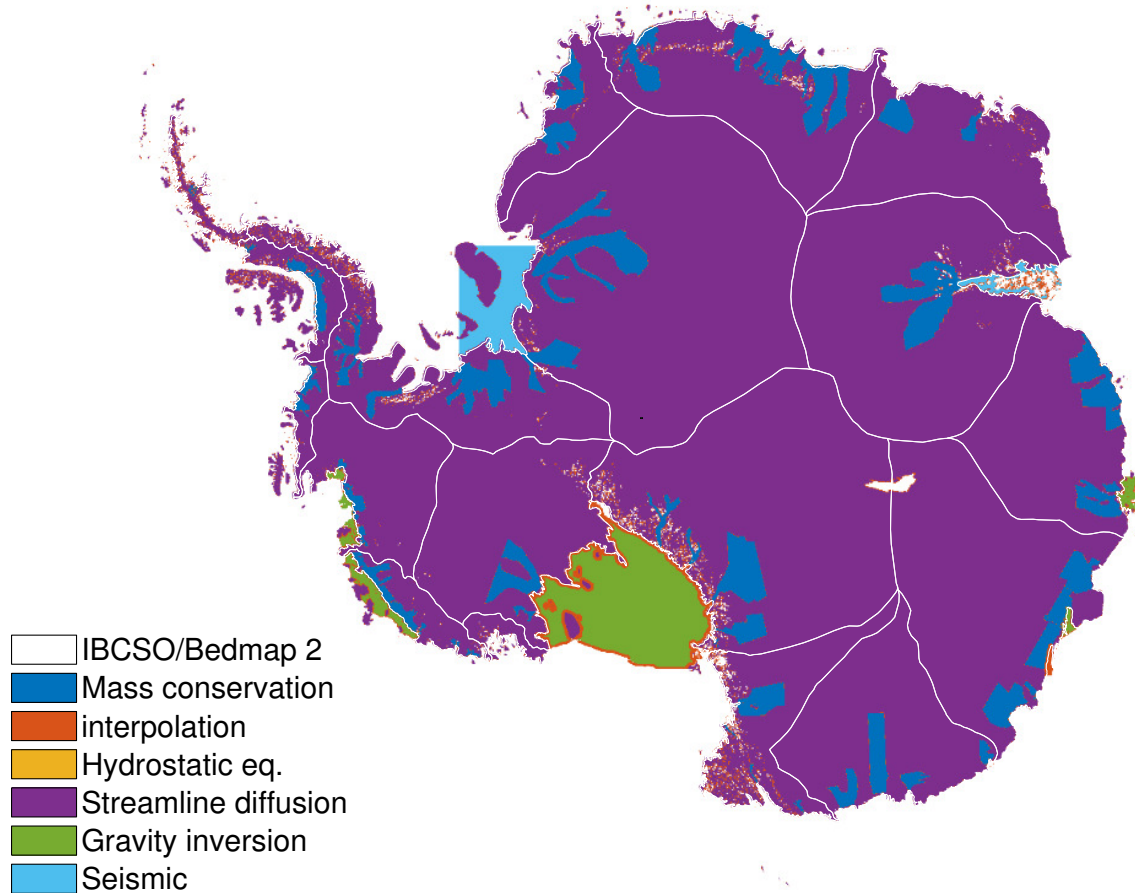


Figure S1: Bed mapping method

Figure S2 shows the flight lines for which we have radar derived ice thickness data available to constrain the mapping of the ice thickness and bed topography. Figure S3 shows in color the new lines of radar data that are used in BedMachine v1 that were not available when Bedmap2 was being developed.

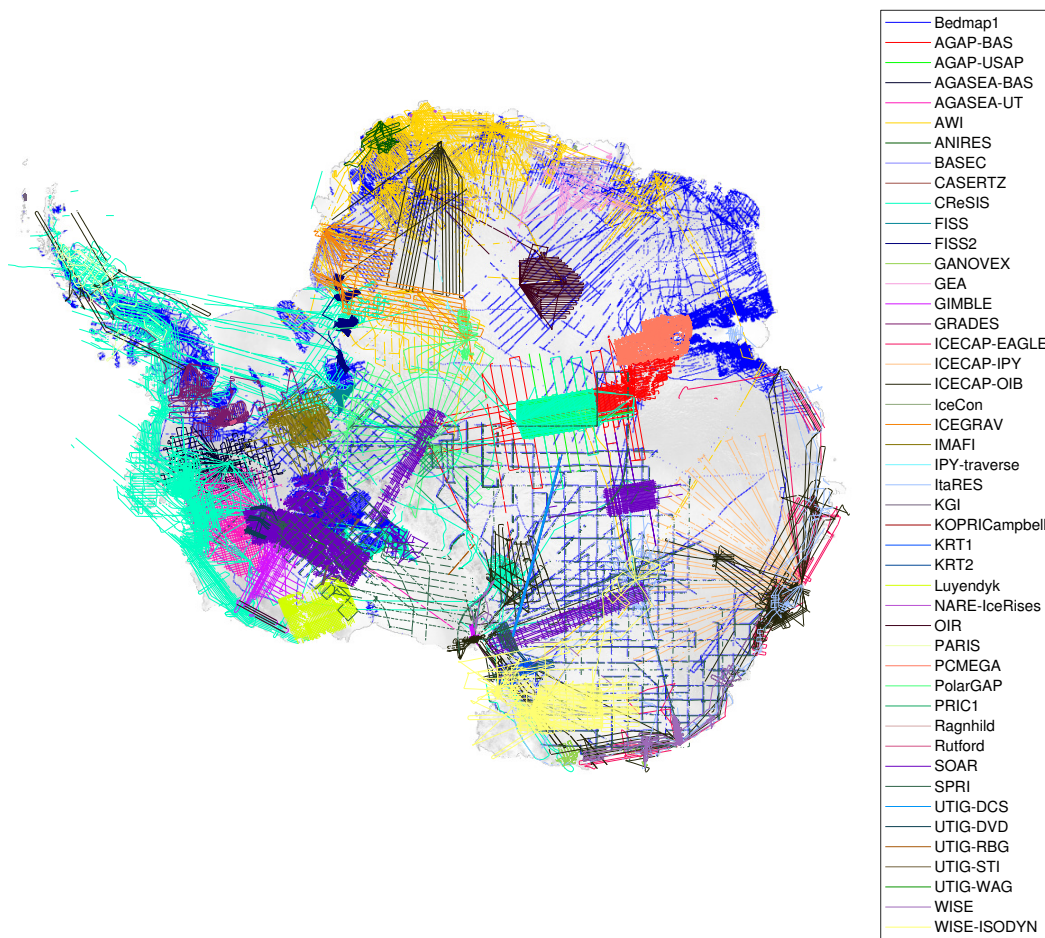


Figure S2: Ice thickness data from airborne radar used in BedMachine Antarctica v1

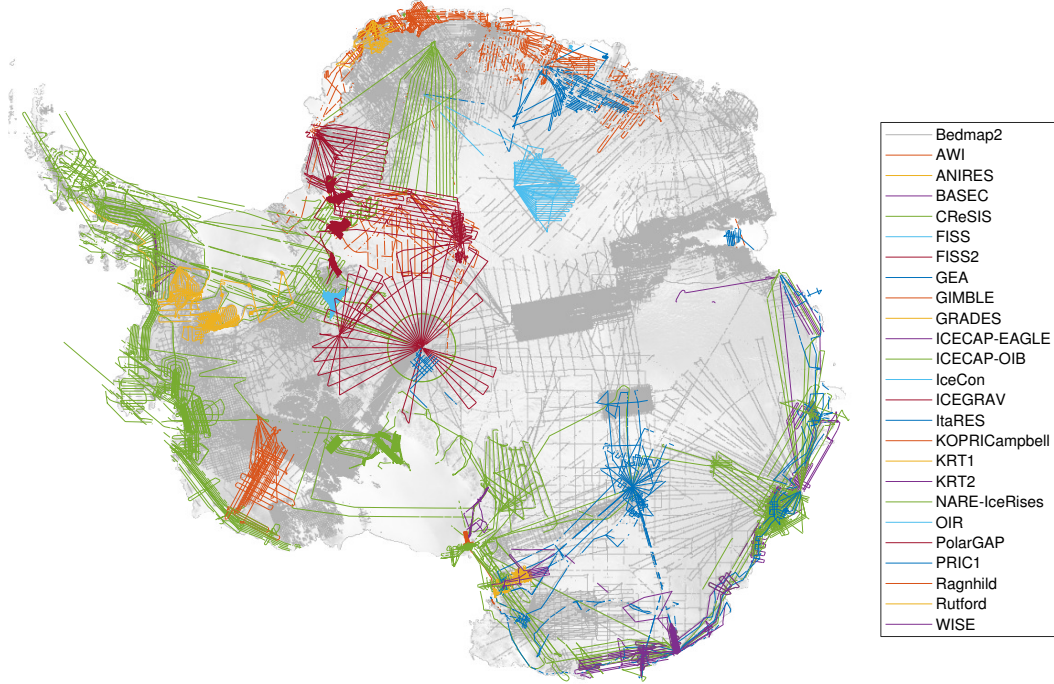


Figure S3: New ice thickness data (color) collected since Bedmap2 (grey)

1.3 Fast flowing sectors

In the region of fast flow (ice surface velocity > 50 m/a) we use the method of conservation of mass that has been extensively detailed in *Morlighem et al.* [2011, 2014b, 2017]. We just mention here the main ideas. Using ISSM [*Larour et al.*, 2012], we solve for the ice thickness that satisfies the conservation of mass [*Morlighem et al.*, 2011, 2014b]:

$$\begin{cases} \nabla \cdot H \bar{\mathbf{v}} = \dot{a} & \text{in } \Omega \\ H = H_{obs} & \text{on } \Gamma_- \end{cases} \quad (\text{S3})$$

where Ω model domain, Γ_- inflow boundary, $\bar{\mathbf{v}}$ depth-averaged ice velocity, H , H_{obs} : modeled and measured ice thickness, and $\dot{a} = \dot{M}_s - \dot{M}_b - \partial H / \partial t$ apparent mass balance.

To account for all measurements of ice thickness, H_{obs} along flight tracks, T , that lie within the model domain Ω , we formulate an optimization problem, where the following cost function must be minimized:

$$\mathcal{J}(\bar{\mathbf{v}}, \dot{a}) = \int_T \frac{1}{2} (H - H_{obs})^2 dT + \int_{\Omega} \gamma_{\parallel} (\nabla H \cdot \mathbf{n}_{\parallel})^2 d\Omega + \int_{\Omega} \gamma_{\perp} (\nabla H \cdot \mathbf{n}_{\perp})^2 d\Omega \quad (\text{S4})$$

where \mathbf{n}_{\parallel} and \mathbf{n}_{\perp} are unit vectors parallel/perpendicular to ice velocity, γ_{\parallel} and γ_{\perp} are constant regularization parameters. We generally choose $\gamma_{\perp} \simeq 10 \times \gamma_{\parallel}$ to preserve gradients across flow, that are often stronger than along flow. To calibrate these regularization parameters, we perform an L-curve analysis [*Hansen*, 2000] for each basin.

Here, we use the InSAR-derived ice surface velocities from *Rignot et al.* [2011], which is posted at 150 m and has errors in speed of ~ 10 m/a and 1.5° in flow direction. Note that, as in BedMachine Greenland [*Morlighem et al.*, 2017], we are using *surface* velocities and not *depth-averaged* velocities. We apply mass conservation only in fast flowing regions (> 50 m/a), where sliding speeds account for a significant portion of the total ice velocity. Internal deformation is also not well constrained as it depends on geothermal heat flux, which is highly uncertain. Based on an Antarctic-wide ice sheet model designed for ISMIP6 [*Seroussi et al.*, 2019], we find that depth-averaged velocities are less than 5% smaller than surface velocities in these

Acronym	Companion name	Institution(s)	Reference(s)	Contact	URL
BedMap	Bedmap 1	BAS	Lüthi and Faugeron 2001 Ferracci et al. 2011	Peter Fretwell Flavia Ferracci	https://icecore.ac.uk/Data_research/databases/bedmap/database/
AGAP-PS	Antarctic's Gamburtsev Province - USAP	BAS	Bur et al. 2011	Robin Bell	https://icecore.ac.uk/icecore/
AGASEA-SAS	Antarctic Geophysical Survey of the Amundsen Sea Embayment, Antarctica	BAS	Vanguard et al. 2006	François Forgette	https://icecore.ac.uk/icecore/
AGASEA-II	Antarctic Geophysical Survey of the Amundsen Sea Embayment, Antarctica	UTIG	Held et al. 2008a	Ivan Holt, Duncan Young	https://icecore.ac.uk/icecore/
ANARES	Antarctic network of ice shelves sounding	AM + MPR (05/06) + BGR (11-12)	Werner et al. 2019; Rödig et al. 2012; Nogu et al. 2013	Old Eise, Daniel Stenberg	https://doi.pangaea.de/10.1594/PANGAEA.896598
ANARES	ERICA, PRO, GE, USA, MARIBAO, SEA, IBI, MEGAS	AWI	Kotzen et al. 2014; Smith et al. 2013 (in prep)	Elmar Simmler, Old Eise	https://doi.pangaea.de/10.1594/PANGAEA.923211
RECSL	Recovery Glaciers, Antarctica	AWI	Hemmer et al. 2018	Angela Hartnett, Daniel Steimann	https://doi.pangaea.de/10.1594/PANGAEA.920451
VSA	westernmost central Transantarctic Mountains	AWI	Rödig et al. 2012	Gemma Etches	-
BASC-E	English Coast Radar Survey	UNIS	currenly no reference , doi to be created by Gudmundsson	Hilmar Gudmundsson	https://doi.pangaea.de/10.1594/PANGAEA.920200
BAERSTZ	Cenozoic Aerogeophysics of the Southeastern Ross Transition Zone	KU	Bannister et al. 2001	Donald Bannister	https://doi.pangaea.de/10.1594/PANGAEA.905972
CBESS	Center for Remote Sensing of Ice Sheets	BAS/AM	Craswell et al. 2016 (digital media)	John Paden	https://doi.pangaea.de/10.1594/PANGAEA.905972
FRIES	Former Ice Shelf System Pantry (mostly seismic)	BAS/JNN	Rödig et al. 2018	Sebastien Rosier, Caren Hothode	https://doi.pangaea.de/10.1594/PANGAEA.905972
FRISS2	Former Ice Shelf System bed, airborne radar	BGR	currently no reference , doi to be created by Gudmundsson	Hilmar Gudmundsson	https://doi.pangaea.de/10.1594/PANGAEA.920200
GANOVEX	German Antarctic Korn Vorkommen Land Expeditions	BGR/AM	Denn 2004	Verner Dam	-
GEIA	Geodynamic evolution of East Antarctica	UTIG	Ergo et al. 2018	Duncan Young	http://www.nau.edu/~dsteimann/icefa/utig03/01.html
GIMBLE	Geophysical Investigations of New Byrd Land Evolution	BAS?	Long et al. 2013; Young et al. 2016	Young et al. 2011	http://www.nau.edu/~dsteimann/icefa/utig03/01.html
GRADES	Global Retreat in Antarctica and Deglaciation of the Earth System	UTIG/AAD	Ross et al. 2012	John Paden	https://doi.pangaea.de/10.1594/PANGAEA.905972
IGEAC-EGLE	East Antarctic Grounding Line Experiment	UTIG/AAD/NERC	Bannister et al. 2001	Sebastien Rosier, Caren Hothode	https://doi.pangaea.de/10.1594/PANGAEA.905972
IGEAC-HPY	IGCapability, Autonome Radar Sounder, NERC Campaign	UTIG/AAD/NERC	Young et al. 2011	Hilmar Gudmundsson	https://doi.pangaea.de/10.1594/PANGAEA.905972
IGECAR-JOB	IGCapability, Autonome Radar Sounder, Operation Ice Bridge	UTIG/AAD/NERC	Bannister et al. 2013	Verner Dam	-
IGECAR-VB	IGCapability, Autonome Radar Sounder, Operation Ice Bridge	UTIG/AAD/NERC	Denn 2004	Duncan Young	http://www.nau.edu/~dsteimann/icefa/utig03/01.html
Icecom/BaWise	Icecom/BaWise	ULB	Ergo et al. 2018	Young et al. 2011	http://www.nau.edu/~dsteimann/icefa/utig03/01.html
IPY-Traverse	Deutsche Ice-Raeumende Maud Land, Antarctica	NPI	Dowd et al. 2015; Berger et al. 2016	Jack Kotler	https://doi.pangaea.de/10.1594/PANGAEA.905972
ISRES	Italian RES data	NPI/PA	Langley et al. 2011	Silvano Ibari	-
KR1	K-Route survey	KOHRUUTG	Langley et al. in prep	Wen-San Lee	-
KR2	K-Route survey	USBSLUTG	Langley et al. in prep	Wen-San Lee	-
Luyendijk	Eastern margin of the Ross Sea rift in western Marie Byrd Land, Antarctica	UPEB/LUTG	Langley et al. in prep	Bruce Luyendijk	https://doi.pangaea.de/10.1594/PANGAEA.905972
NARE-sites	Norwegian Antarctic Research Expeditions Ice Rises	UPEI	Langley et al. in prep	Ylva Götlund	https://doi.pangaea.de/10.1594/PANGAEA.905972
OIR	Office of Polar Programs	AWI	Goel et al. 2017	Koen Matsuka	https://doi.pangaea.de/10.1594/PANGAEA.891323
PARIS	Part of the Advanced Radar Ice Sounder	Johns Hopkins	Kortens et al. 2018	Old Eise, Daniel Steimann	https://doi.pangaea.de/10.1594/PANGAEA.905972
PausGAP-ESA	PausGAP	BAS/DTU/DTU	Reid et al. 2010	John Roney	https://doi.pangaea.de/10.1594/PANGAEA.891323
PausGAP-ES	PausGAP	NPI/PA/SOTU	Jordan et al. 2018; Winter et al. 2018; Paxman et al. 2019	François Forgette	https://doi.pangaea.de/10.1594/PANGAEA.905972
POMEGA	Prince Charles Mountains Expedition of Germany and Australia	AADC	Droz et al. 2013; Froberg et al. 2018	Koen Matsuka	https://doi.pangaea.de/10.1594/PANGAEA.905972
PRICE1	SHICeCAP (Tian Doma)	AMC/UTIG/PRC	Alison and Hynd 2010	Ian Alison	https://researchdata.mimas.ac.uk/autumnice/autumnice-datasets/01.html
Rephind		BAS/PAW/UTIG/ULB	Benn et al. in prep	Duncan Young, James Greenbaum	https://doi.pangaea.de/10.1594/PANGAEA.882329
Rutherford		Cullen et al. 2015	Cullen et al. 2015	Koen Matsuka	https://doi.pangaea.de/10.1594/PANGAEA.882329
SOAR	Support Office for Aerogeophysical Research	EDW/UTIG/DE/OUFS	Koen Matsuka	Edwin King	https://doi.pangaea.de/10.1594/PANGAEA.882329
SPIR	Scott Polar Research Institute	BAS/OUFS/UTIG/UTIG/UNIS	Bennetts et al. 2001; Carter et al. 2007; Studinger et al. 2004; Studinger et al. 2007	Douglas Blankenship, Duncan Young	https://doi.pangaea.de/10.1594/PANGAEA.882329
UTIG-DPS	Deep Continental Structure Survey	UTIG	Dewey et al. 1980	Edwin King	https://doi.pangaea.de/10.1594/PANGAEA.882329
UTIG-DO	WAS Ice-Disk Migration Survey	UTIG	Held et al. 2006b	Duncan Young	https://doi.pangaea.de/10.1594/PANGAEA.882329
UTIG-RBG	Robust Glaciological Survey	UTIG	Masterson et al. 2010	Duncan Young	https://doi.pangaea.de/10.1594/PANGAEA.882329
UTIG-SM	Seismic Tomography Ice Sheet Shear Margin Survey	UTIG/OSU	Unpublished	Duncan Young	https://doi.pangaea.de/10.1594/PANGAEA.882329
UTIG-WAG	West Antarctic Geology Survey	UTIG/GSC	Unpublished	Duncan Young	https://doi.pangaea.de/10.1594/PANGAEA.882329
WISE-ISODYN	Warm Isobath/Thermodynamic Mountain System Exploration-Icehouse Earth Stability or Dynamism	UCP/L	Borchardt et al. 2005	Edmund, Tongyu Guo	https://doi.pangaea.de/10.1594/PANGAEA.882329
			McMurdo et al. 2014	Fabio Ferracci	https://doi.pangaea.de/10.1594/PANGAEA.882329
			Jordán et al. 2010		

Table S1: Ice thickness and ocean bathymetry data source used in BedMachine Antarctica v1

regions, which to a first order translates into a 5% error in ice thickness, which is below our error estimate. We do account for potentially lower speeds in the optimization sequence, and radar-derived ice thickness data help correct for a potential bias. The reason why we are not relying on an ice flow model is twofold. First, to run a numerical ice sheet model, we would need to assume that the bed topography is known and there would therefore be a consistency issue between the inferred bed from MC and the velocities calculated by the ice sheet model. Second, we observed that velocity directions from numerical models can deviate significantly from the observed velocities, which leads to a larger misfit to radar-derived ice thickness. In the future, we plan on using the ratio between surface velocities and depth-averaged velocities as a way to address this problem.

The surface mass balance (SMB) is from RACMO2.3p2, averaged for the years 1979-2011 [*van Wessem et al., 2018*], with an accuracy of 7% for the time-average fields. The thickening rate is assumed to be zero except in the Amundsen sea embayment where we use altimetry data from ATM and ICESat to estimate it.

The optimization is constrained by radar sounder data collected by various institutions (see figure S2) acquired between the 1970s and 2017. An exhaustive list of the data used in the optimization is shown Table S1.

From the calculated ice thickness, we derive the bed by subtracting it from the REMA surface digital elevation model [*Howat et al., 2018, 2019*].

1.4 Slow moving sectors

In slow moving regions, ordinary Kriging [*Deutsch and Journel, 1997*] or thin plate splines are generally employed (e.g., *Bamber et al. [2001]*; *Fretwell et al. [2013]*; *Bamber et al. [2013]*; *Morlighem et al. [2017]*). While convenient, these methods do not capture the intrinsic anisotropy of the ice thickness that mass conservation requires: as ice is transported downstream, ice thickness varies slowly along flow. Significantly higher gradients in ice thickness are expected across flow. In order to account for the asymmetry, we developed a new method based on a diffusion equation: we find the ice thickness, H , such that:

$$\begin{cases} \nabla \cdot \mathbf{D} \nabla H = 0 & \text{in } \Omega \\ H = H_{obs} & \text{on } T \end{cases} \quad (\text{S5})$$

where \mathbf{D} is an anisotropic diffusion tensor defined as:

$$\mathbf{D} = \mathbf{v}_s \otimes \mathbf{v}_s + \tau \mathbf{I} \quad (\text{S6})$$

where $\tau = 30^2 \text{ m}^2/\text{yr}^2$, if the ice velocity is greater than 30 m/a, or scalar (i.e., isotropic) in the regions where the velocity is undefined or less than 30 m/a. This equation is not based on physics, it is a way to interpolate ice thickness between flight lines anisotropically. Figure S4 shows an example of streamline diffusion applied to Upernivik in western Greenland. The trough are well preserved, and the over shape of the bed more realistic than with ordinary Kriging.

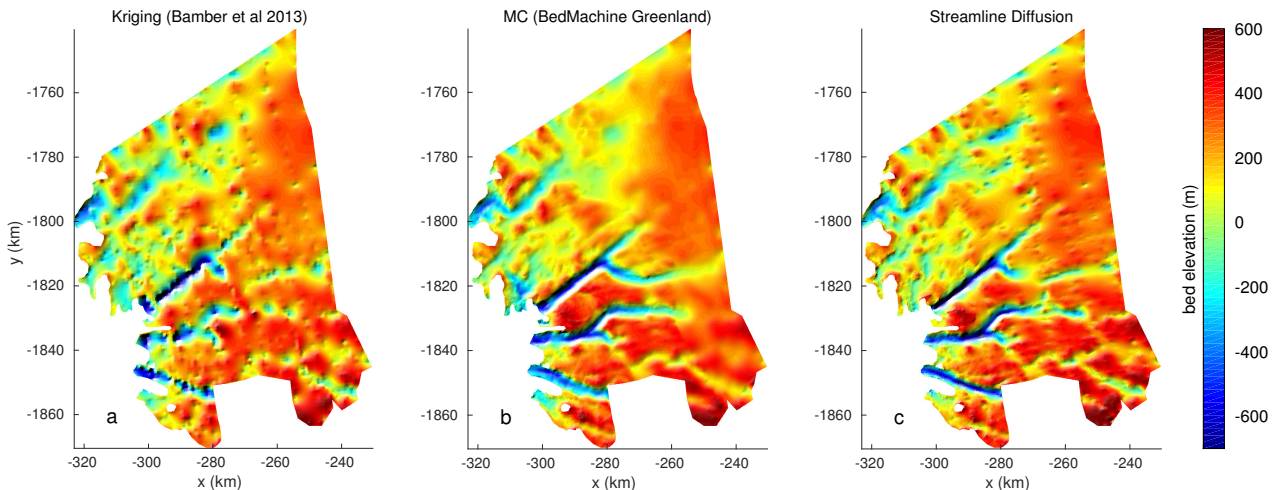


Figure S4: Example of bed mapping from (a) Kriging, (b) mass conservation and (c) streamline diffusion, applied to the Upernivik sector in western Greenland.

1.5 Ice-free land

On ice-free land, we rely directly on the REMA dem [Howat *et al.*, 2018, 2019].

1.6 Ocean bathymetry

Most of the ocean bathymetry is based on IBCSO [Arndt *et al.*, 2013]. Under Pine Island ice shelf we used the gravity inversion from Millan *et al.* [2017]. in the case of Thwaites, Dotson, Crosson and the Getz Ice shelves, we used an updated version of Millan *et al.* [2017] with the methodology from [An *et al.*, 2019], using constraints from both OIB radar sounder data and mass conservation onshore and multibeam observation offshore. We use the inversion from Greenbaum *et al.* [2015] under the Totten ice shelf, and seismic from Rosier *et al.* [2018] for the Southeastern Filchner-Ronne Ice Shelf.

1.7 Ice Shelf thickness

Following Griggs and Bamber [2009] and Le Brocq *et al.* [2010], we derive the ice thickness of floating ice shelves by relying on the hydrostatic equilibrium. The top surface is not covered with solid ice, however, and the presence of a firn layer has to be accounted for. The firn air content is defined as:

$$\delta = 1/\rho_i \int_{\text{firn layer}} (\rho_i - \rho_f) dz \quad (\text{S7})$$

where $\rho_i = 917 \text{ kg/m}^3$ is the ice density and ρ_f is the firn density that varies with depth. We define the ice shelf thickness in ice equivalent, H_i^* , such that:

$$\rho_i H_i^* = \int_b^s \rho dz = \rho_i H - \int_{\text{firn layer}} (\rho_i - \rho_f) dz = \rho_i (H - \delta) \quad (\text{S8})$$

The ice shelf thickness is therefore the sum of an ice equivalent ice thickness, H_i^* and firn depth correction:

$$H = H_i^* + \delta \quad (\text{S9})$$

Here, we use firn air content as simulated by the firn densification model from Ligtenberg *et al.* [2011], is forced at the surface by output of the regional climate model RACMO2.3p2 [van Wessem *et al.*, 2018].

Hydrostatic equilibrium imposes that:

$$\rho_i H_i^* = -\rho_w b \quad (\text{S10})$$

where $\rho_w = 1027 \text{ kg/m}^3$ is the density of sea water [Griggs and Bamber, 2009]. In terms of surface elevation, this equation becomes

$$\rho_i H_i^* = \rho_w (H_i^* + \delta - s) \quad (\text{S11})$$

and so the inferred ice equivalent thickness is:

$$H_i^* = (s - \delta) \frac{\rho_w}{\rho_w - \rho_i} \quad (\text{S12})$$

The actual ice thickness is therefore:

$$H = (s - \delta) \frac{\rho_w}{\rho_w - \rho_i} + \delta \quad (\text{S13})$$

By comparing the estimated ice thickness with radar derived thickness for all ice shelves, we found that this method provided reasonable results for some ice shelves such as Amery and Ross, but performed poorly in other sectors such as the Amundsen Sea Embayment. The source of discrepancies between the hydrostatic ice thickness and the measured ice thickness from radar is attributed to the firn depth correction δ . We decided to use the radar data to recalibrate the modeled firn depth correction in order to minimize this misfit. We forced a smooth transition between the grounded ice thickness and the floating ice thickness over the first 3 km downstream of the grounding lines. In most cases, the smoothing changed the ice thickness by less than 1000 m.

We force the bathymetry to be at least 1 m below the ice shelf base. While not satisfying, there are many regions where there is no bathymetry estimate and forcing IBCSO to be consistent with our grounding line by lowering the bathymetry was the simplest solution.

1.8 Mosaicking

The mosaicking process is done in three steps.

First, we stitch together all individual MC ice thickness maps. Two adjacent MC maps of ice thickness are constrained by the same flight lines along their boundaries. The ice thicknesses at the boundary of two adjacent maps are therefore very close to each other. We create a gap of $\sim 2 \text{ km}$ between the two maps and use a simple interpolation (Inverse Distance Weighting, with an exponent of 2) in order to create a smooth transition.

Then, we combine mass conservation along the coast, and streamline diffusion in the interior in order to provide a complete map of the bed topography under the Antarctic ice sheet. Streamline diffusion is applied 5 km away from the MC maps and we add the MC ice thickness results as additional constraints to the algorithm. The streamline diffusion algorithm used here is part of the Ice Sheet System Model (ISSM).

Finally, we fill the remaining gaps with a minimum curvature algorithm. Figure S5a shows what method is used to derive the ice thickness for the entire ice sheet.

2 Error Analysis

2.1 Fast flowing sectors

We rely on the same method as the one described in *Morlighem et al.* [2014a]. We want to evaluate the error δH made on the ice thickness given errors in both velocity $\delta \bar{v}$ and apparent mass balance $\delta \dot{a}$. The calculated thickness $H + \delta H$ is solution of the mass balance equation by definition:

$$\nabla \cdot (H + \delta H) (\bar{v} + \delta \bar{v}) = \dot{a} + \delta \dot{a}. \quad (\text{S14})$$

If we neglect second order terms and assume that the real thickness H is solution of the mass balance equation, the thickness error is solution of:

$$\nabla \cdot \delta H \bar{v} = \delta \dot{a} - \nabla \cdot H \delta \bar{v}. \quad (\text{S15})$$

The error is known on the flight tracks T and δH is solution of:

$$\begin{cases} \nabla \cdot (\delta H \bar{v}) = \delta \dot{a} + \nabla \cdot H \delta \bar{v} & \text{in } \Omega \\ \delta H = H - H_{obs} & \text{on } \Gamma_- \cup T \end{cases}. \quad (\text{S16})$$

This expression does not take into account the fact that the flux is well constrained upstream of each flight track. The simplest way to take that into account is to solve two problems:

$$\begin{cases} \nabla \cdot \delta H_1 (+\bar{v}) = \delta \dot{a} + \nabla \cdot H \delta \bar{v} & \text{in } \Omega \\ \delta H = H - H_{obs} & \text{on } \Gamma_- \cup T \end{cases} \quad (\text{S17})$$

$$\begin{cases} \nabla \cdot \delta H_2 (-\bar{v}) = \delta \dot{a} + \nabla \cdot H \delta \bar{v} & \text{in } \Omega \\ \delta H = H - H_{obs} & \text{on } \Gamma_- \cup T \end{cases}, \quad (\text{S18})$$

so that the error propagates once downstream (δH_1) and once upstream (δH_2). The actual error would be the minimum of the two:

$$\delta H = \min(\delta H_1, \delta H_2). \quad (\text{S19})$$

To evaluate the right hand side, we take $\delta \dot{a} = 0.5$ m/a, the error in velocities is 2 m/a and the error in strain rate is estimated as 3×10^{-4} yr⁻¹ based on observation errors.

2.2 Slow moving sectors

In the slow moving sectors, where we rely on streamline diffusion, we assume that the error grows in between flight lines by 20 m per km (i.e. a 2% slope). The error is saturated at 1000 m to avoid unrealistically large estimates in locations where there are no data available. One important source of error that we are not accounting for here is the uncertainty in geolocation, especially for older datasets. Deviations can reach several 100 m to 1000 m.

2.3 Ice-free land

On ice-free land, we estimate an error of 10 m.

2.4 Ocean bathymetry

The error in ocean bathymetry is derived from the IBCSO's data source. We assume an error of 10 m where IBCSO is based on bathymetry measurements, and use the same approximation as for the slow moving region (20 m per km) in between measurements.

2.5 Cavities under ice shelves

We rely on the same error estimates as the one for the ocean bathymetry except in regions mapped using gravity for which we use the inversion derived error mapped, using a minimum error of 30 m.

3 Sea level potential

Note that the sea level potential of each basin is derived from the total ice volume above floatation of each sector following the delineations from the ice sheet mass balance inter-comparison exercise (IMBIE).

Basin name	Vol. (10^3 km^3)	Vol. above float. (10^3 km^3)	Sea level eq. (cm)
Abbot	23.0 ± 0.8	16.5 ± 0.8	4.2 ± 0.2
Pine Island	366 ± 5	202 ± 5	51 ± 1
Lucchitta Velasco	4.7 ± 0.2	3.4 ± 0.2	0.85 ± 0.04
Cosgrove	6.1 ± 0.2	4.2 ± 0.2	1.05 ± 0.06
Walgreen Coast	$710 \pm 700 \times 10^{-3}$	$520 \pm 700 \times 10^{-3}$	0.13 ± 0.02
King	$460 \pm 400 \times 10^{-3}$	$440 \pm 400 \times 10^{-3}$	0.11 ± 0.01
Thwaites	483 ± 6	258 ± 6	65 ± 1
Haynes	14.6 ± 0.3	7.9 ± 0.3	2.01 ± 0.07
Pope	10.5 ± 0.2	5.7 ± 0.2	1.45 ± 0.05
Smith	8.5 ± 0.2	4.6 ± 0.2	1.17 ± 0.04
Philbin	1.02 ± 0.08	$750 \pm 800 \times 10^{-3}$	0.19 ± 0.02
Kohler	19.4 ± 0.4	12.6 ± 0.4	3.2 ± 0.1
Getz	105 ± 3	85 ± 3	21.6 ± 0.6
Jackson-Perkins	$630 \pm 500 \times 10^{-3}$	$480 \pm 500 \times 10^{-3}$	0.12 ± 0.01
Hull	20.7 ± 0.5	17.7 ± 0.5	4.5 ± 0.1
Bindschadler	244 ± 4	130 ± 4	32.8 ± 0.9
Frostman-Lord-Shuman-Anandakri	4.7 ± 0.2	3.5 ± 0.2	0.88 ± 0.05
Kamb	296 ± 5	161 ± 5	41 ± 1
Land	14.1 ± 0.4	13.2 ± 0.4	3.34 ± 0.10
MacAyeal	311 ± 6	213 ± 6	54 ± 1
Nickerson	5.5 ± 0.3	4.3 ± 0.3	1.08 ± 0.08
Mercer	76 ± 2	56 ± 2	14.2 ± 0.5
Sulzberger	32 ± 1	26 ± 1	6.5 ± 0.3
Leverett	1.3 ± 0.1	$900 \pm 10000 \times 10^{-3}$	0.23 ± 0.03
Whillans	296 ± 6	191 ± 6	48 ± 2
Ruppert Coast2	$220 \pm 200 \times 10^{-3}$	$140 \pm 200 \times 10^{-3}$	0.035 ± 0.004
Echelmeyer	18.3 ± 0.6	9.5 ± 0.6	2.4 ± 0.1
Scott	36 ± 1	36 ± 1	9.0 ± 0.3
Butler-Swinburne	1.7 ± 0.1	1.3 ± 0.1	0.33 ± 0.03
Prestud	7.8 ± 0.4	4.6 ± 0.4	1.17 ± 0.09
Richter	$170 \pm 200 \times 10^{-3}$	$160 \pm 200 \times 10^{-3}$	0.040 ± 0.005
Saunders Coast	$6 \pm 5 \times 10^{-3}$	$6 \pm 5 \times 10^{-3}$	0.001 ± 0.001
Withrow	$870 \pm 700 \times 10^{-3}$	$840 \pm 700 \times 10^{-3}$	0.21 ± 0.02
Hamilton	$500 \pm 400 \times 10^{-3}$	$410 \pm 400 \times 10^{-3}$	0.10 ± 0.01
Shirases Coast2	$30 \pm 100 \times 10^{-3}$	$30 \pm 100 \times 10^{-3}$	0.006 ± 0.003
Shirases Coast1	$60 \pm 100 \times 10^{-3}$	$60 \pm 100 \times 10^{-3}$	0.015 ± 0.003
Amundsen	35.5 ± 0.9	35.2 ± 0.9	8.9 ± 0.2
Bowman Strom Live Axel-Heigerg	3.1 ± 0.3	2.4 ± 0.3	0.61 ± 0.08
Ross East1	$220 \pm 700 \times 10^{-3}$	$70 \pm 700 \times 10^{-3}$	0.02 ± 0.02
Shackleton	4.9 ± 0.4	4.9 ± 0.4	1.24 ± 0.10
Ross East2	$500 \pm 30000 \times 10^{-3}$	$200 \pm 30000 \times 10^{-3}$	0.06 ± 0.07
Victoria Land3	$10 \pm 100 \times 10^{-3}$	$0 \pm 100 \times 10^{-3}$	0.001 ± 0.003
Tucker	$200 \pm 30000 \times 10^{-3}$	$100 \pm 30000 \times 10^{-3}$	0.03 ± 0.08
Victoria Land2	$300 \pm 40000 \times 10^{-3}$	$300 \pm 40000 \times 10^{-3}$	0.1 ± 0.1

Beardmore	221 ± 4	217 ± 4	55.0 ± 0.9
Mariner	600 ± 30000 × 10 ⁻³	500 ± 30000 × 10 ⁻³	0.12 ± 0.06
Icebreaker-Fitzgerald	50 ± 400 × 10 ⁻³	30 ± 400 × 10 ⁻³	0.01 ± 0.01
Ross East3	600 ± 20000 × 10 ⁻³	300 ± 20000 × 10 ⁻³	0.08 ± 0.05
Aviator	1.6 ± 0.2	1.4 ± 0.2	0.36 ± 0.05
Campbell-Tinker	1.5 ± 0.2	1.2 ± 0.2	0.30 ± 0.04
Lillie	1.2 ± 0.4	1.0 ± 0.4	0.3 ± 0.1
Lennox-King	22.5 ± 0.6	22.3 ± 0.6	5.7 ± 0.2
Skelton	5.5 ± 0.4	5.0 ± 0.4	1.27 ± 0.09
Victoria Land1	40 ± 600 × 10 ⁻³	30 ± 600 × 10 ⁻³	0.01 ± 0.01
Prietsley-Rieves	29.3 ± 0.6	27.1 ± 0.6	6.9 ± 0.2
Dry Valleys	23.3 ± 1.0	23.1 ± 1.0	5.9 ± 0.3
Rennick	39 ± 2	37 ± 2	9.5 ± 0.4
Ross East4	900 ± 30000 × 10 ⁻³	600 ± 30000 × 10 ⁻³	0.14 ± 0.07
Oates Coast2	2.4 ± 0.3	2.3 ± 0.3	0.58 ± 0.07
Ross East5	4.2 ± 0.3	4.0 ± 0.3	1.03 ± 0.07
Matusevitch	26.1 ± 0.5	23.4 ± 0.5	5.9 ± 0.1
Oates Coast1	90 ± 7 × 10 ⁻³	54 ± 7 × 10 ⁻³	0.014 ± 0.002
Lauritzen	4.7 ± 0.1	4.0 ± 0.1	1.00 ± 0.03
David	549 ± 6	474 ± 6	120 ± 2
Slava	4.2 ± 0.2	3.2 ± 0.2	0.80 ± 0.04
Cook	852 ± 9	630 ± 9	160 ± 2
Mulock	347 ± 4	313 ± 4	79 ± 1
Wilkes Land2	3.2 ± 0.1	2.2 ± 0.1	0.55 ± 0.03
Nimrod	753 ± 8	733 ± 8	186 ± 2
Wilkes Land1	2.1 ± 0.1	1.7 ± 0.1	0.43 ± 0.03
Ninnis	459 ± 5	381 ± 5	97 ± 1
Byrd	2.63 ± 0.03 × 10 ³	2.52 ± 0.03 × 10 ³	640 ± 7
Mertz	169 ± 3	147 ± 3	37.4 ± 0.6
Adelie Coast	169 ± 3	146 ± 3	36.9 ± 0.6
Dibble	55.8 ± 1.0	50.8 ± 1.0	12.9 ± 0.2
Clarie Coast	32.8 ± 0.8	28.0 ± 0.8	7.1 ± 0.2
Frost	372 ± 4	339 ± 4	86 ± 1
Holmes	50.8 ± 0.9	45.5 ± 0.9	11.5 ± 0.2
Sabrina Coast1	470 ± 300 × 10 ⁻³	450 ± 300 × 10 ⁻³	0.113 ± 0.008
Voyeykov	7.9 ± 0.2	7.2 ± 0.2	1.83 ± 0.05
Sabrina Coast2	4.0 ± 0.1	3.7 ± 0.1	0.93 ± 0.03
Moscow	608 ± 7	511 ± 7	130 ± 2
Totten	1.81 ± 0.02 × 10 ³	1.54 ± 0.02 × 10 ³	389 ± 4
Law Dome	9.6 ± 0.4	8.7 ± 0.4	2.2 ± 0.1
Vincennes Bay	325 ± 4	264 ± 4	67 ± 1
Budd Coast	20.1 ± 0.5	19.2 ± 0.5	4.9 ± 0.1
Conger Glenzer	5.9 ± 0.2	5.8 ± 0.2	1.48 ± 0.04
Knox Coast	200 ± 100 × 10 ⁻³	170 ± 100 × 10 ⁻³	0.044 ± 0.003
Tracy Tremenchus	4.7 ± 0.2	4.6 ± 0.2	1.16 ± 0.04
Denman Scott	640 ± 8	590 ± 8	149 ± 2
Wilhelm II Coast	156 ± 3	153 ± 3	38.8 ± 0.7
Leopold and Astrid Coast	482 ± 6	457 ± 6	116 ± 2
Ingrid Christensen Coast	163 ± 3	161 ± 3	40.7 ± 0.7
Publications	53 ± 1	52 ± 1	13.3 ± 0.3

American HighLand	395 ± 6	388 ± 6	98 ± 2
Lambert	$1.10 \pm 0.01 \times 10^3$	$1.06 \pm 0.01 \times 10^3$	269 ± 3
MacRobertson Land	222 ± 5	213 ± 5	54 ± 1
Mawson Coast	137 ± 3	132 ± 3	33.3 ± 0.8
Mellor	$1.22 \pm 0.01 \times 10^3$	$1.19 \pm 0.01 \times 10^3$	303 ± 3
Fisher	228 ± 3	224 ± 3	56.8 ± 0.8
Enderby Land2	$1 \pm 2000 \times 10^{-3}$	$1 \pm 2000 \times 10^{-3}$	0.0002 ± 0.0004
Edward VIII	1.7 ± 0.1	1.5 ± 0.1	0.39 ± 0.03
WilmaRobertDowner	74 ± 2	74 ± 2	18.7 ± 0.4
Enderby Land	28 ± 1	26 ± 1	6.7 ± 0.4
Rayner Thyer	217 ± 4	215 ± 4	54.5 ± 0.9
Prince Olav Coast	109 ± 3	108 ± 3	27.3 ± 0.6
Shirase Glacier	476 ± 6	475 ± 6	120 ± 2
Prince Harald Coast2	$1 \pm 2 \times 10^{-3}$	$1 \pm 2 \times 10^{-3}$	0.0003 ± 0.0004
Prince Harald	16.1 ± 0.6	13.6 ± 0.6	3.4 ± 0.1
Prince Harald Coast1	$490 \pm 400 \times 10^{-3}$	$380 \pm 400 \times 10^{-3}$	0.10 ± 0.01
Baudouin	552 ± 9	538 ± 9	136 ± 2
Borchgrevink	297 ± 5	285 ± 5	72 ± 1
Lazarev	30.8 ± 1.0	25.5 ± 1.0	6.5 ± 0.2
Princess Astrid Coast2	$13 \pm 2 \times 10^{-3}$	$5 \pm 2 \times 10^{-3}$	0.0013 ± 0.0006
Nivl	33.9 ± 0.8	31.3 ± 0.8	7.9 ± 0.2
Vigrid	62 ± 1	60 ± 1	15.1 ± 0.3
Princess Astrid Coast1	$15 \pm 2 \times 10^{-3}$	$8 \pm 2 \times 10^{-3}$	0.0021 ± 0.0006
Jutulstraumen	303 ± 6	290 ± 6	74 ± 1
Jelbart	16.6 ± 0.6	13.4 ± 0.6	3.4 ± 0.2
Atka	$810 \pm 400 \times 10^{-3}$	$420 \pm 400 \times 10^{-3}$	0.11 ± 0.01
Ekstrom	11.7 ± 0.5	8.5 ± 0.5	2.1 ± 0.1
Princess Martha Coast2	$10 \pm 1 \times 10^{-3}$	$4 \pm 1 \times 10^{-3}$	0.0011 ± 0.0004
Quar	1.80 ± 0.08	$880 \pm 800 \times 10^{-3}$	0.22 ± 0.02
Princess Martha Coast1	$190 \pm 200 \times 10^{-3}$	$120 \pm 200 \times 10^{-3}$	0.031 ± 0.004
Riiser-Larsen	93 ± 3	76 ± 3	19.3 ± 0.7
Slessor	$1.27 \pm 0.01 \times 10^3$	$1.15 \pm 0.01 \times 10^3$	292 ± 4
Recovery	$2.58 \pm 0.03 \times 10^3$	$2.43 \pm 0.03 \times 10^3$	615 ± 8
Brunt Stancomb	205 ± 4	185 ± 4	46.9 ± 0.9
Bailey	114 ± 2	83 ± 2	20.9 ± 0.6
Coats Coast	21.5 ± 0.8	20.4 ± 0.8	5.2 ± 0.2
Support Force	288 ± 5	265 ± 5	67 ± 1
Academy	$1.09 \pm 0.01 \times 10^3$	980 ± 100	249 ± 3
Eastern Graham Land	$100 \pm 10000 \times 10^{-3}$	$100 \pm 10000 \times 10^{-3}$	0.03 ± 0.03
LarsenE Kemp Peninsula	$26 \pm 8 \times 10^{-3}$	$25 \pm 8 \times 10^{-3}$	0.006 ± 0.002
LarsenA	$110 \pm 300 \times 10^{-3}$	$110 \pm 300 \times 10^{-3}$	0.027 ± 0.009
Drygalskis Headland	$2 \pm 4 \times 10^{-3}$	$1 \pm 4 \times 10^{-3}$	0.0003 ± 0.0010
LarsenF Piggot Peninsula	$26 \pm 6 \times 10^{-3}$	$25 \pm 6 \times 10^{-3}$	0.006 ± 0.001
Drygalski	$120 \pm 300 \times 10^{-3}$	$110 \pm 300 \times 10^{-3}$	0.029 ± 0.007
LarsenG Smith Peninsula	$28 \pm 7 \times 10^{-3}$	$24 \pm 7 \times 10^{-3}$	0.006 ± 0.002
Hektoria Headland	$10 \pm 100 \times 10^{-3}$	$10 \pm 100 \times 10^{-3}$	0.003 ± 0.003
Jason Peninsula	$200 \pm 300 \times 10^{-3}$	$110 \pm 300 \times 10^{-3}$	0.028 ± 0.006
LarsenE	3.1 ± 0.3	2.9 ± 0.3	0.74 ± 0.08
Evans Headland	$4 \pm 3 \times 10^{-3}$	$4 \pm 3 \times 10^{-3}$	0.0011 ± 0.0008
LarsenF	1.1 ± 0.1	1.0 ± 0.1	0.26 ± 0.04

Hektoria Green Evans	$100 \pm 400 \times 10^{-3}$	$80 \pm 400 \times 10^{-3}$	0.021 ± 0.010
Pequod	$14 \pm 9 \times 10^{-3}$	$10 \pm 9 \times 10^{-3}$	0.002 ± 0.002
Punchbowl	$1 \pm 2000 \times 10^{-3}$	$1 \pm 2000 \times 10^{-3}$	0.0002 ± 0.0006
LarsenG Bowman Peninsula	$15 \pm 2 \times 10^{-3}$	$14 \pm 2 \times 10^{-3}$	0.0036 ± 0.0004
Stubb	$6 \pm 5 \times 10^{-3}$	$5 \pm 5 \times 10^{-3}$	0.001 ± 0.001
LarsenD	10 ± 1	10 ± 1	2.5 ± 0.3
Jorum	$50 \pm 100 \times 10^{-3}$	$50 \pm 100 \times 10^{-3}$	0.012 ± 0.003
Mapple	$3 \pm 4 \times 10^{-3}$	$2 \pm 4 \times 10^{-3}$	0.0006 ± 0.0010
Starbuck	$9 \pm 7 \times 10^{-3}$	$8 \pm 7 \times 10^{-3}$	0.002 ± 0.002
Melville	$19 \pm 6 \times 10^{-3}$	$19 \pm 6 \times 10^{-3}$	0.005 ± 0.002
LarsenG	$680 \pm 1000 \times 10^{-3}$	$640 \pm 1000 \times 10^{-3}$	0.16 ± 0.02
Crane	$230 \pm 300 \times 10^{-3}$	$210 \pm 300 \times 10^{-3}$	0.052 ± 0.008
Flask	$220 \pm 300 \times 10^{-3}$	$190 \pm 300 \times 10^{-3}$	0.048 ± 0.008
Leppard	$550 \pm 500 \times 10^{-3}$	$460 \pm 500 \times 10^{-3}$	0.12 ± 0.01
West Graham Land	2.4 ± 0.7	2.3 ± 0.7	0.6 ± 0.2
LarsenC	4.3 ± 0.5	3.4 ± 0.5	0.9 ± 0.1
D Orville Coast	10.5 ± 0.8	8.7 ± 0.8	2.2 ± 0.2
Fleming	4.0 ± 0.2	3.7 ± 0.2	0.93 ± 0.04
Airy Rott Seller	$590 \pm 500 \times 10^{-3}$	$550 \pm 500 \times 10^{-3}$	0.14 ± 0.01
Harriott Headland	$10 \pm 8 \times 10^{-3}$	$9 \pm 8 \times 10^{-3}$	0.002 ± 0.002
Harriott	$210 \pm 400 \times 10^{-3}$	$210 \pm 400 \times 10^{-3}$	0.052 ± 0.010
Prospect	$960 \pm 400 \times 10^{-3}$	$850 \pm 400 \times 10^{-3}$	0.22 ± 0.01
Zonda Eureka	2.1 ± 0.1	1.8 ± 0.1	0.46 ± 0.03
Cape Jeremy	$100 \pm 100 \times 10^{-3}$	$70 \pm 100 \times 10^{-3}$	0.018 ± 0.004
Foundation	261 ± 5	223 ± 5	57 ± 1
George VI	72 ± 2	60 ± 2	15.2 ± 0.6
Wilkins George VI	1.8 ± 0.2	1.3 ± 0.2	0.33 ± 0.06
Moller	103 ± 2	56 ± 2	14.2 ± 0.5
Wilkins Island4	1.1 ± 0.2	1 ± 20	0.25 ± 0.06
Wilkins	3.7 ± 0.4	2.8 ± 0.4	0.7 ± 0.1
Bach	4.9 ± 0.3	3.6 ± 0.3	0.91 ± 0.08
Mendelssohn	1.24 ± 0.07	$840 \pm 700 \times 10^{-3}$	0.21 ± 0.02
Wilkins Island3	$200 \pm 200 \times 10^{-3}$	$180 \pm 200 \times 10^{-3}$	0.046 ± 0.005
Wilkins Island5	$6 \pm 1 \times 10^{-3}$	$5 \pm 1 \times 10^{-3}$	0.0012 ± 0.0003
Wilkins Island6	$18 \pm 2 \times 10^{-3}$	$16 \pm 2 \times 10^{-3}$	0.0040 ± 0.0006
Brahms	$320 \pm 300 \times 10^{-3}$	$270 \pm 300 \times 10^{-3}$	0.068 ± 0.007
Wilkins Island1	$29 \pm 6 \times 10^{-3}$	$29 \pm 6 \times 10^{-3}$	0.007 ± 0.001
Verdi	$270 \pm 200 \times 10^{-3}$	$210 \pm 200 \times 10^{-3}$	0.054 ± 0.005
Wilkins Island2	$480 \pm 500 \times 10^{-3}$	$400 \pm 500 \times 10^{-3}$	0.10 ± 0.01
Evans	170 ± 4	79 ± 4	20.0 ± 0.9
Stange	12.9 ± 0.4	8.5 ± 0.4	2.2 ± 0.1
Institute	291 ± 5	199 ± 5	50 ± 1
Hercules	7.3 ± 0.3	3.9 ± 0.3	0.98 ± 0.07
Carlson	23.4 ± 0.7	10.7 ± 0.7	2.7 ± 0.2
Rydberg Peninsula	$350 \pm 300 \times 10^{-3}$	$330 \pm 300 \times 10^{-3}$	0.084 ± 0.009
Thomson	$540 \pm 400 \times 10^{-3}$	$500 \pm 400 \times 10^{-3}$	0.13 ± 0.01
Union	4.3 ± 0.2	2.6 ± 0.2	0.65 ± 0.06
Alison	9.3 ± 0.3	6.5 ± 0.3	1.64 ± 0.07
Ferrigno	14.1 ± 0.3	8.3 ± 0.3	2.10 ± 0.07
Minnesota	4.9 ± 0.3	3.5 ± 0.3	0.88 ± 0.08

Rutherford	96 ± 2	49 ± 2	12.4 ± 0.4
Fox	3.8 ± 0.1	2.3 ± 0.1	0.59 ± 0.03
Venable	19.1 ± 0.4	11.9 ± 0.4	3.0 ± 0.1
Cooke	$120 \pm 100 \times 10^{-3}$	$100 \pm 100 \times 10^{-3}$	0.026 ± 0.003

Table S2: Basin names (from *Rignot et al.* [2019]), volume ($\times 10^3$ km 3), volume above floatation ($\times 10^3$ km 3) and sea level equivalent of all sectors of Antarctica

Basin name	Vol. (10³ km³)	Vol. above float. (10³ km³)	Sea level eq. (m)
Antarctic Peninsula	131 ± 8	108 ± 8	0.27 ± 0.02
West Antarctica	$(3.39 \pm 0.06) \times 10^3$	$(2.10 \pm 0.06) \times 10^3$	5.30 ± 0.2
East Antarctica	$(22.4 \pm 0.3) \times 10^3$	$(20.6 \pm 0.3) \times 10^3$	52.20 ± 0.7
Antarctica (incl. islands)	$(26.0 \pm 0.4) \times 10^3$	$(22.8 \pm 0.4) \times 10^3$	57.9 ± 0.9

Table S3: Volume ($\times 10^3$ km 3), volume above floatation ($\times 10^3$ km 3) and sea level equivalent of Antarctica

4 BedMachine Antarctica v1 dataset

BedMachine Antarctica v1 is provided in a NetCDF file, which uses a Polar Stereographic South projection (71°S , 0°E). The following fields on the same 500-m resolution grid: surface elevation (surface), ice thickness (thickness), bed (bed), error in bed elevation (errbed), mask (mask), firn (firn), geoid (geoid).

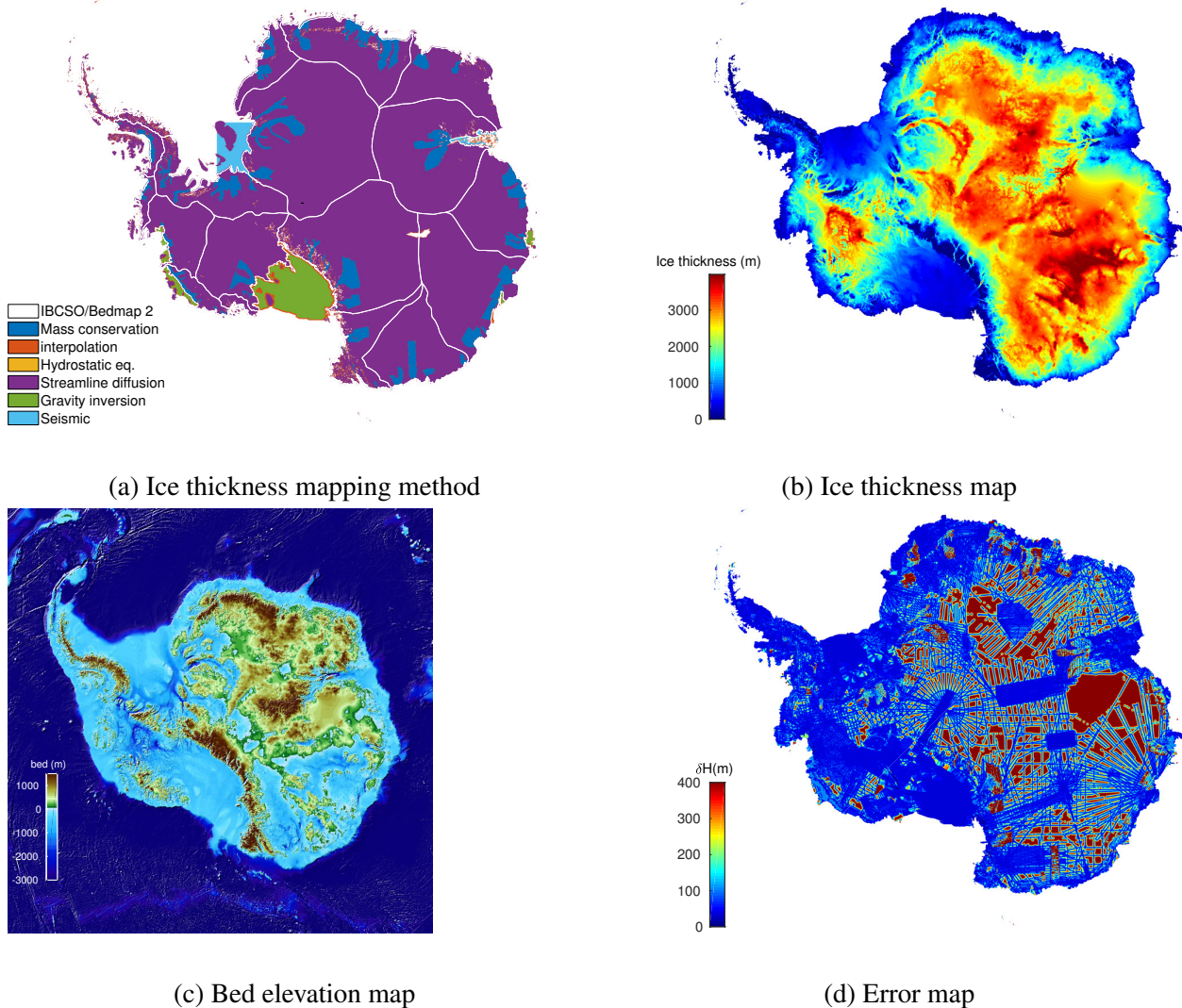


Figure S5: Example of fields included in BedMachine Antarctica

5 Comparison with existing datasets

5.1 Comparison with Bedmap2

In Fig. S6-S58, we show the following fields for a set of 53 glaciers: (a) bed topography from *Fretwell et al.* [2013], (b) bed topography from BedMachine Antarctica, (c) InSAR derived surface velocities, (d) Mass conservation error estimate and available radar data to constrain the model, (e) Difference between the bed from BedMachine and Bedmap2 (red: BedMachine is higher than Bedmap2). The dashed white line indicates the limit of the domain where mass conservation was applied. The grounding line (or ice edge) is shown as a

solid white line.

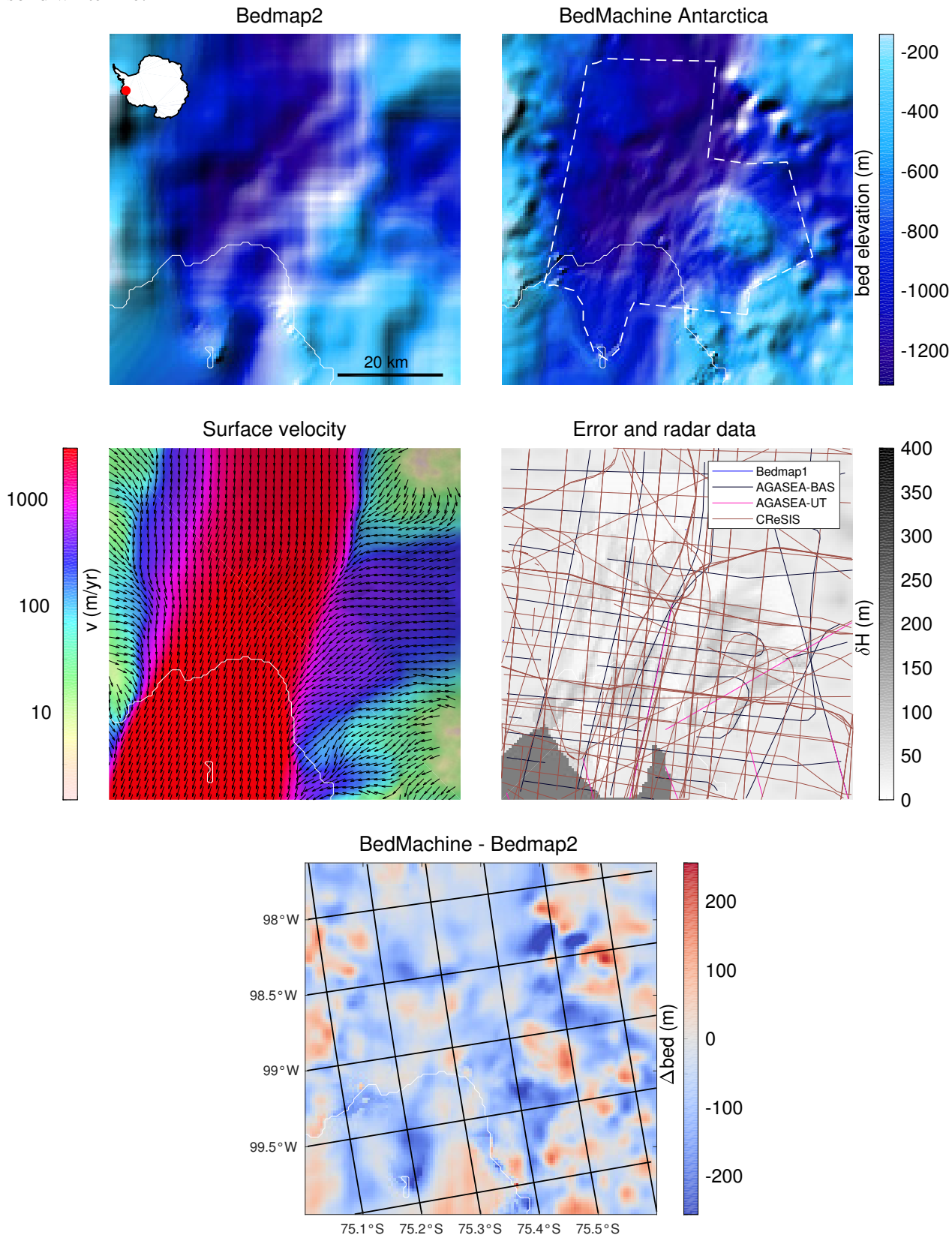


Figure S6: Pine Island Glacier

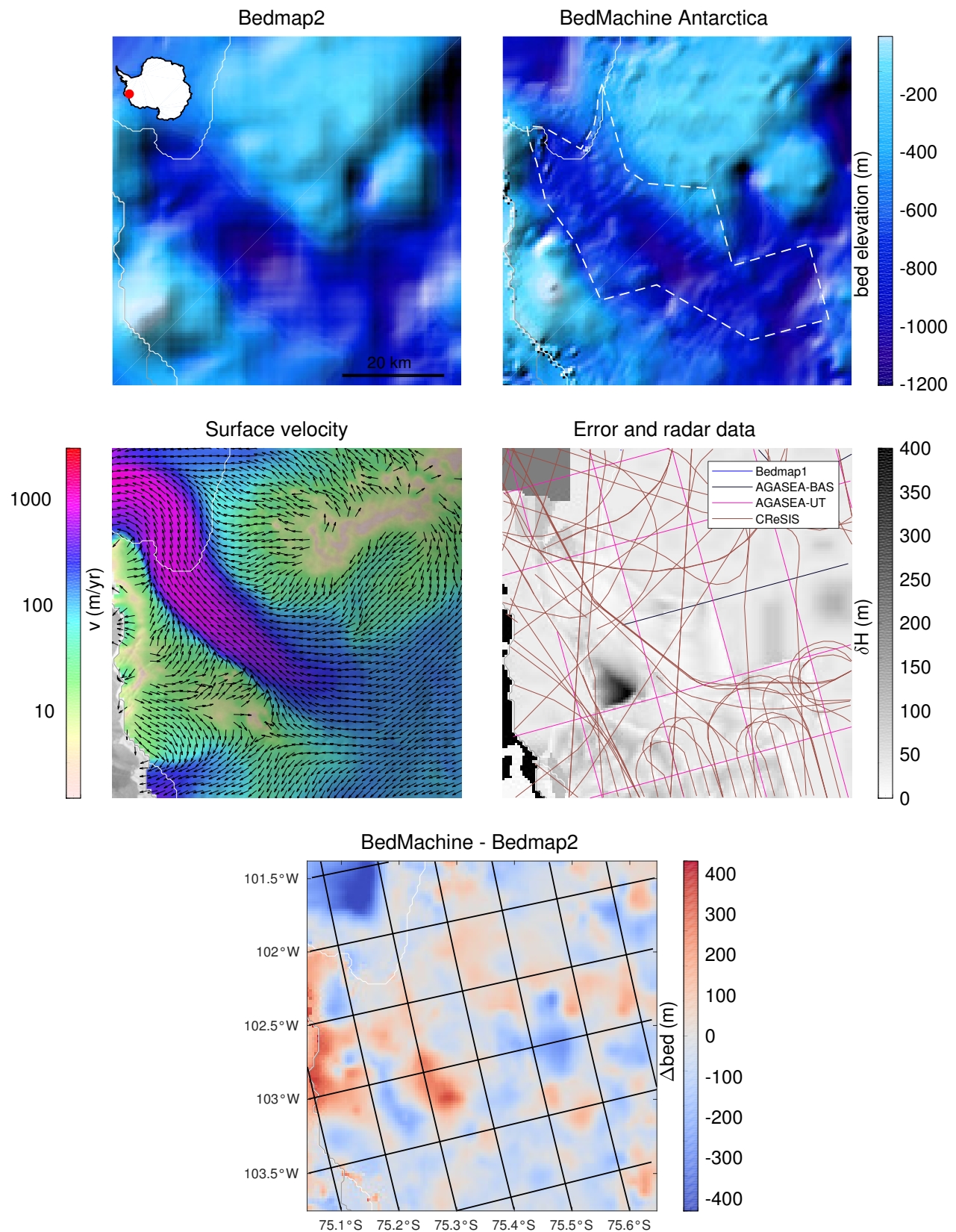


Figure S7: Pig-Thwaites junction

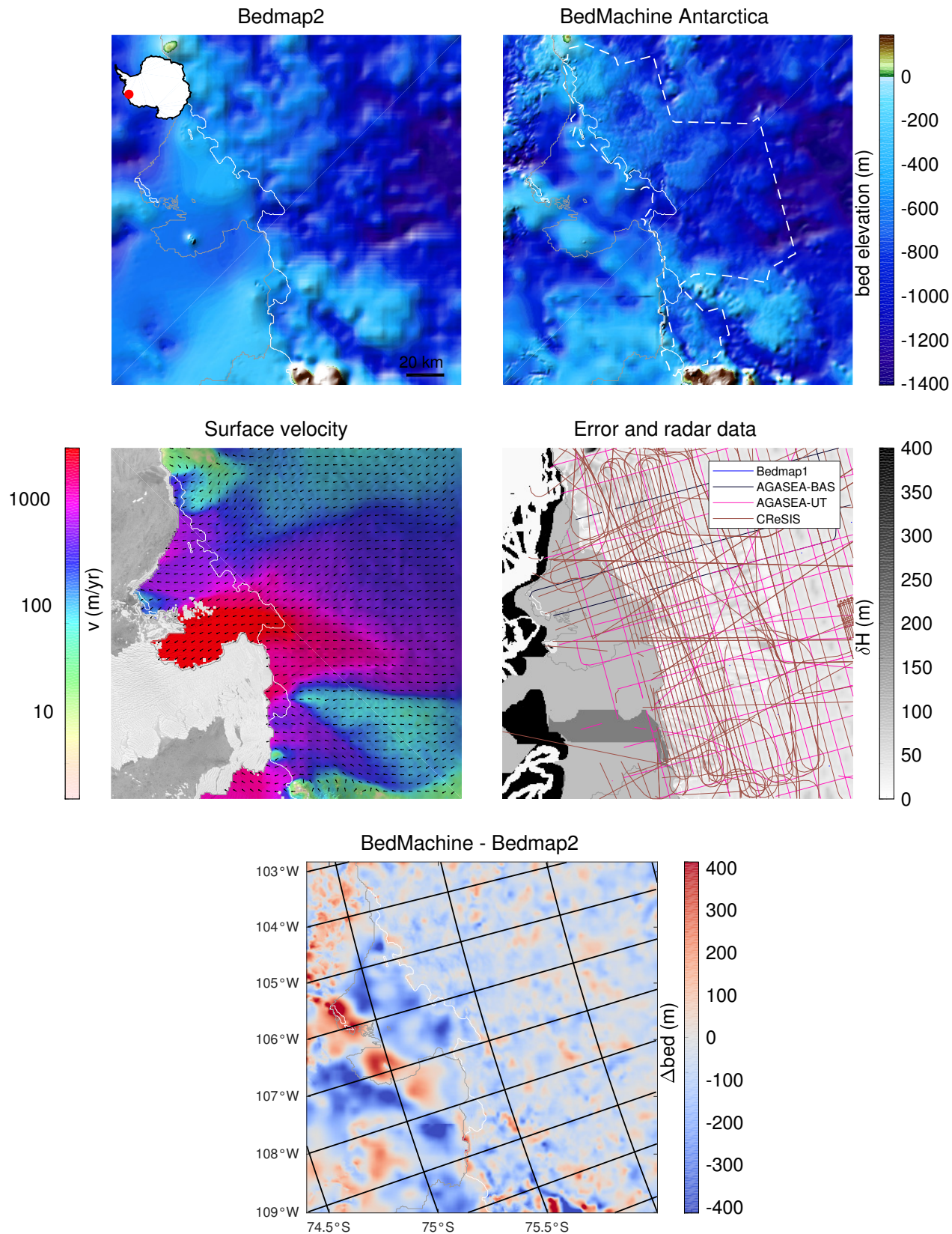
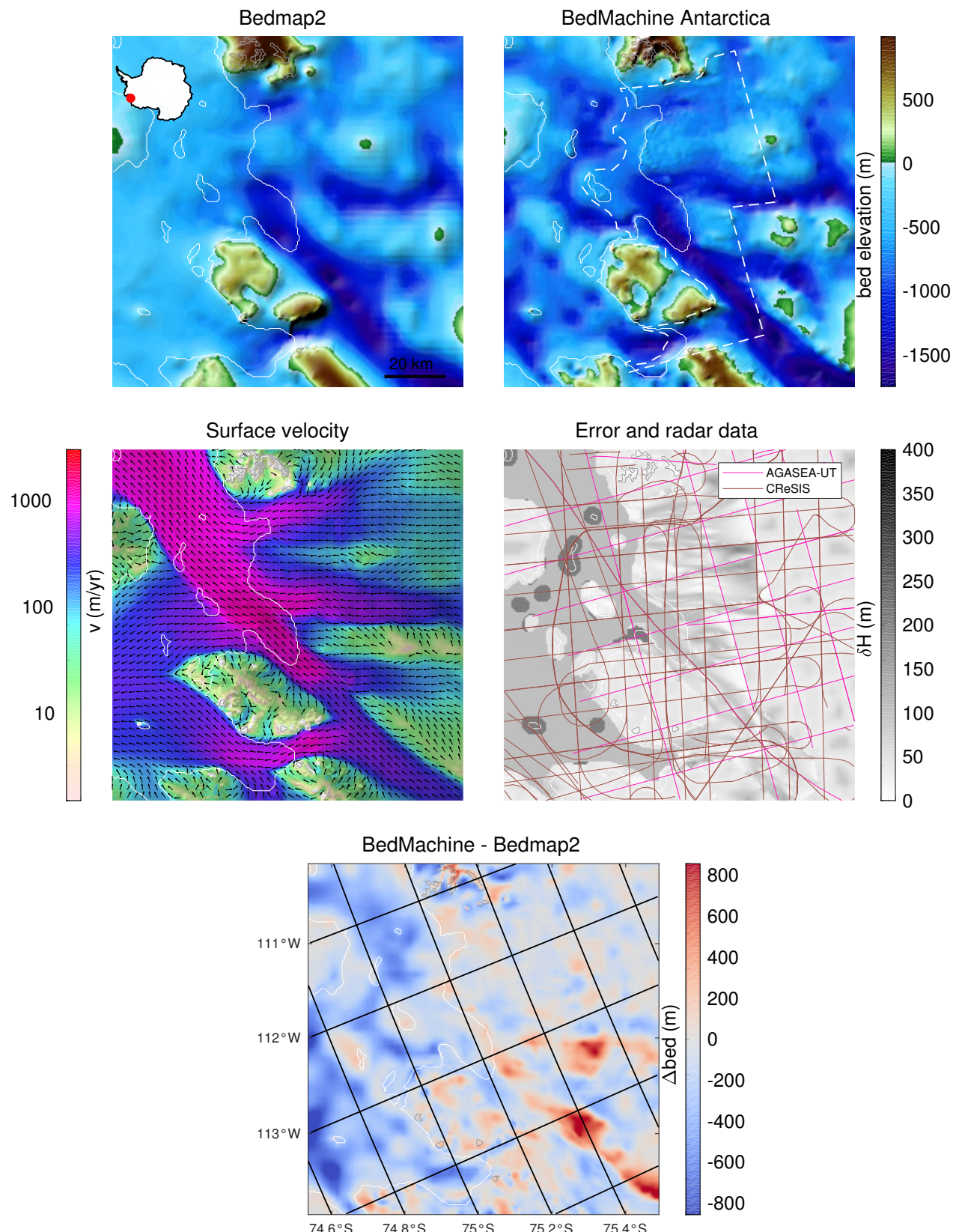


Figure S8: Thwaites



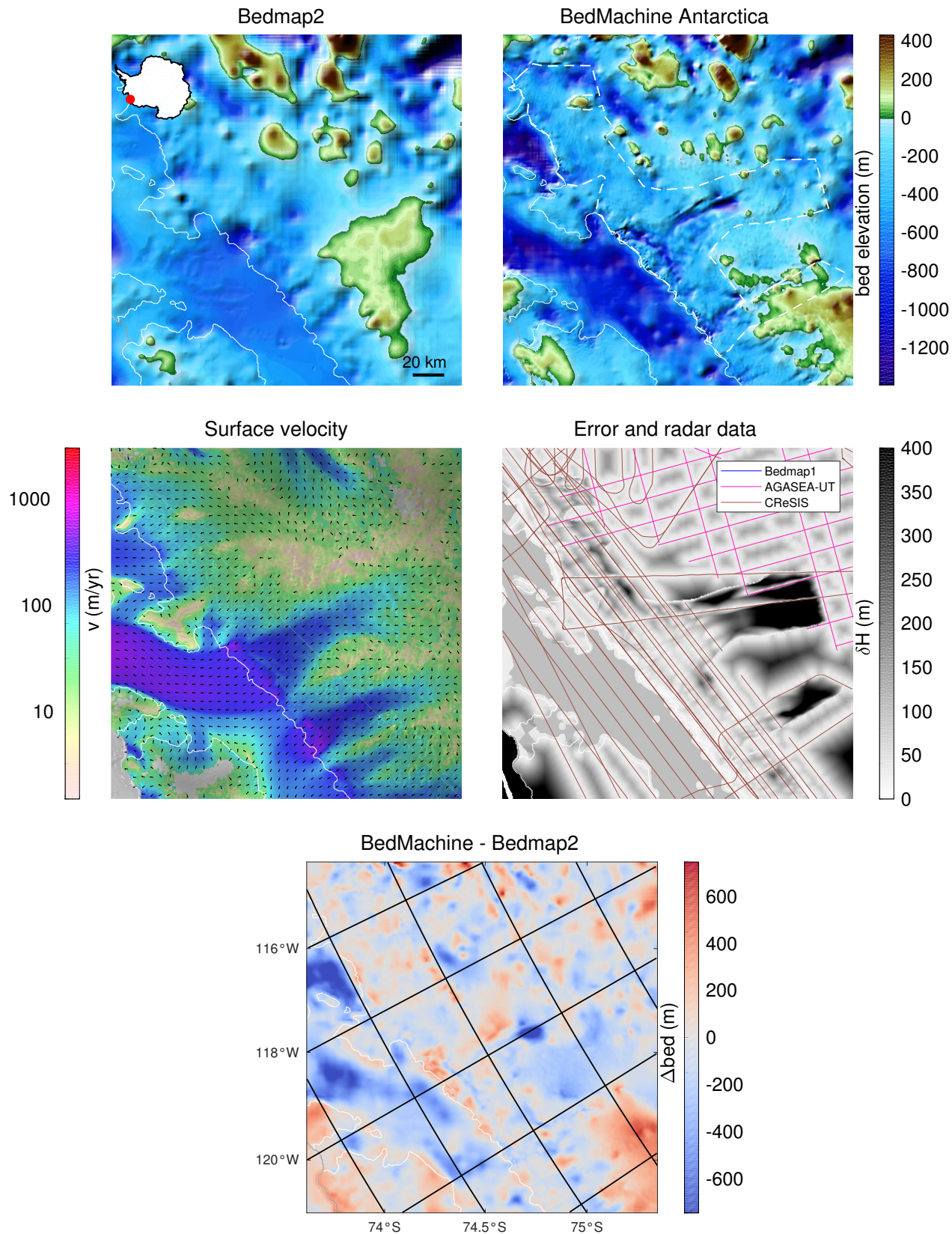


Figure S10: Beakley Glacier

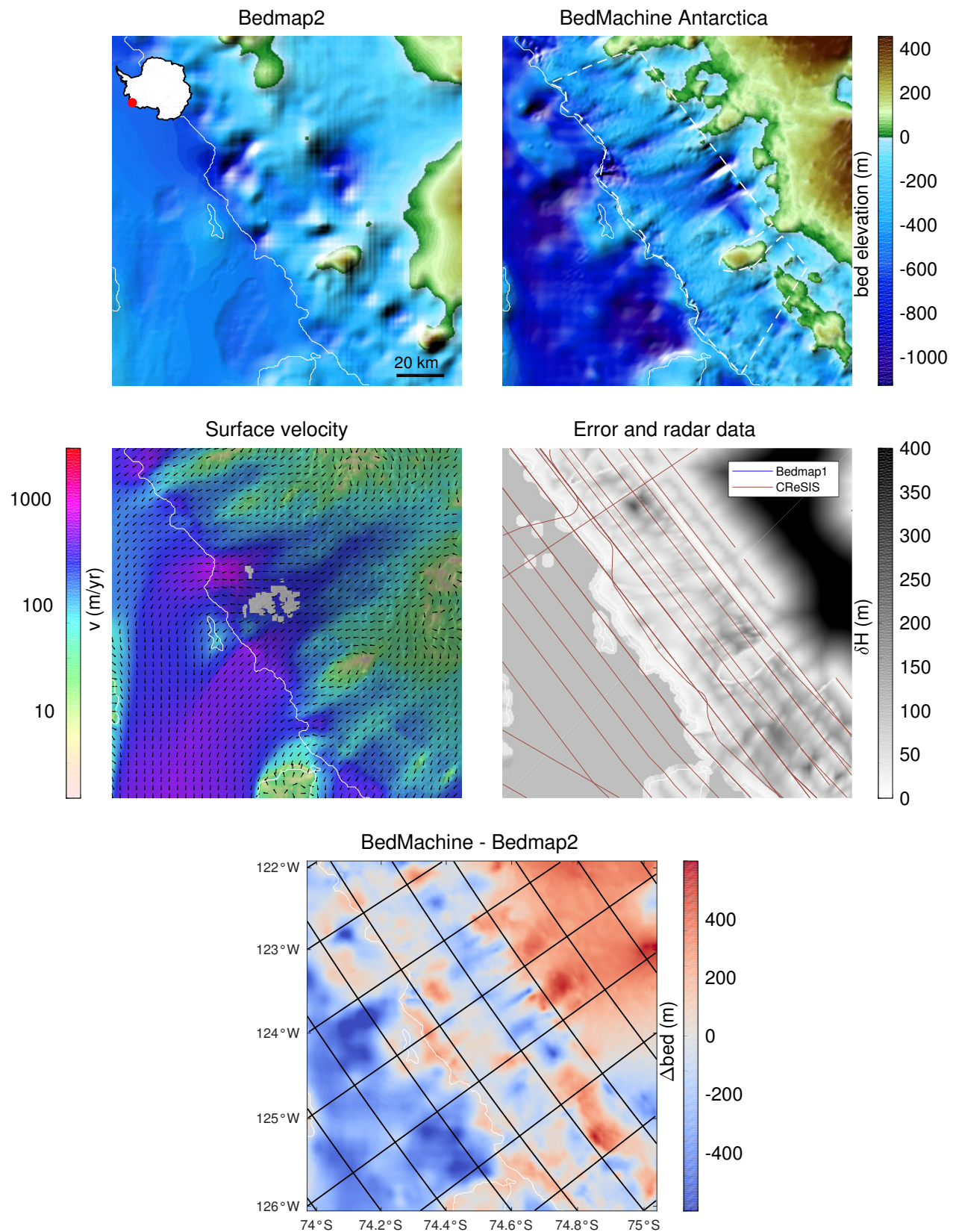


Figure S11: Getz Ic Shelf

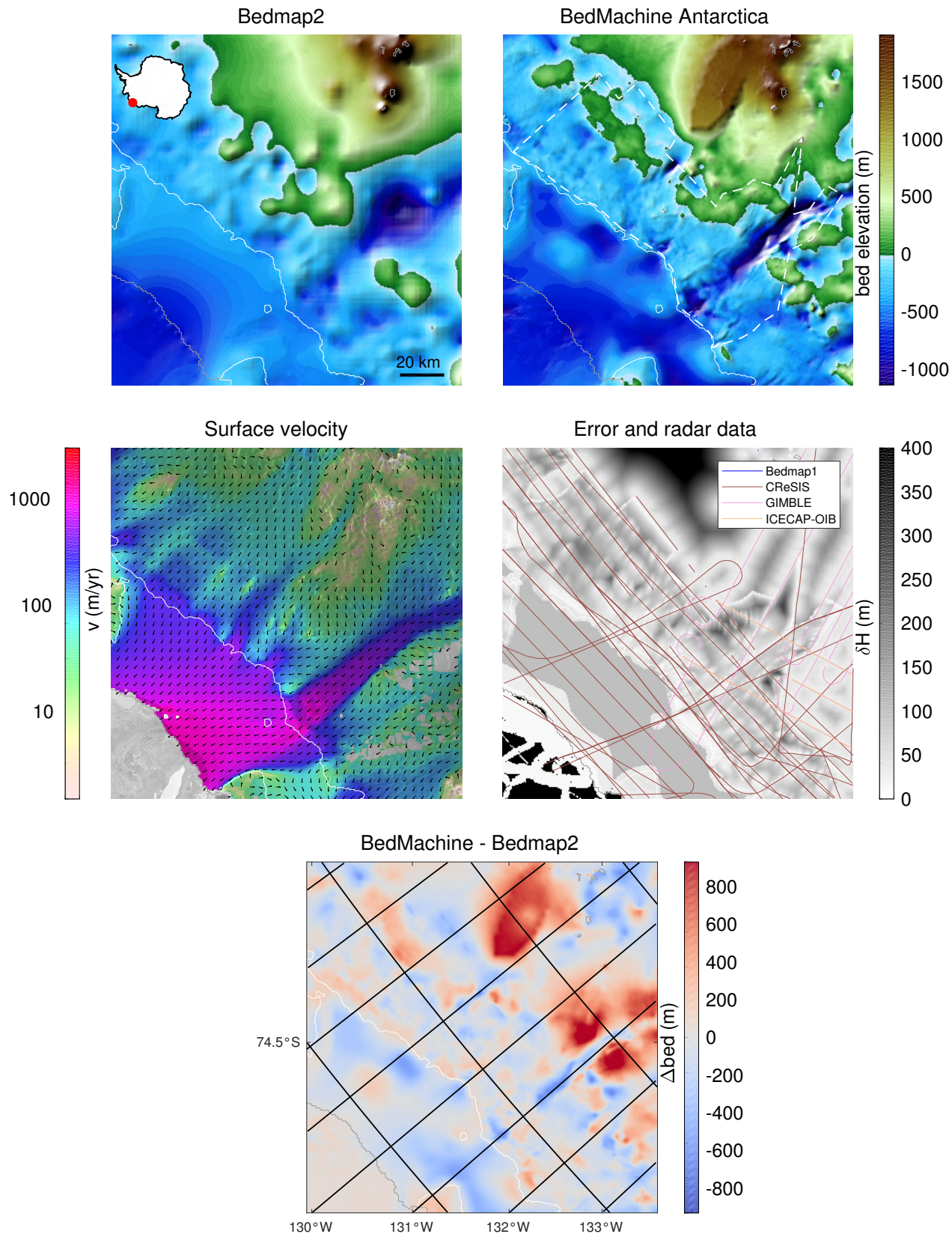


Figure S12: DeVicq Glacier

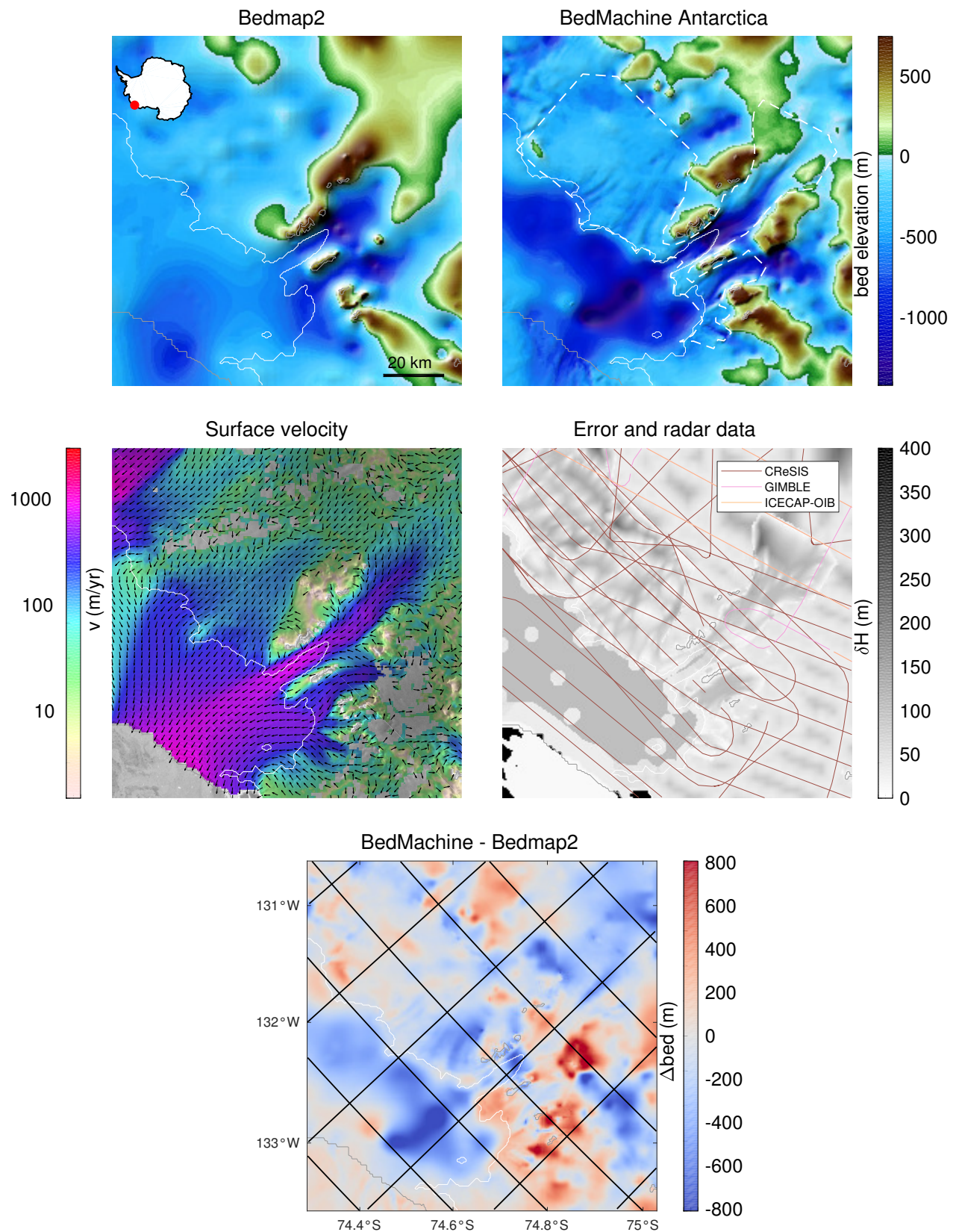


Figure S13: Berry Glacier

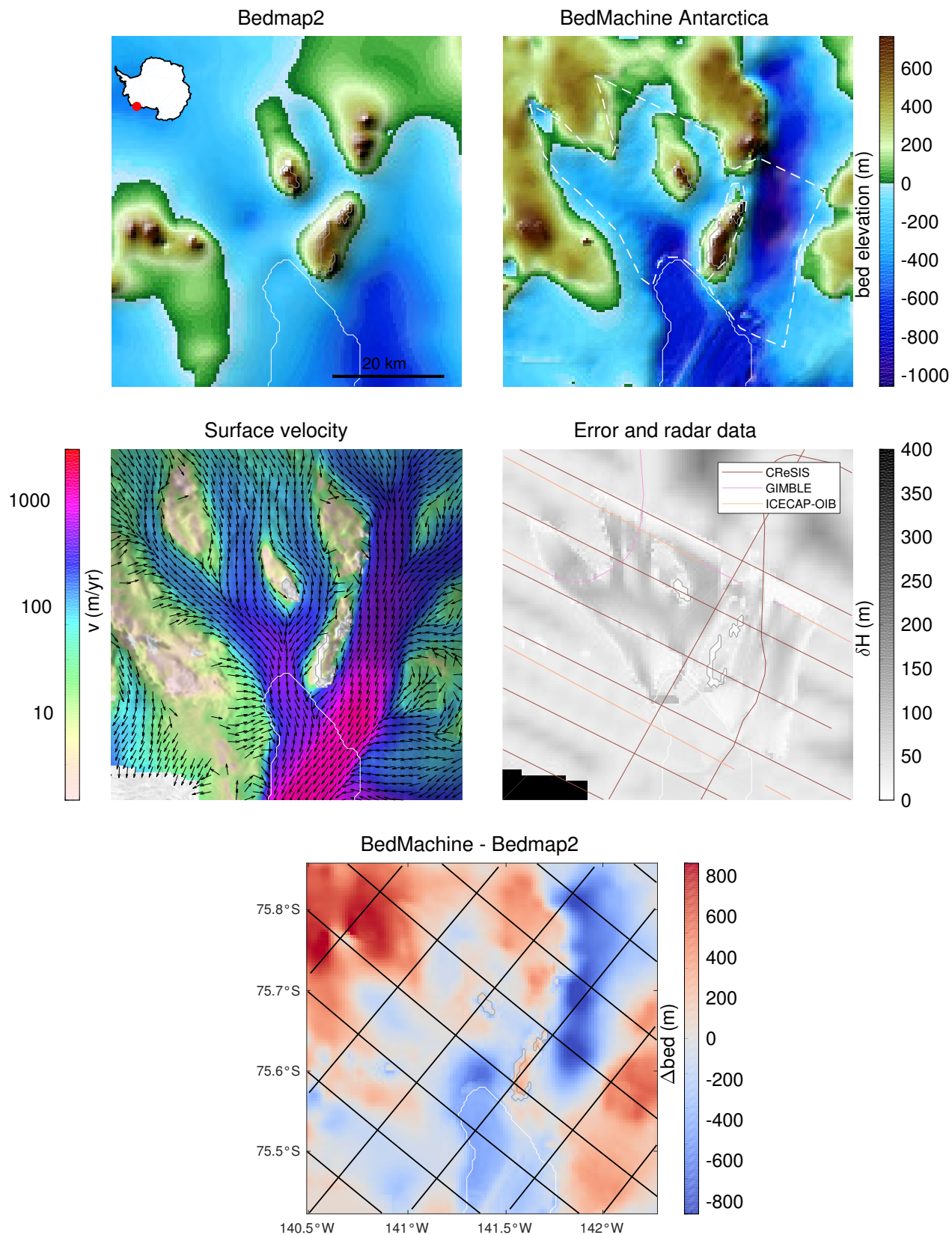


Figure S14: Land Glacier

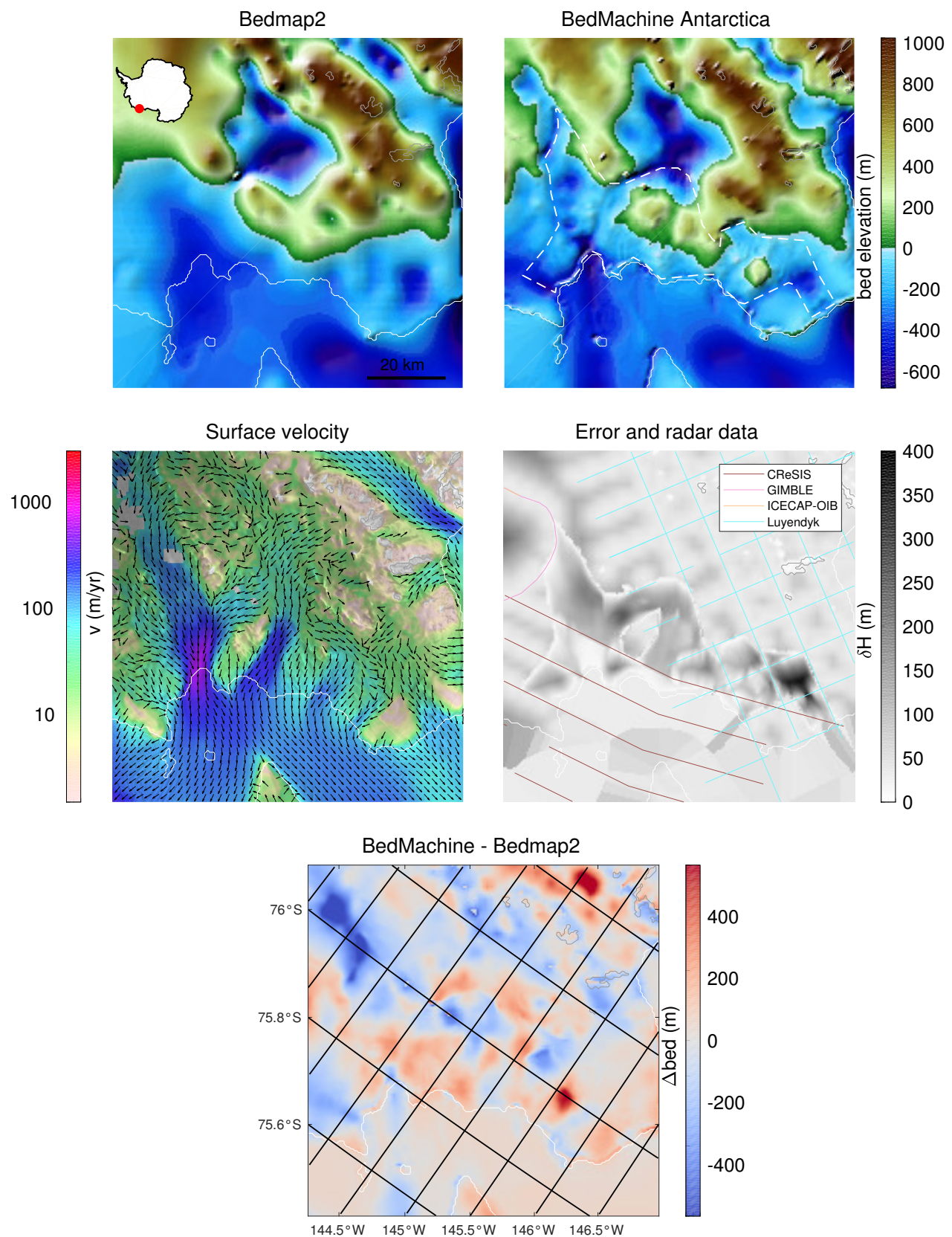


Figure S15: Nickerson Ice Shelf

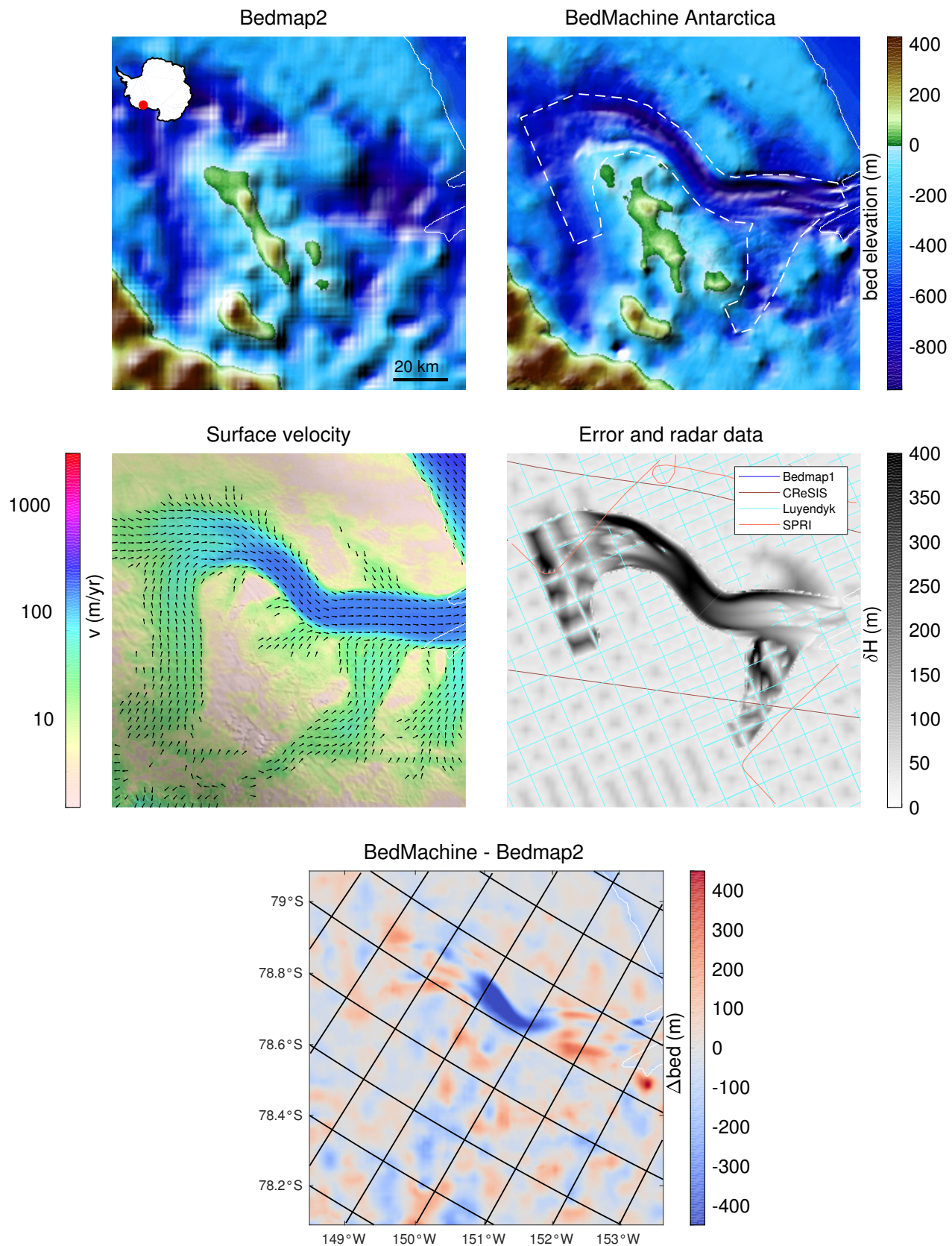


Figure S16: Echelmeyer Ice Stream (Ice Stream F)

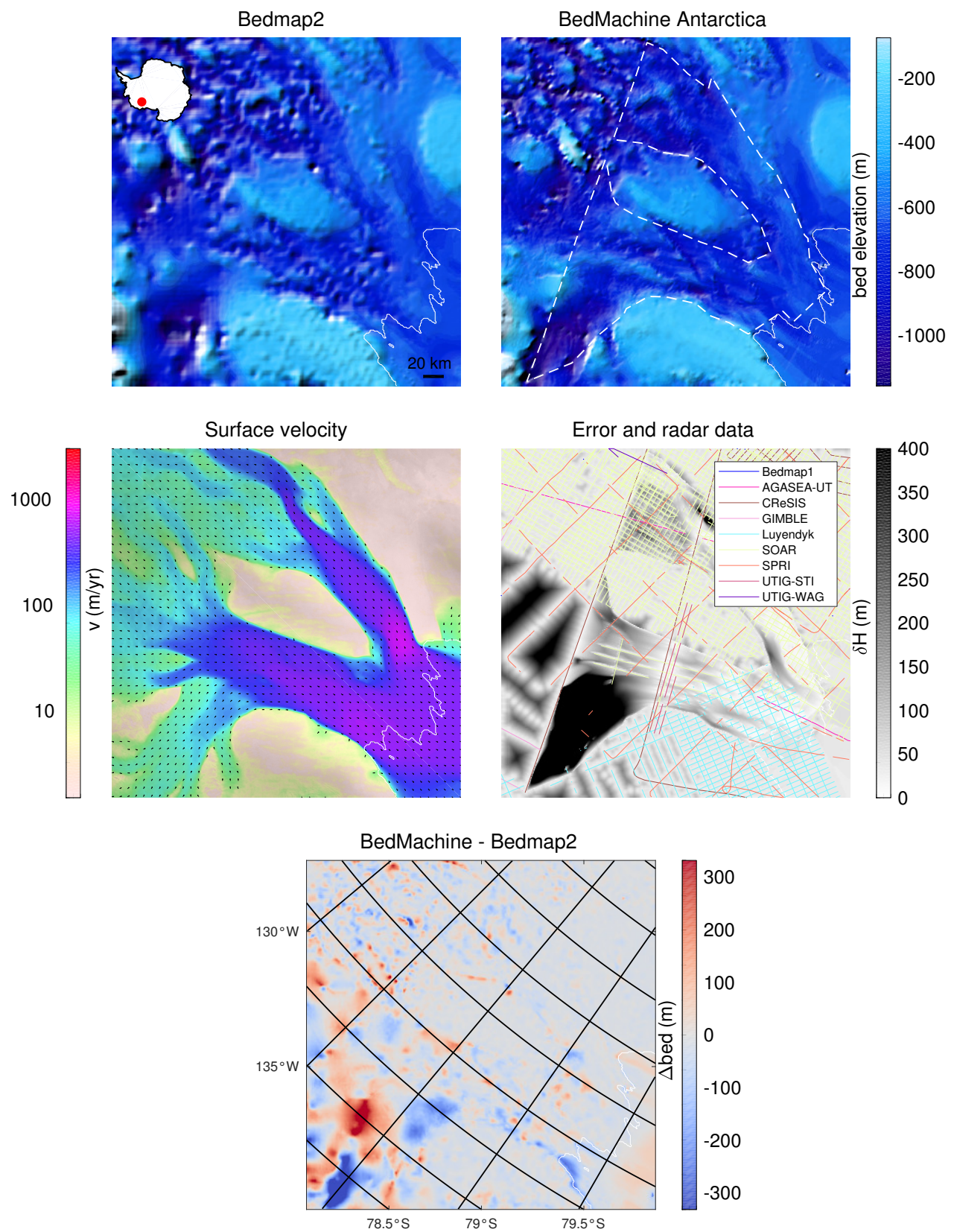


Figure S17: Siple Coast

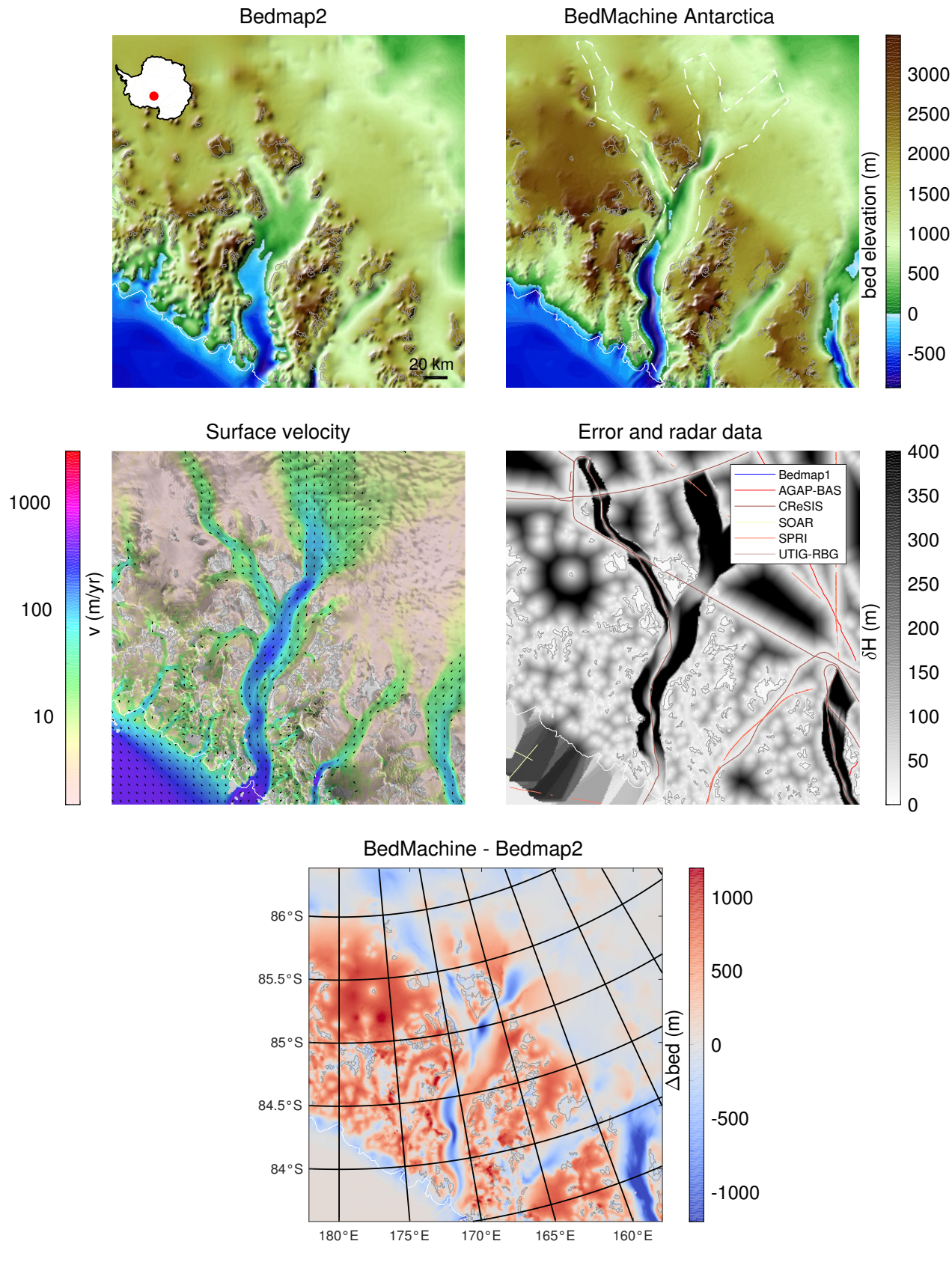


Figure S18: Beardmore Glacier

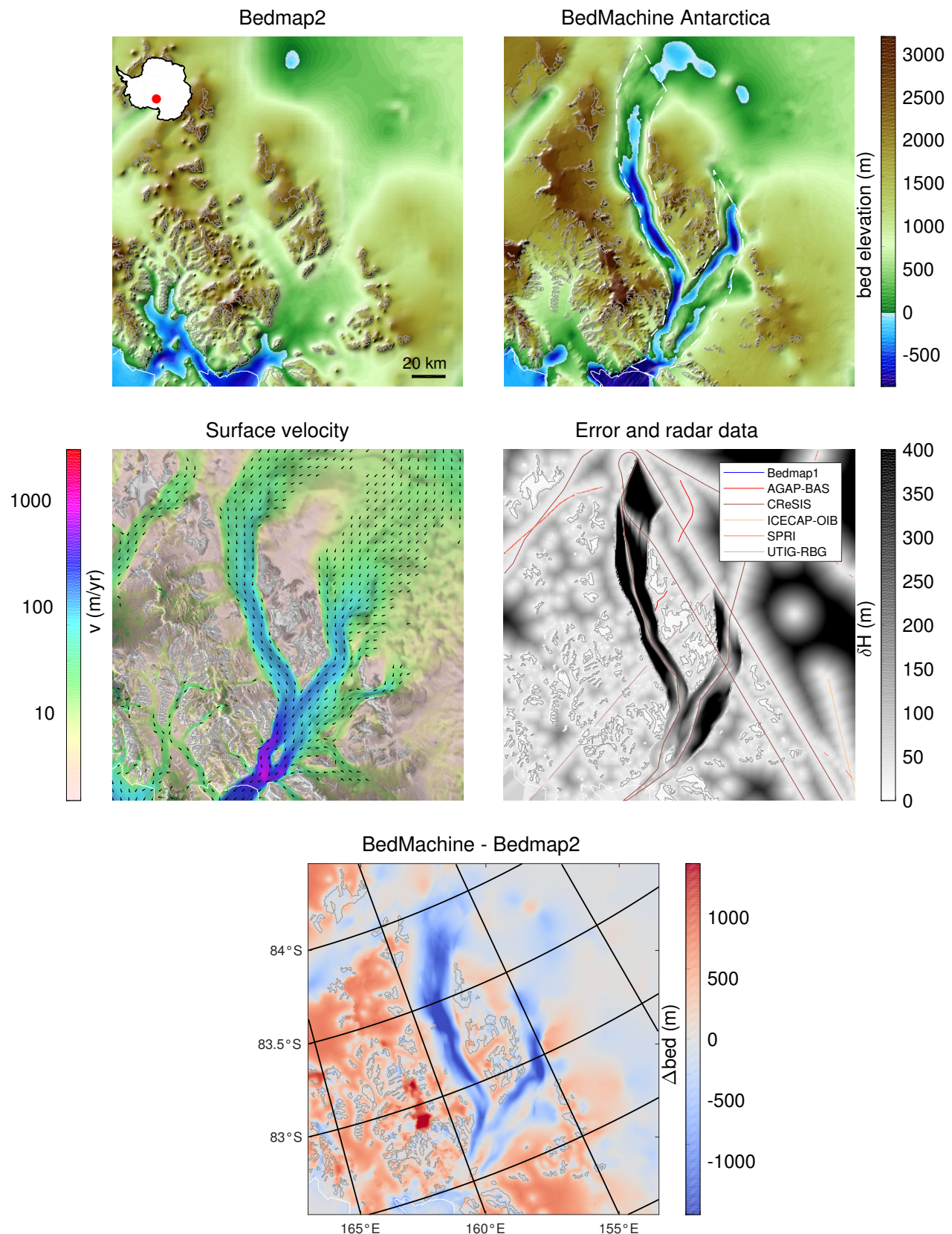


Figure S19: Nimrod Glacier

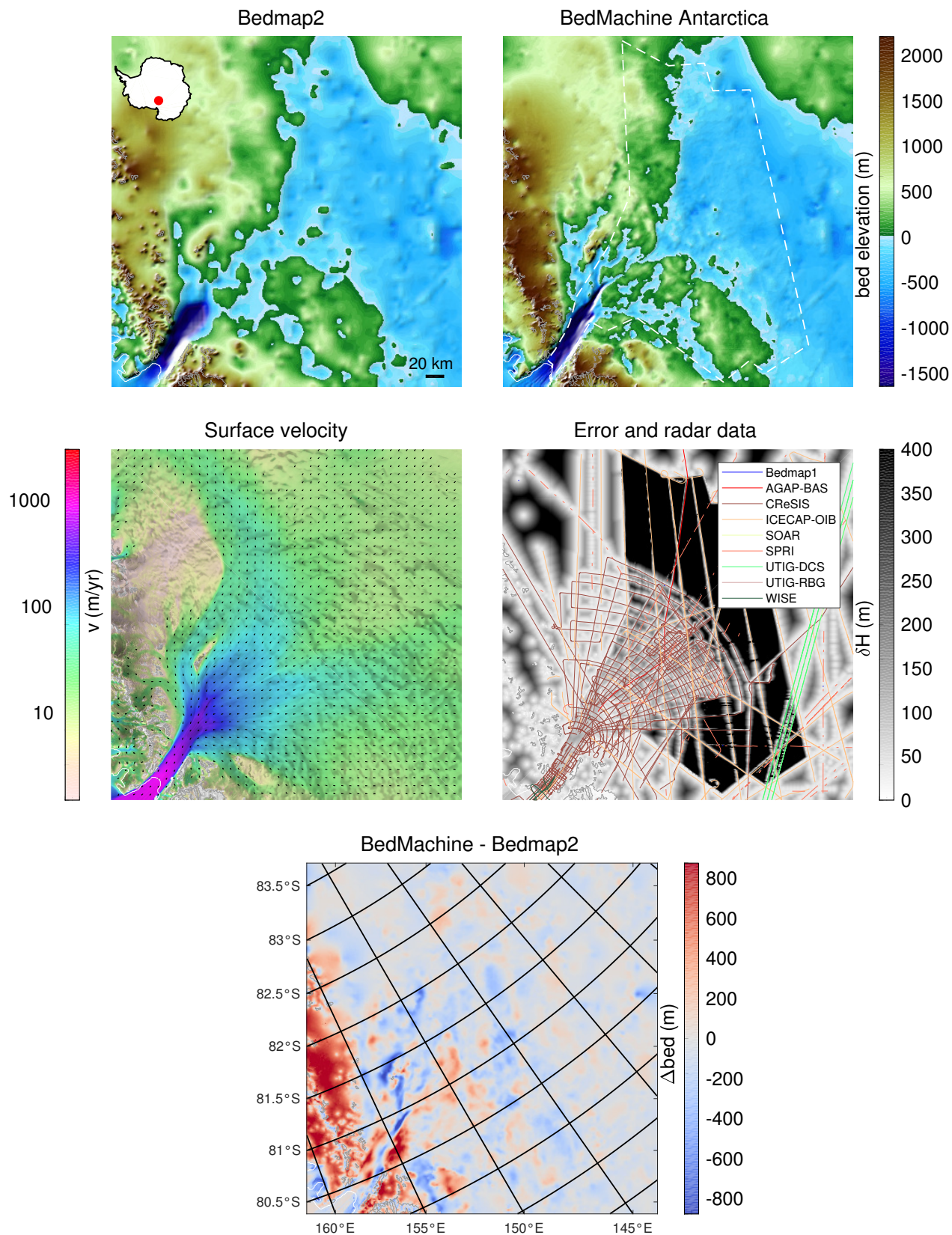


Figure S20: Byrd Glacier

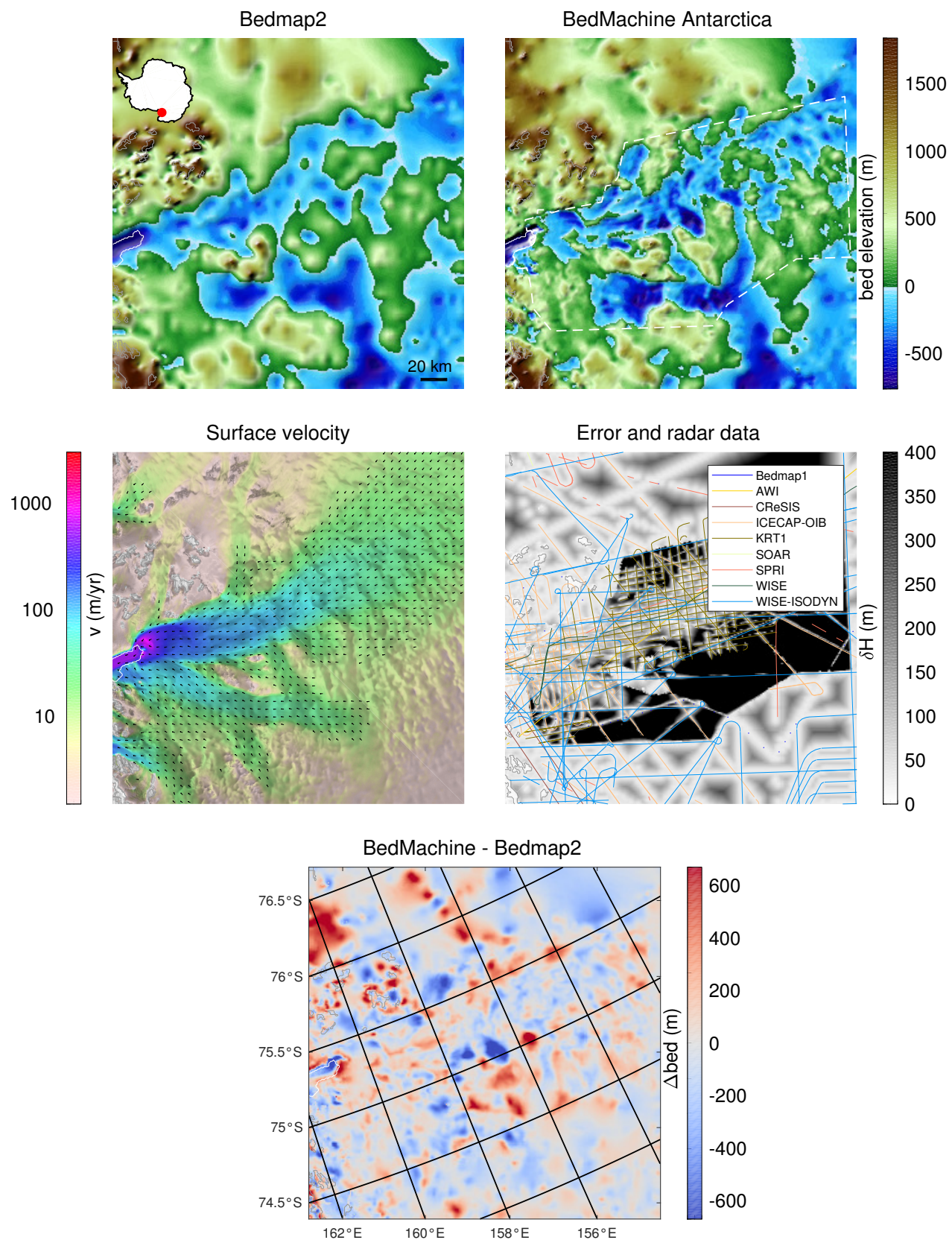


Figure S21: David Glacier

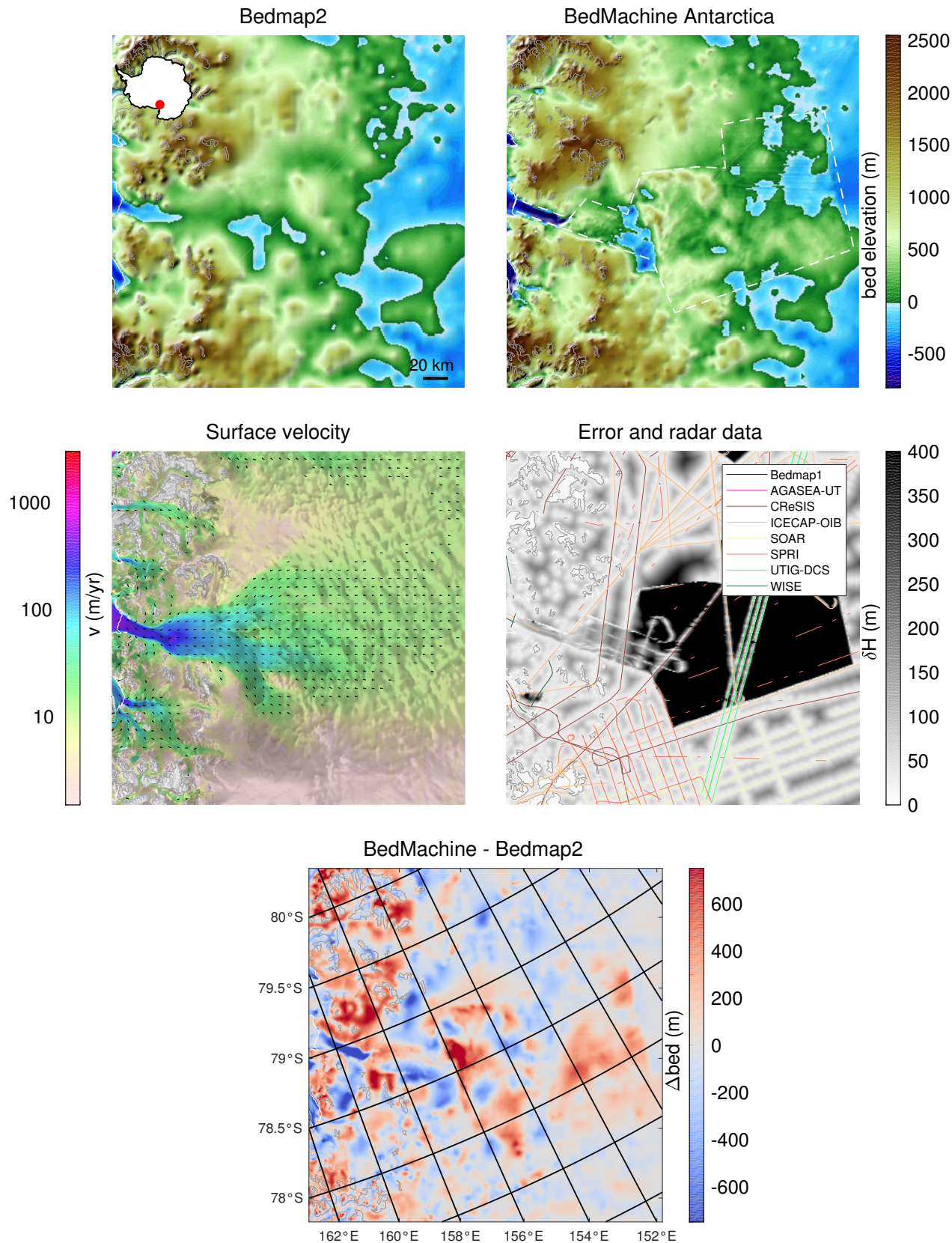


Figure S22: Mulock Glacier

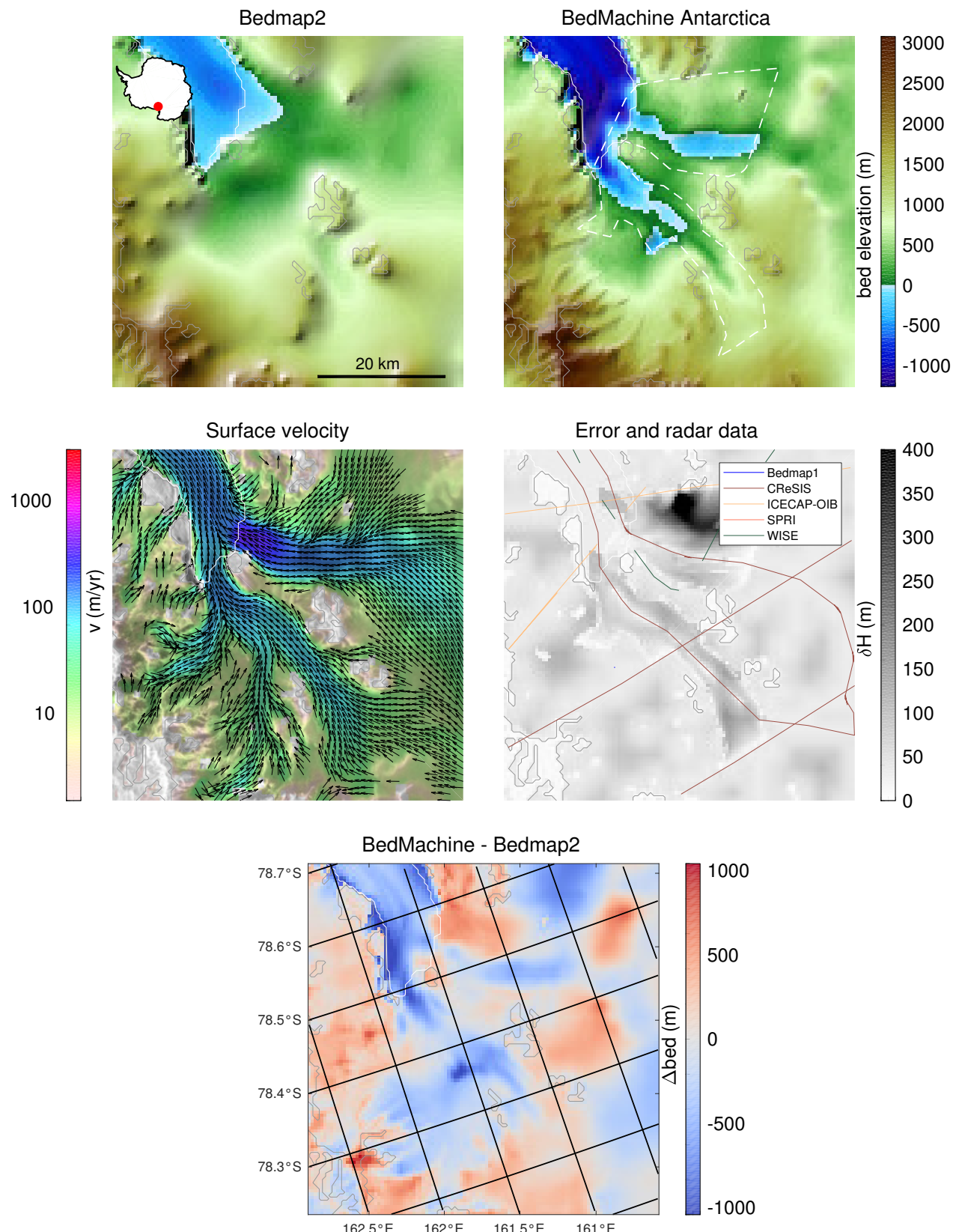


Figure S23: Skelton Glacier

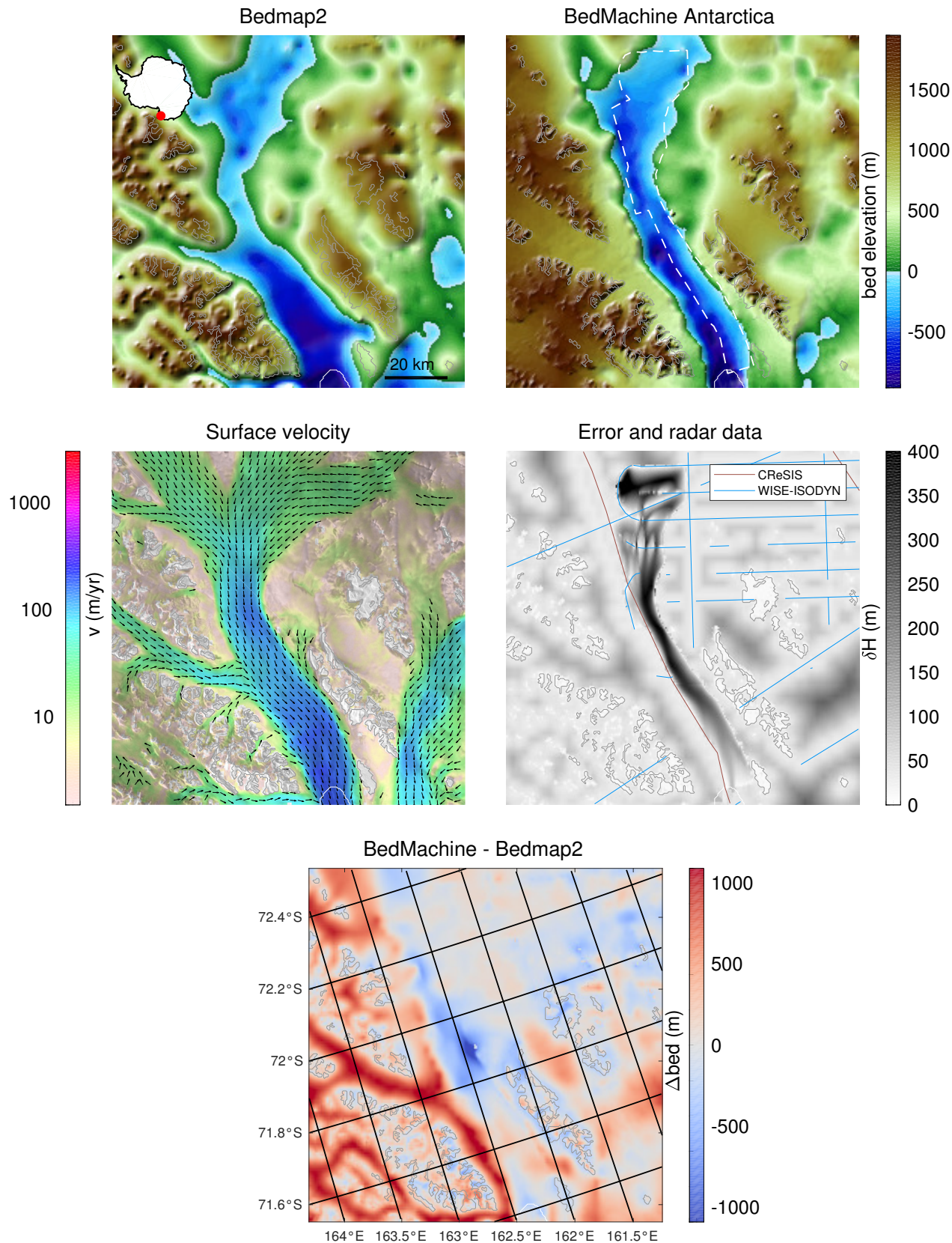


Figure S24: Sullivan Glacier

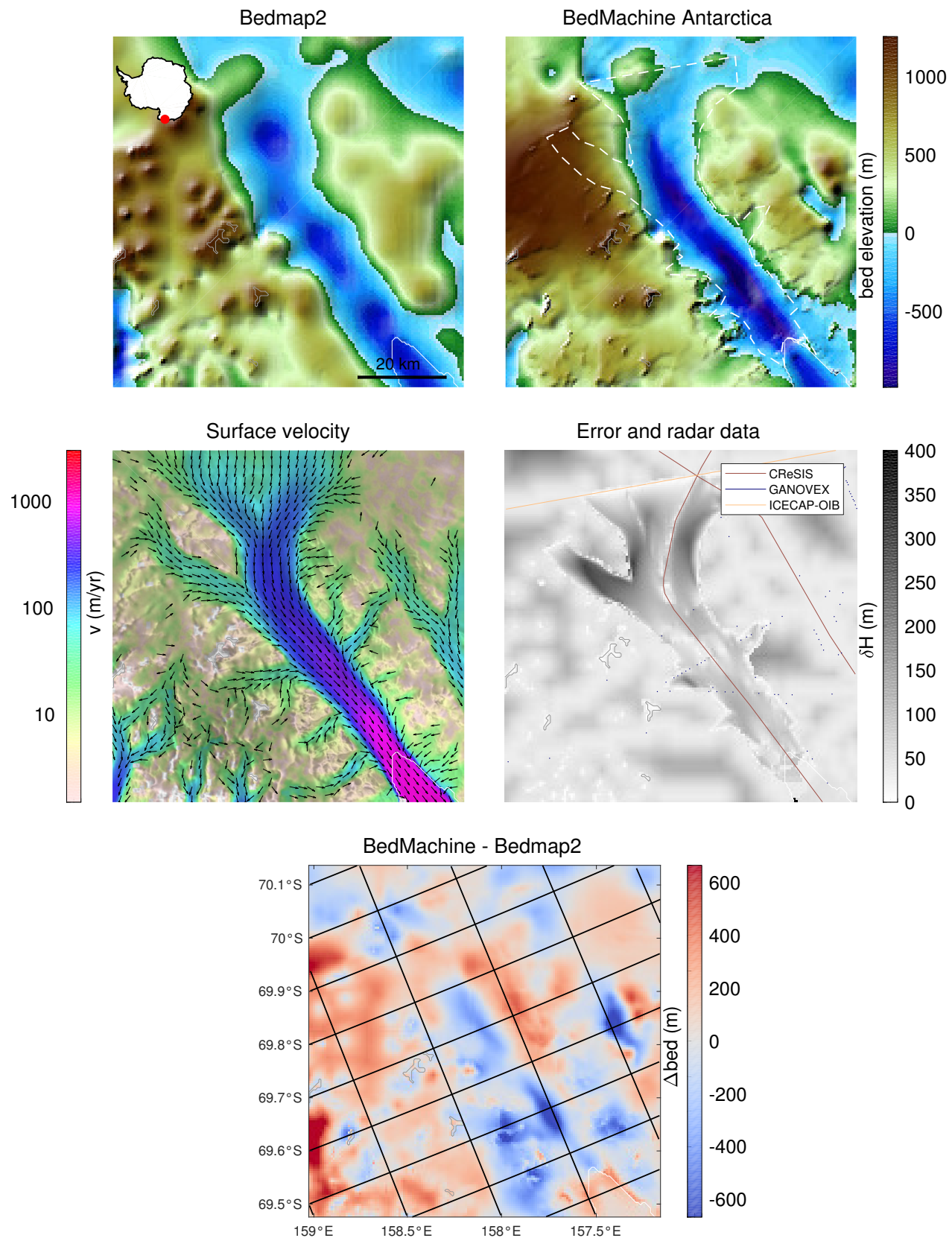


Figure S25: Matusevich Glacier

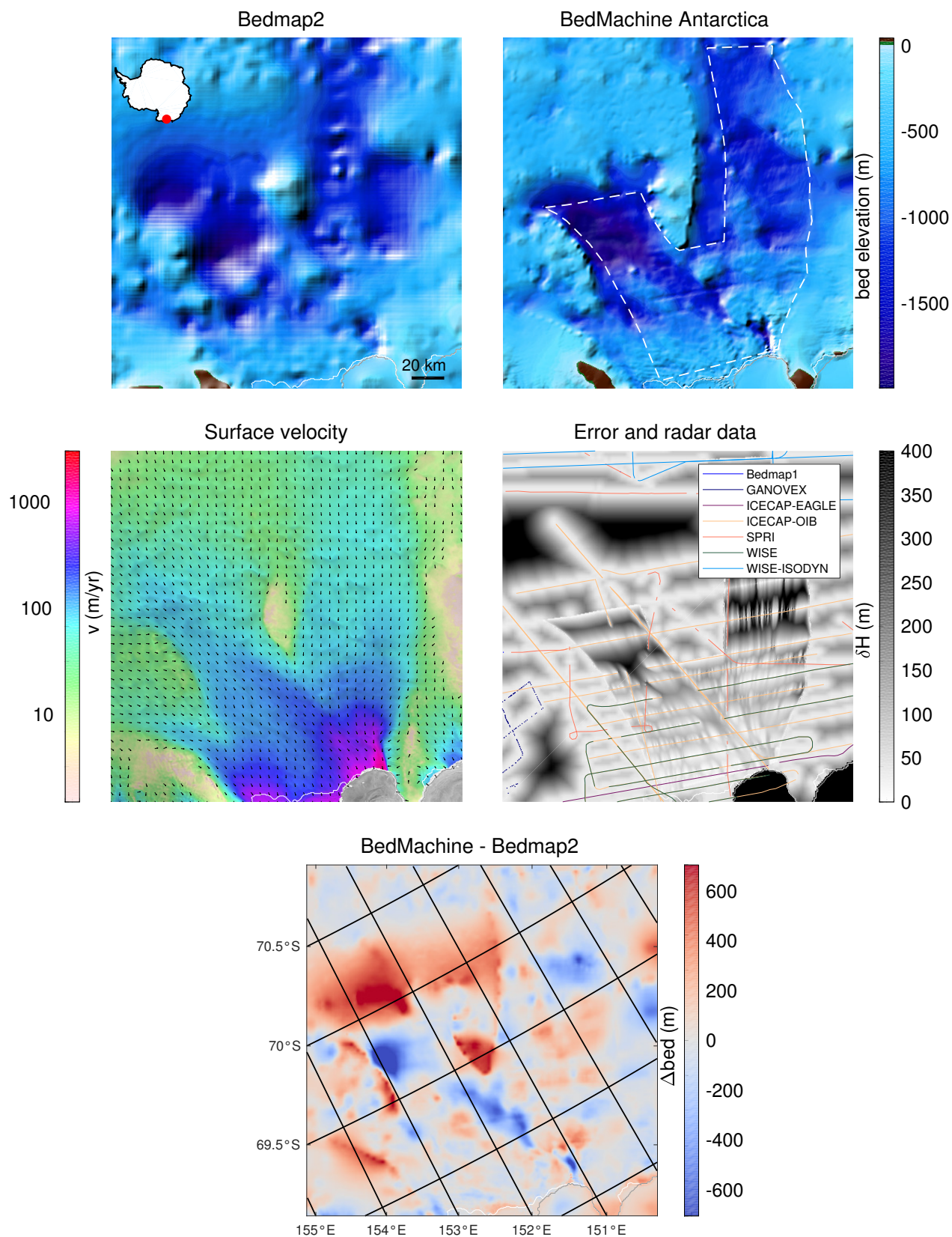


Figure S26: Cook Ice Shelf

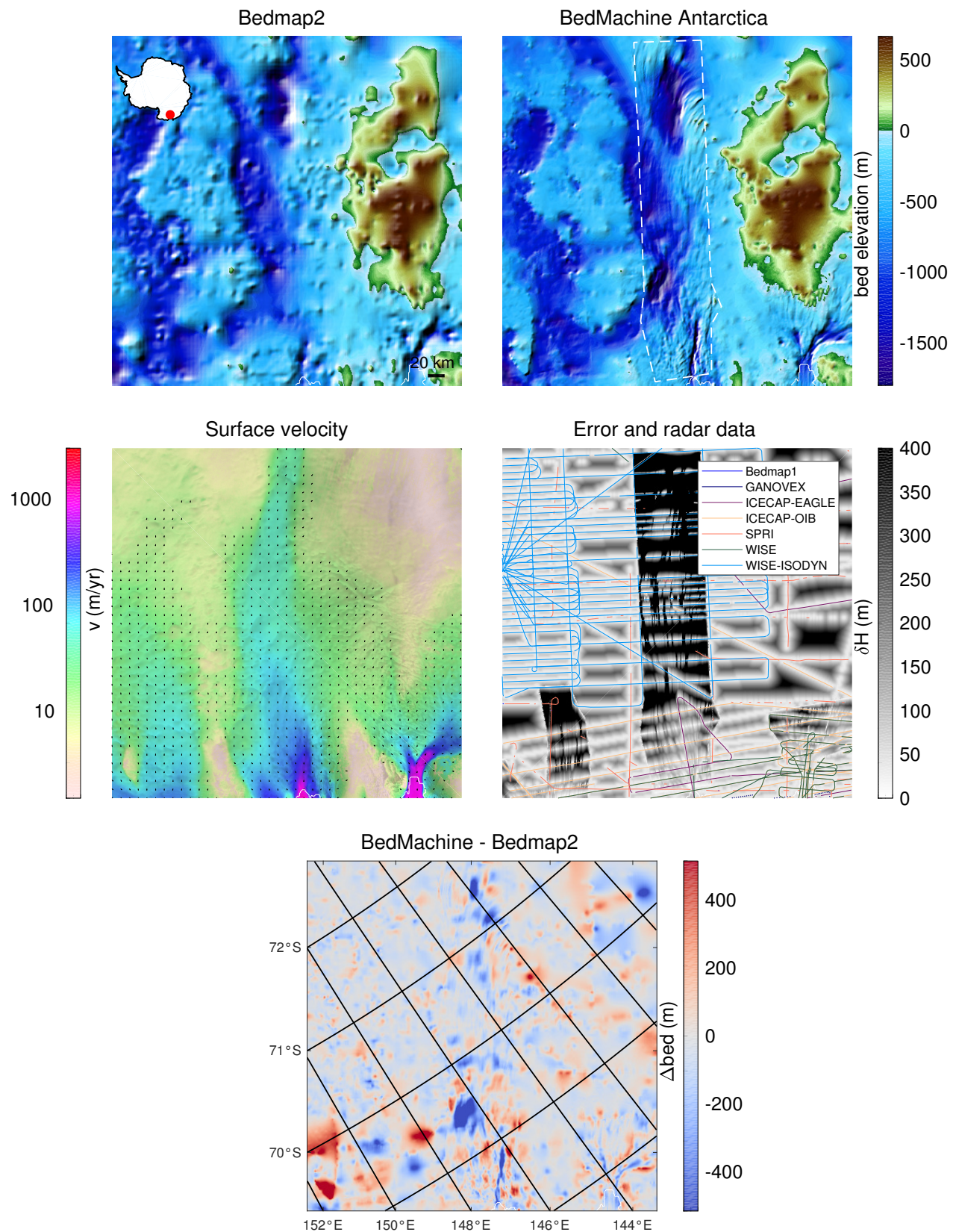


Figure S27: Ninnis Ice Shelf

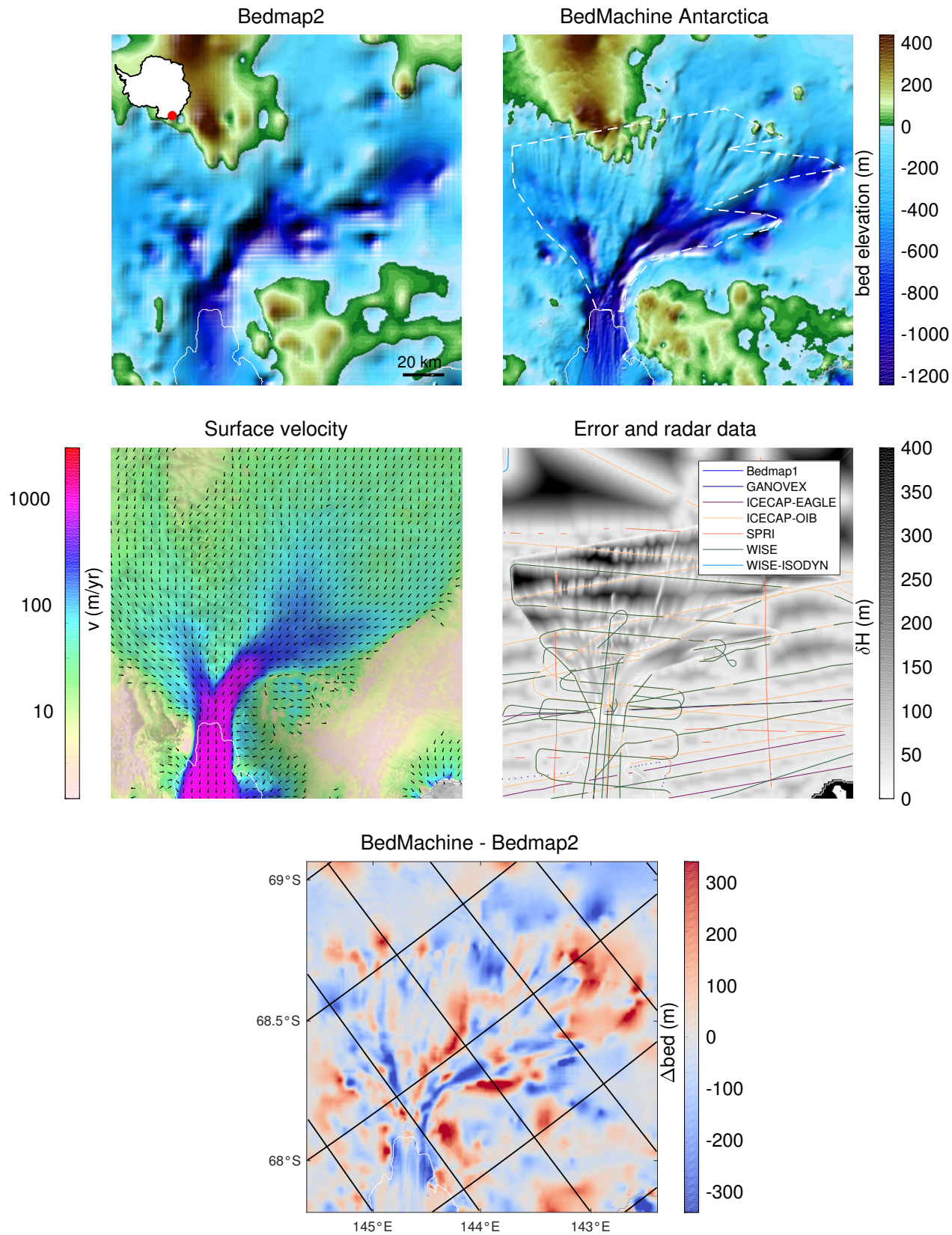


Figure S28: Mertz Glacier

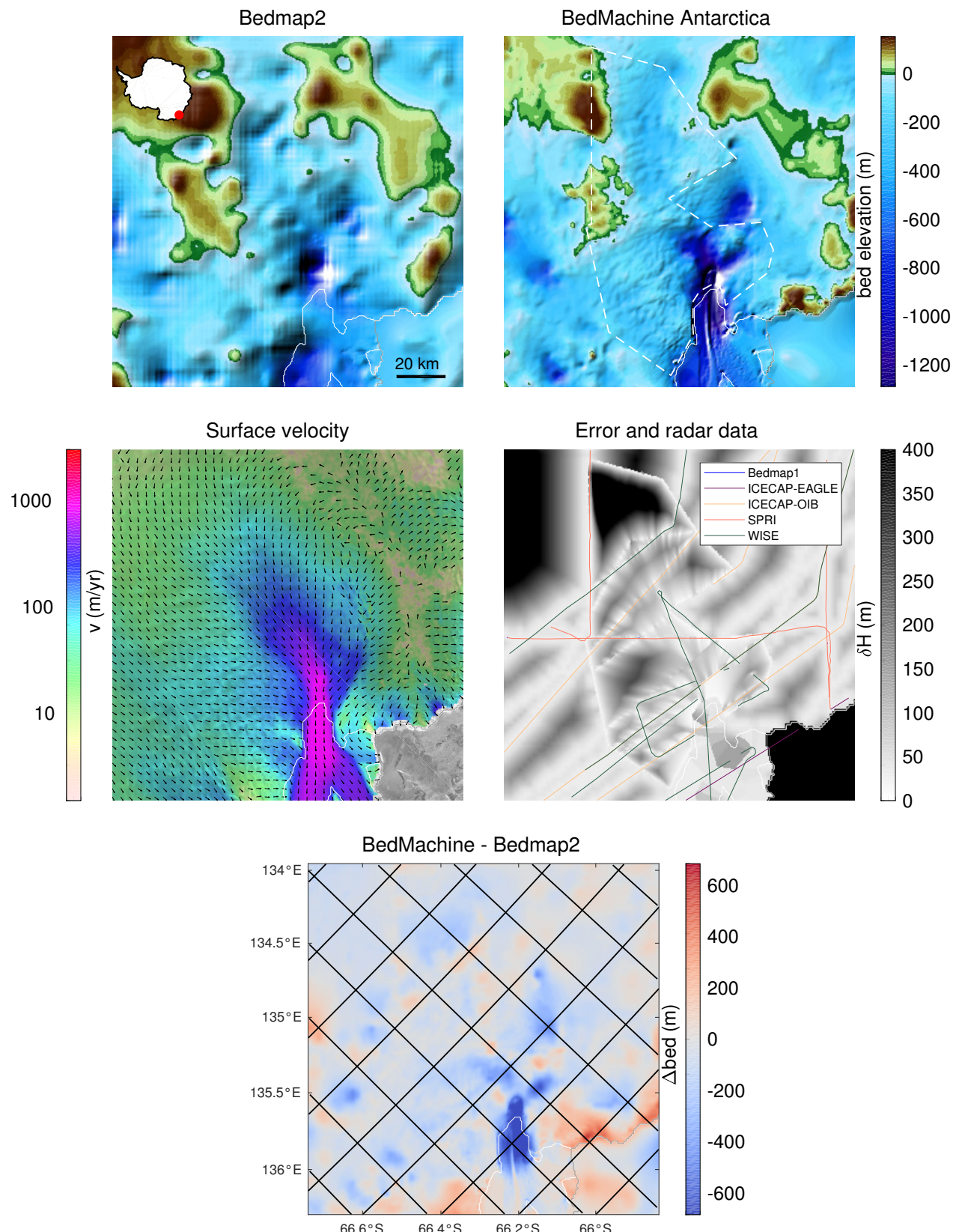


Figure S29: Dibble Glacier

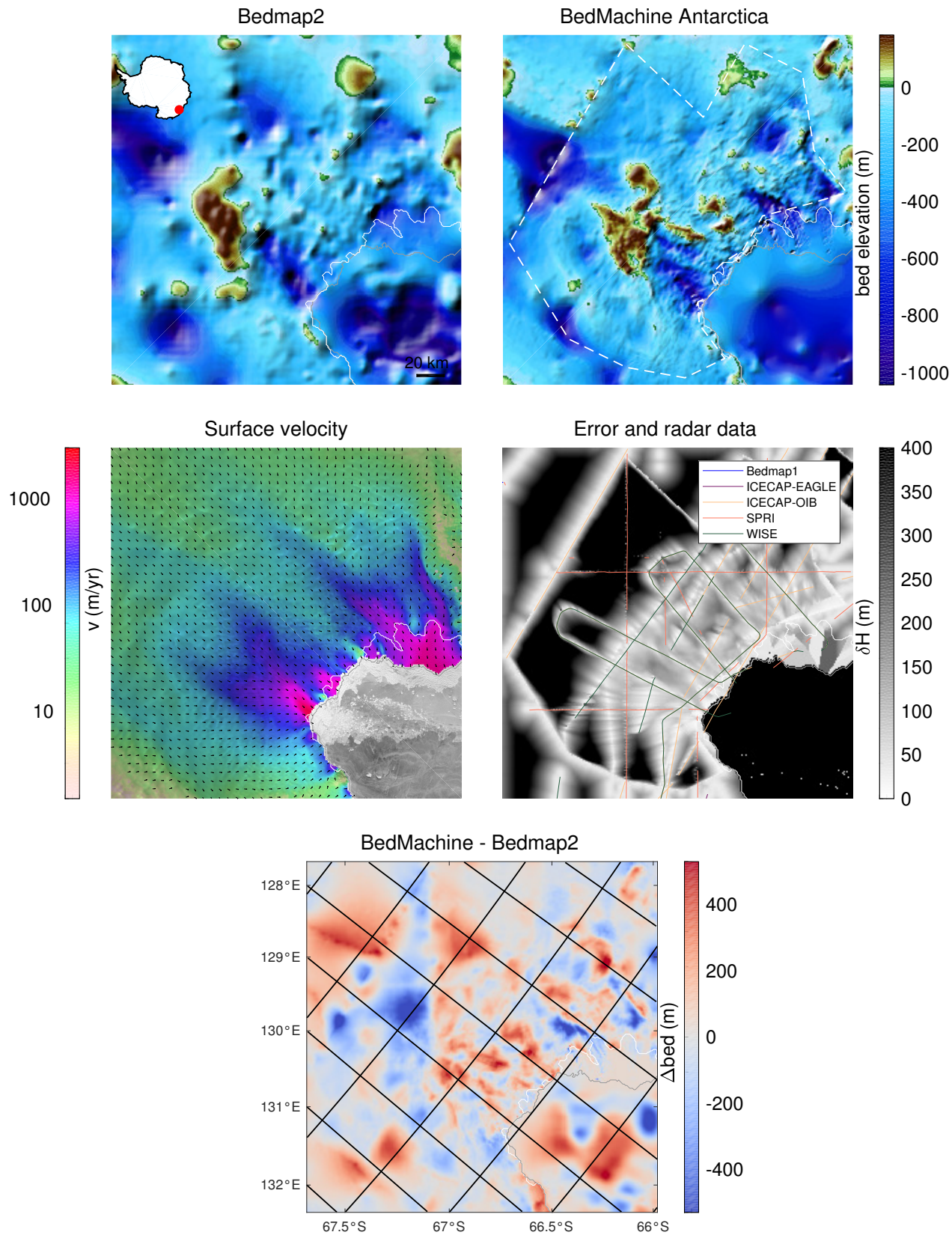


Figure S30: Frost Glacier

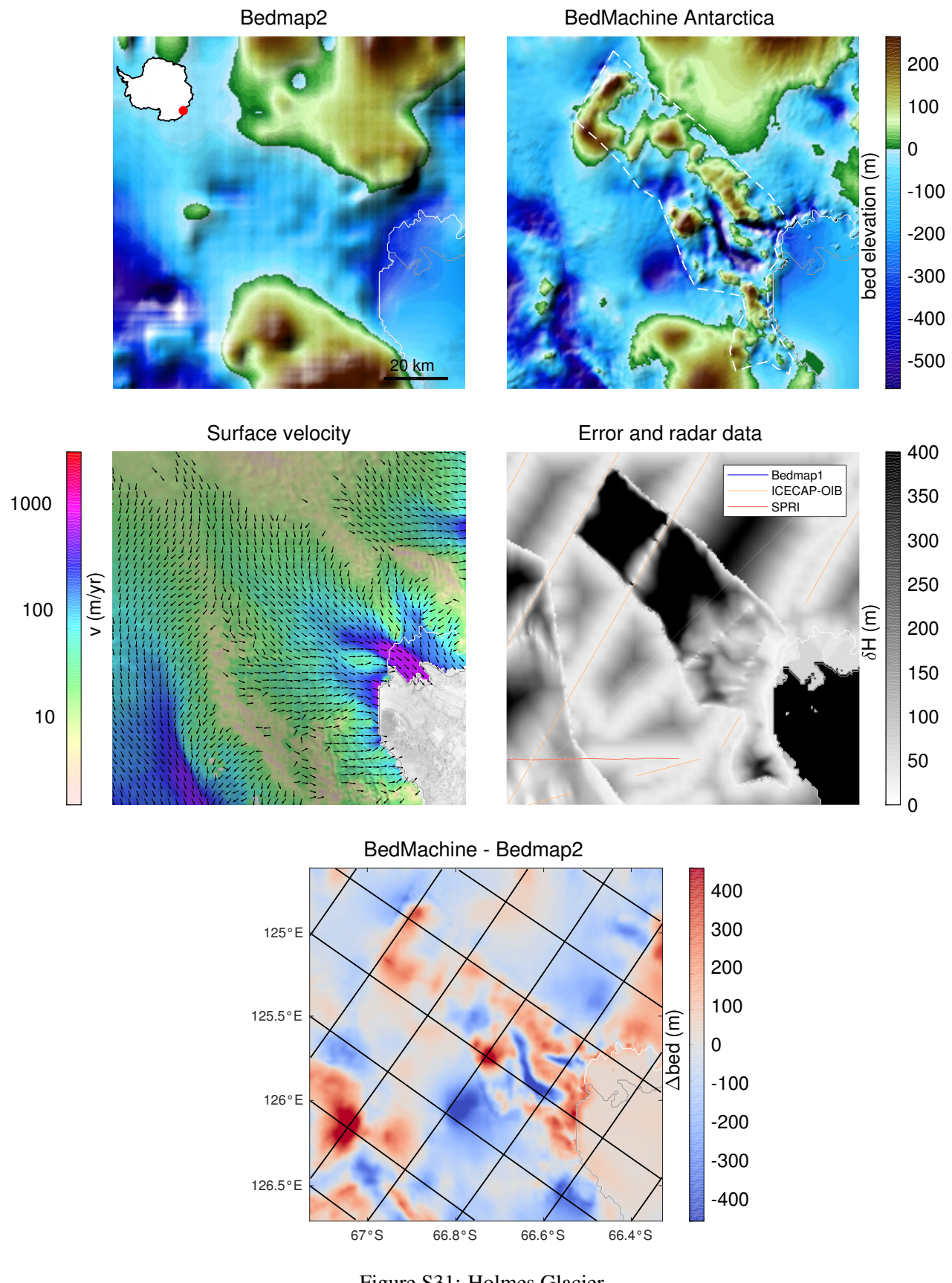


Figure S31: Holmes Glacier

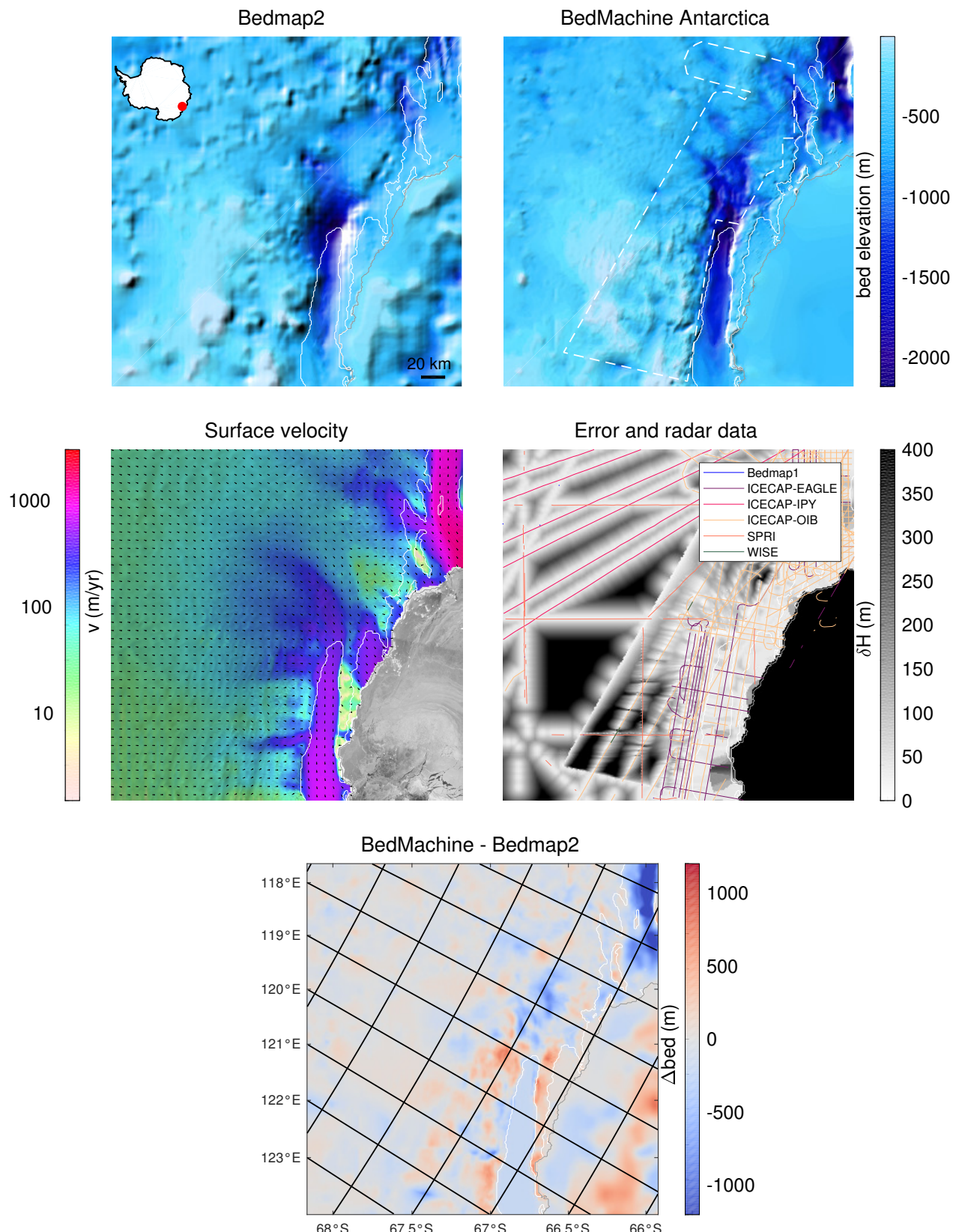


Figure S32: Moscow University Ice Shelf

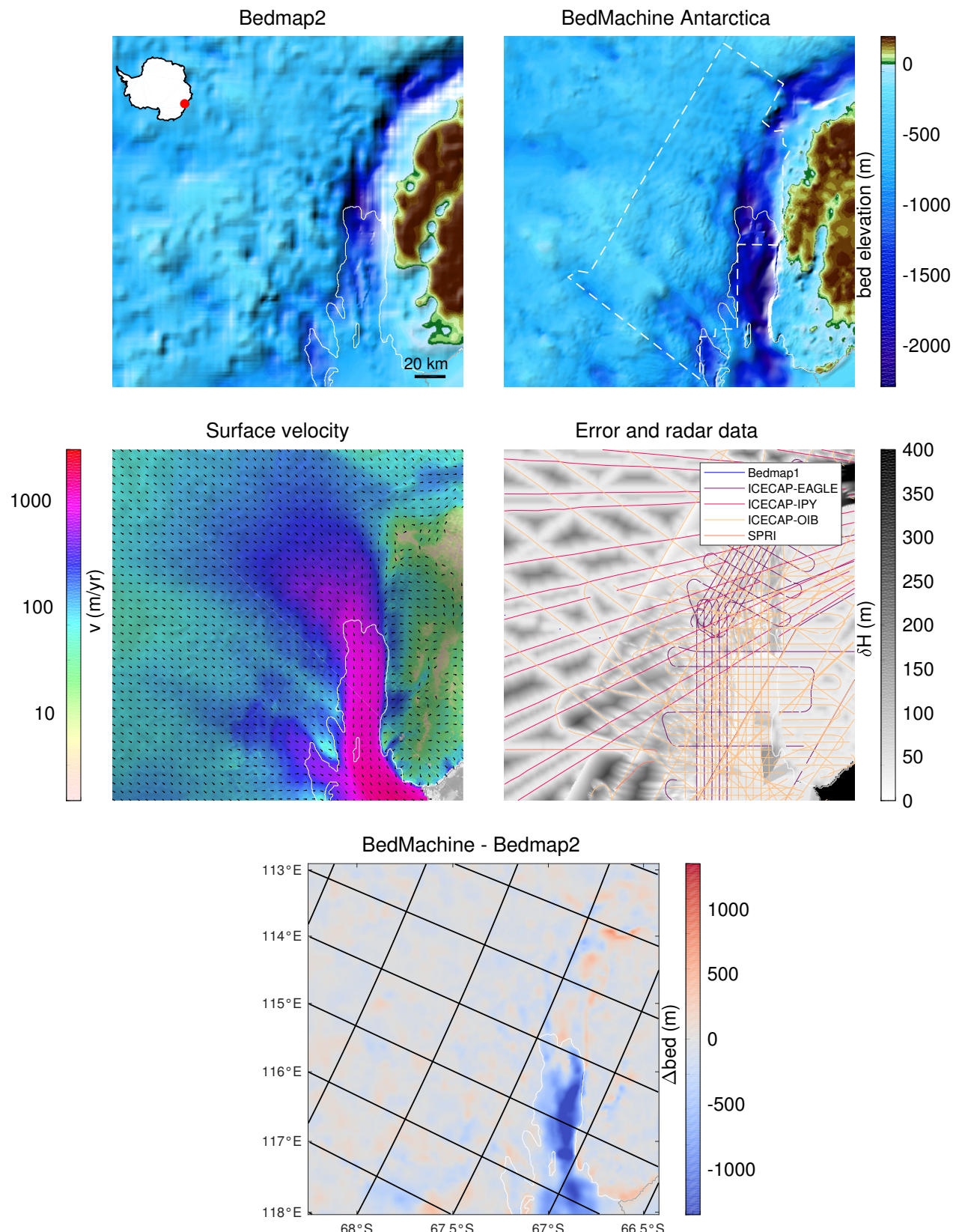


Figure S33: Totten Glacier

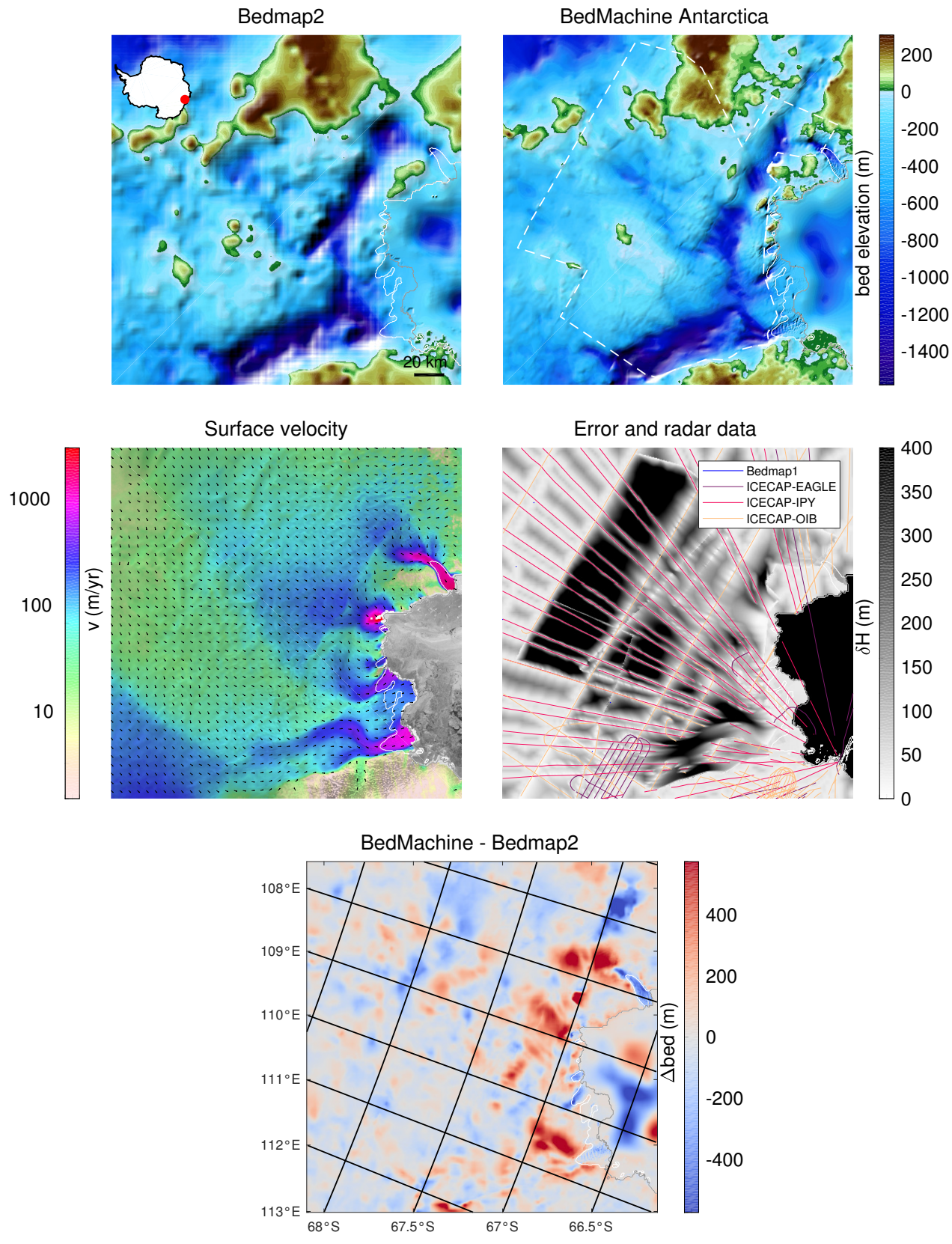


Figure S34: Williamson Glacier

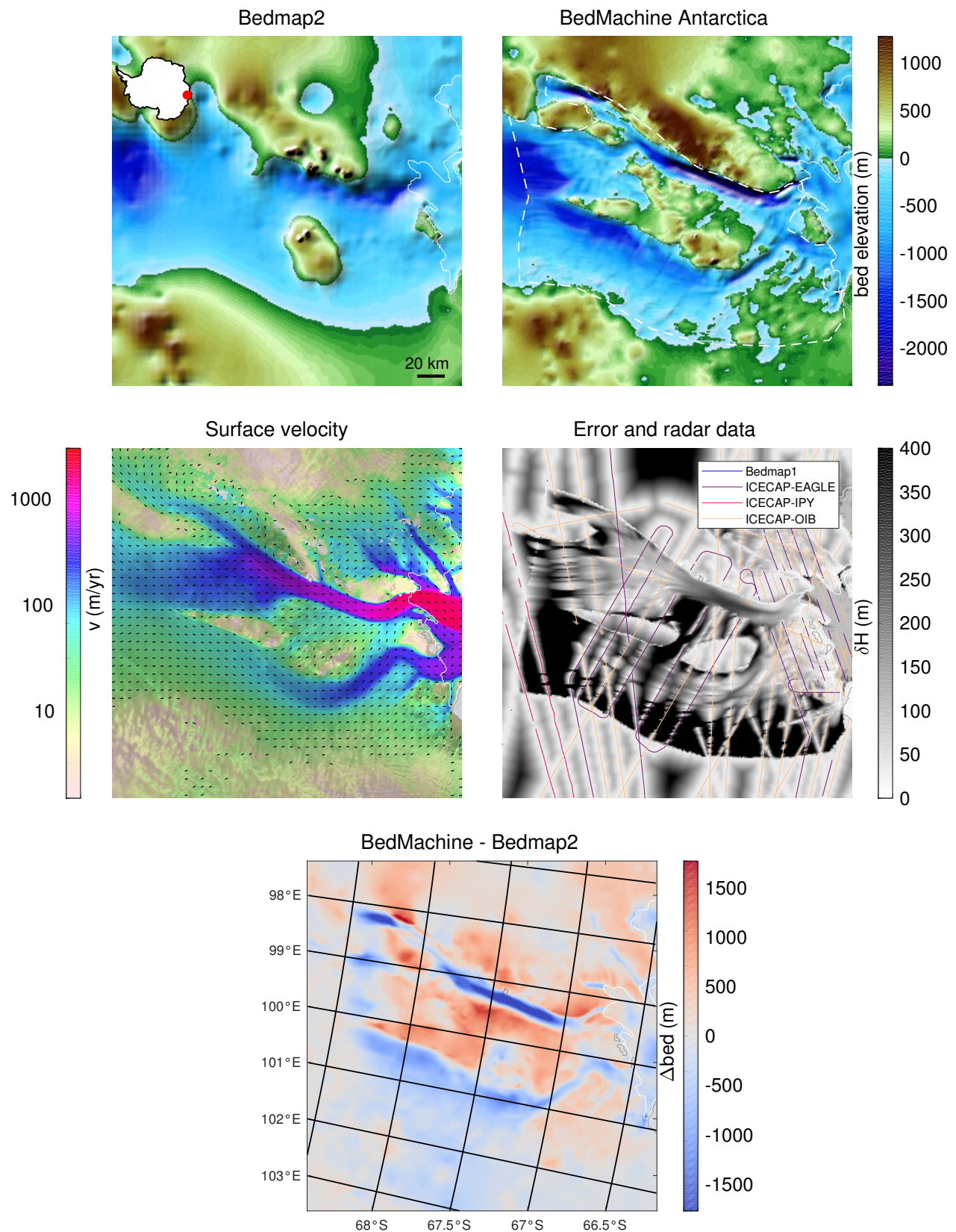


Figure S35: Denman Glacier

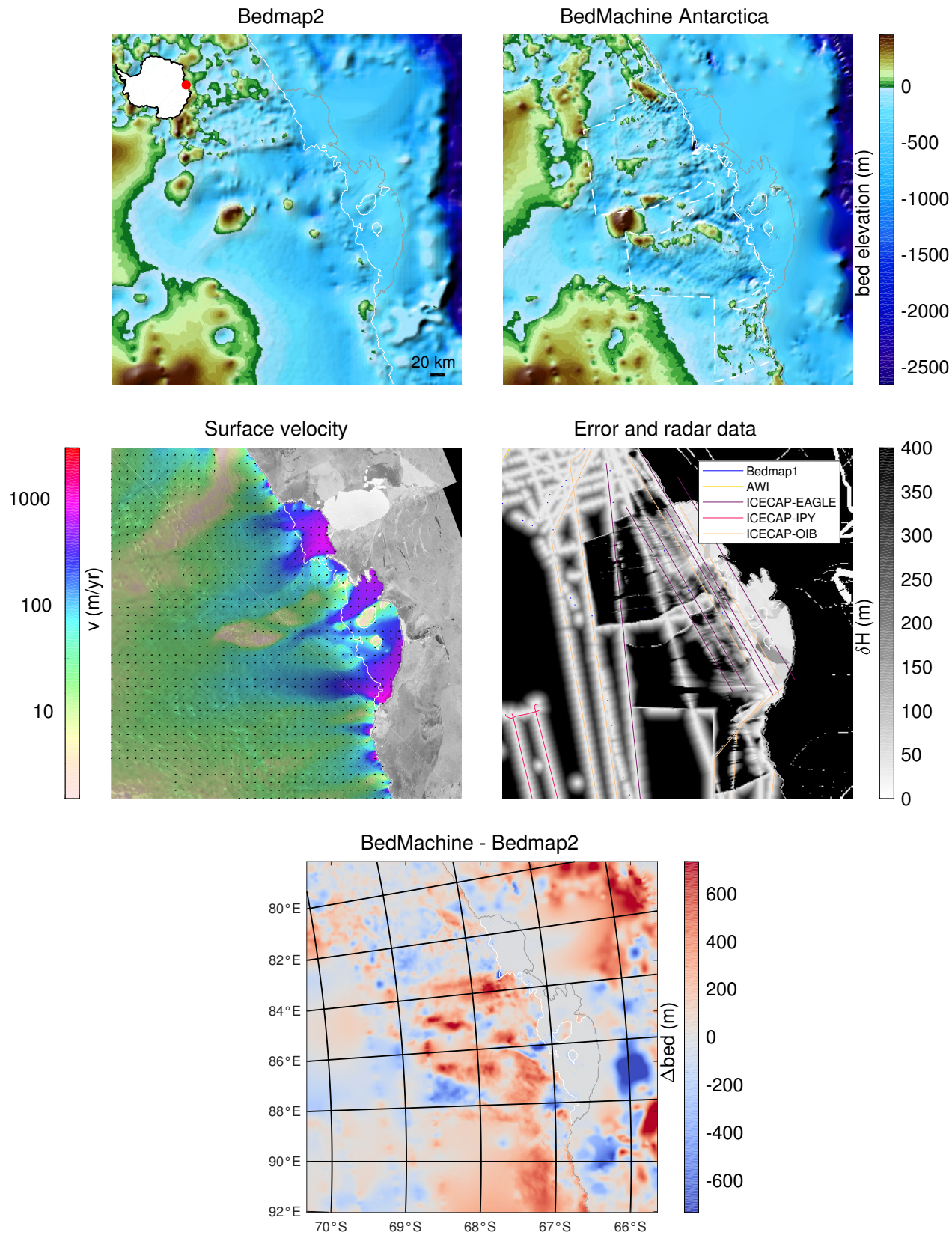


Figure S36: West Ice shelf

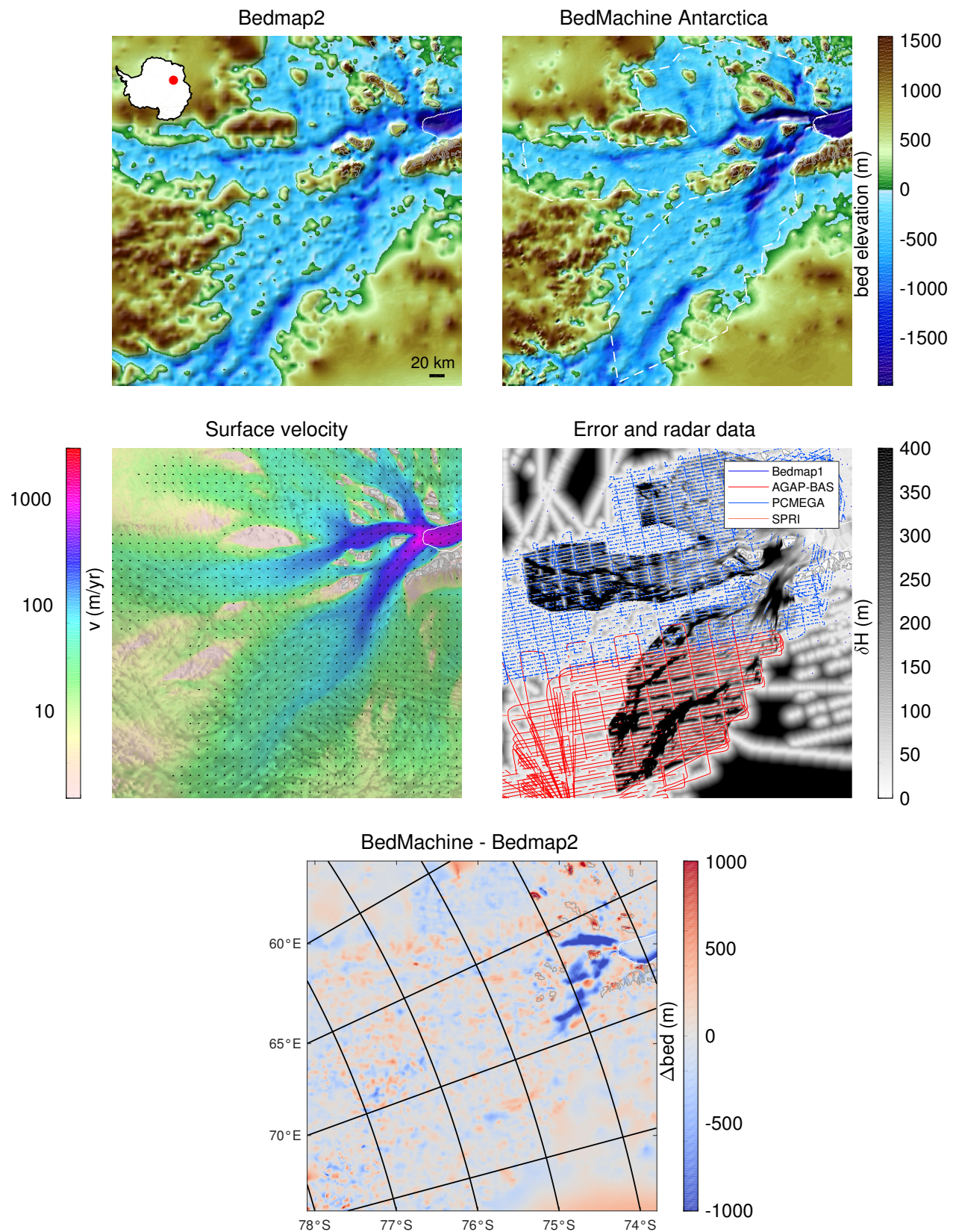


Figure S37: Lambert Glacier

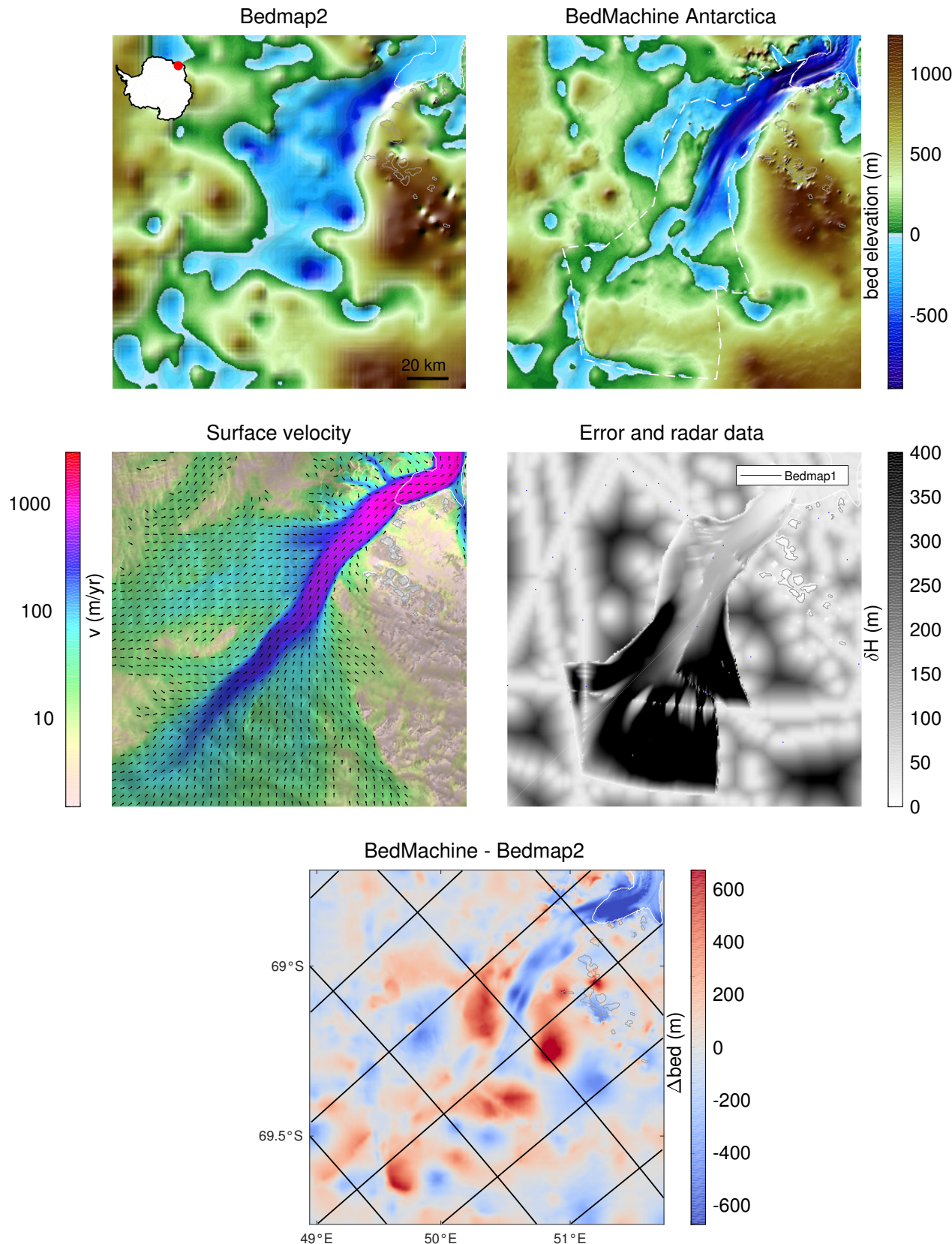


Figure S38: Rayner Glacier

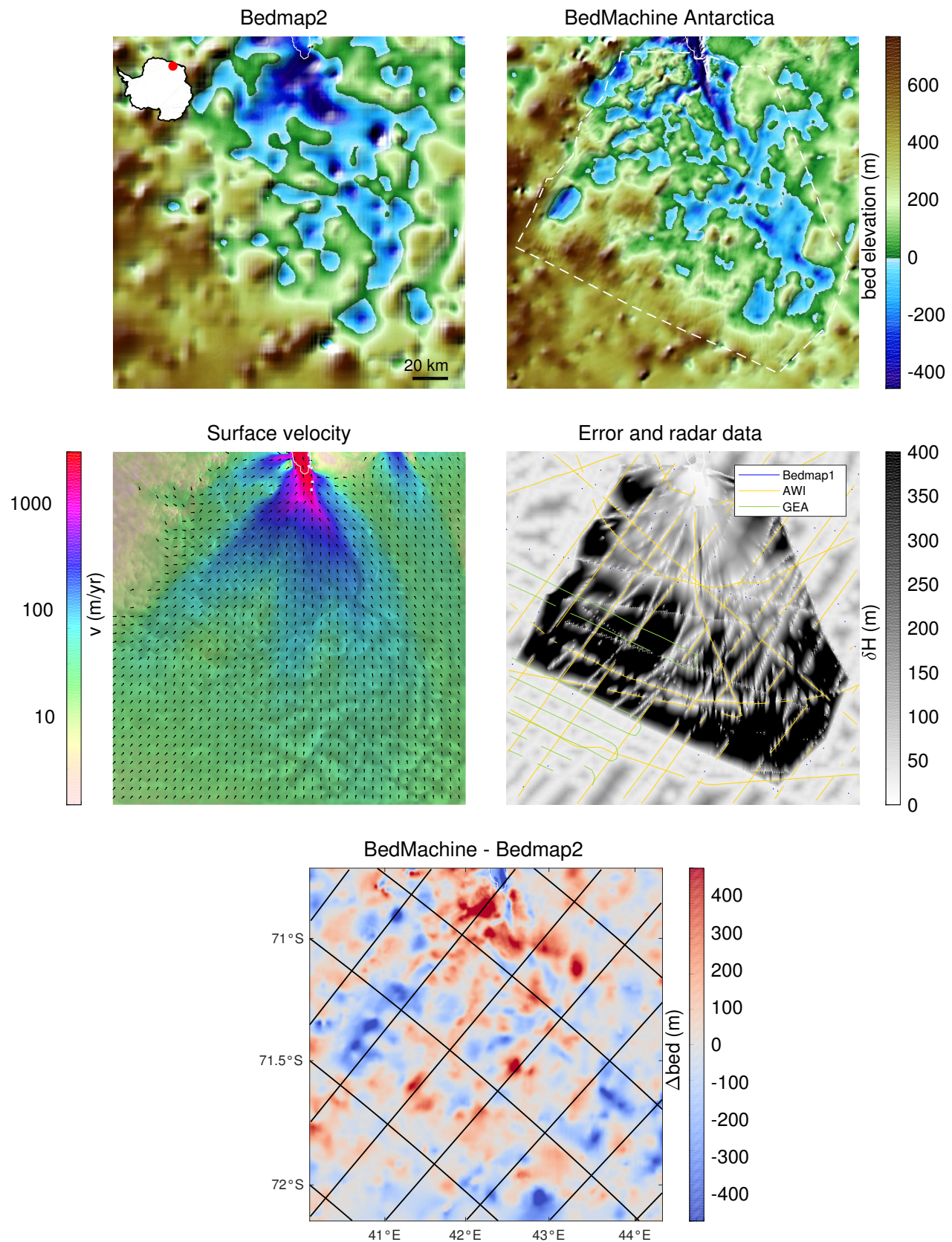


Figure S39: Shirase Glacier

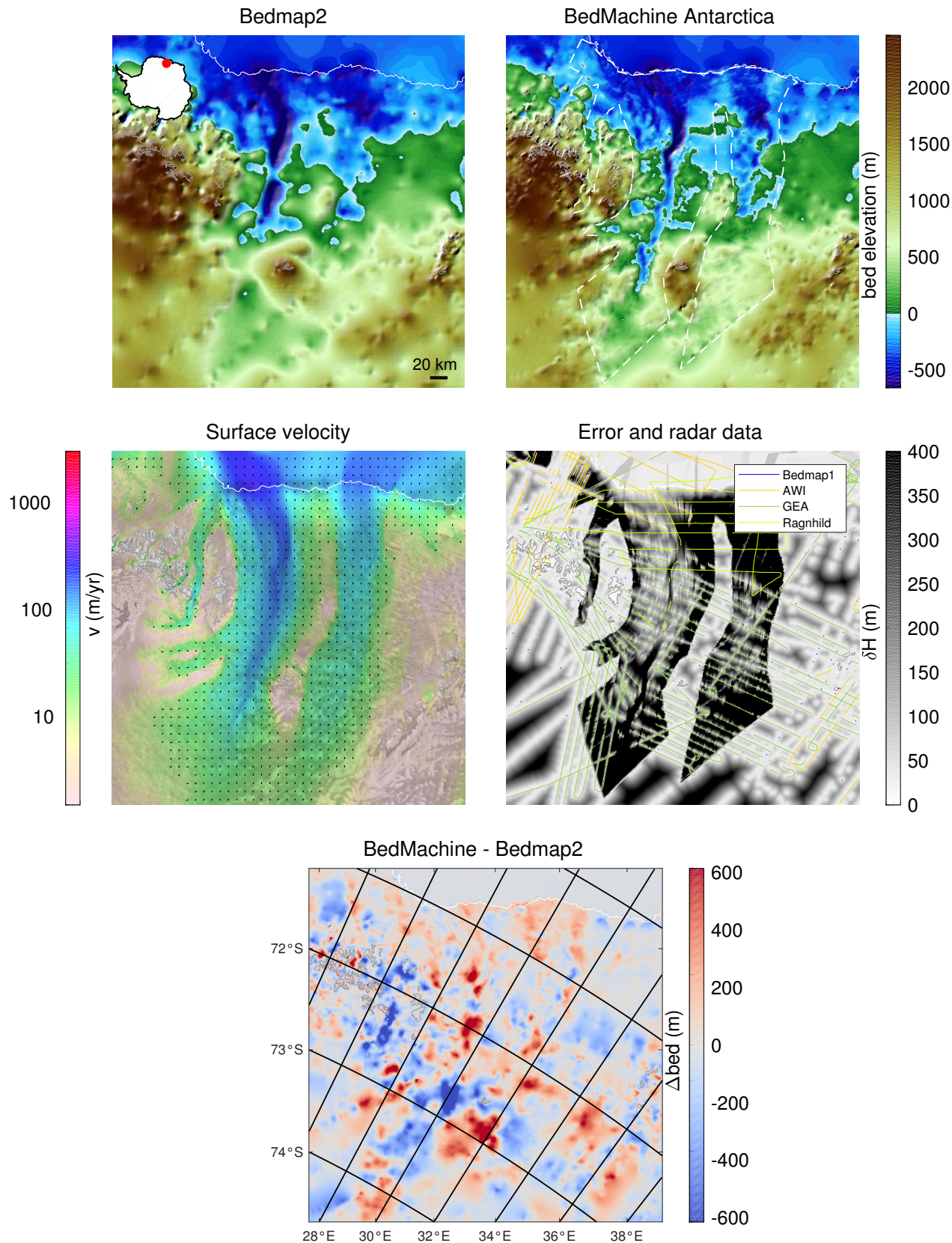


Figure S40: Le Roi Baudouin Ice Shelf

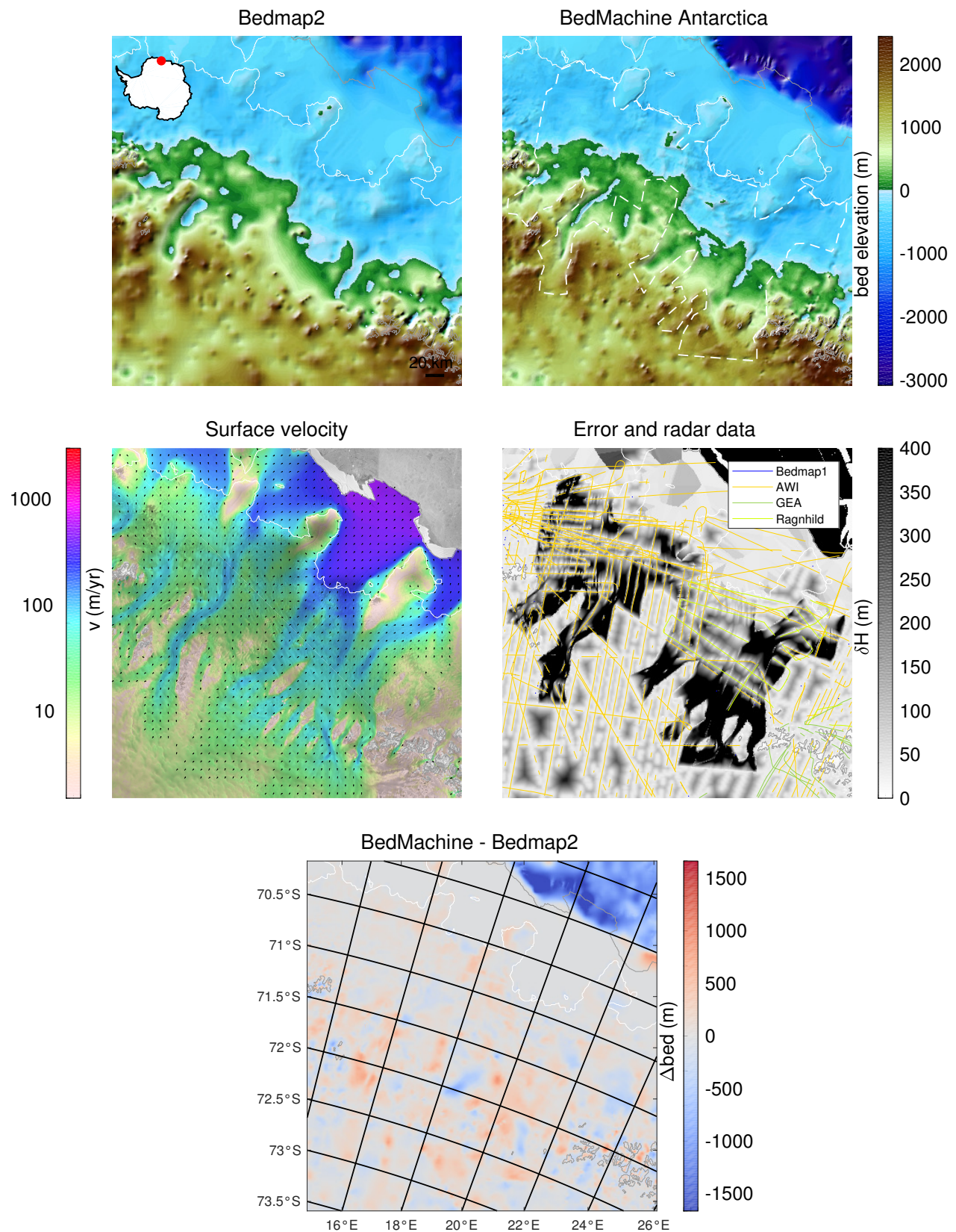


Figure S41: Kolleisen

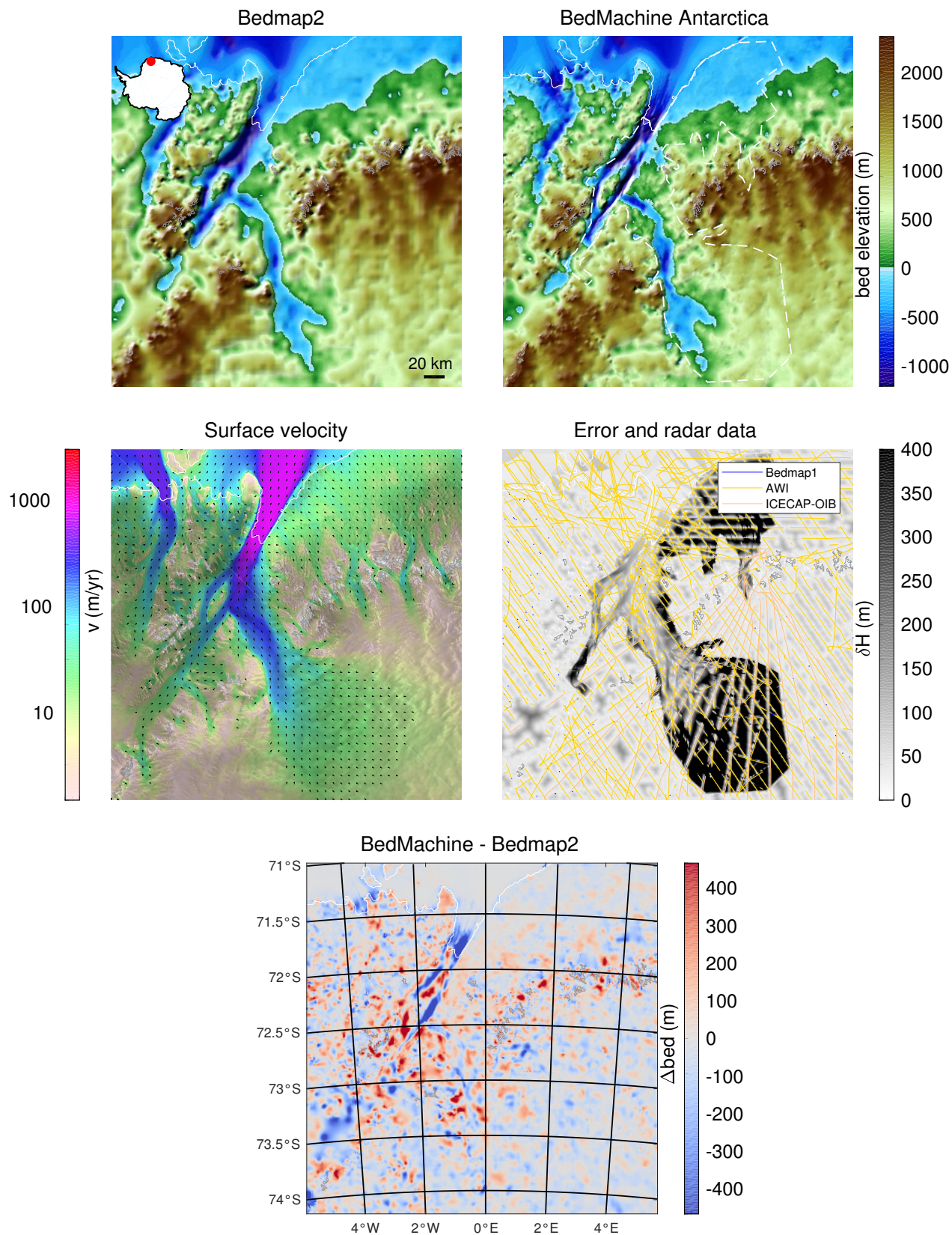


Figure S42: Fimbul Ice Shelf

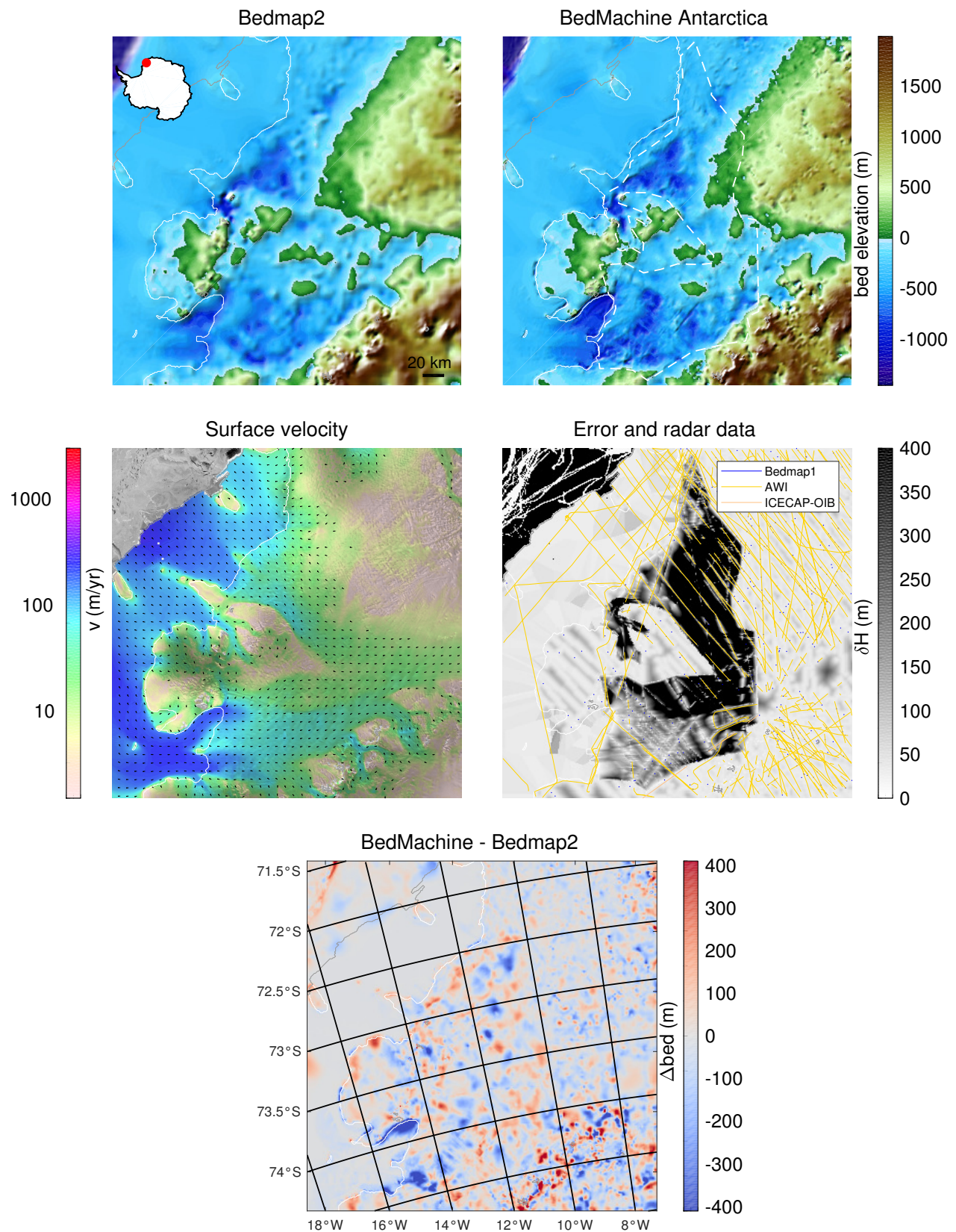


Figure S43: Endurance Glacier

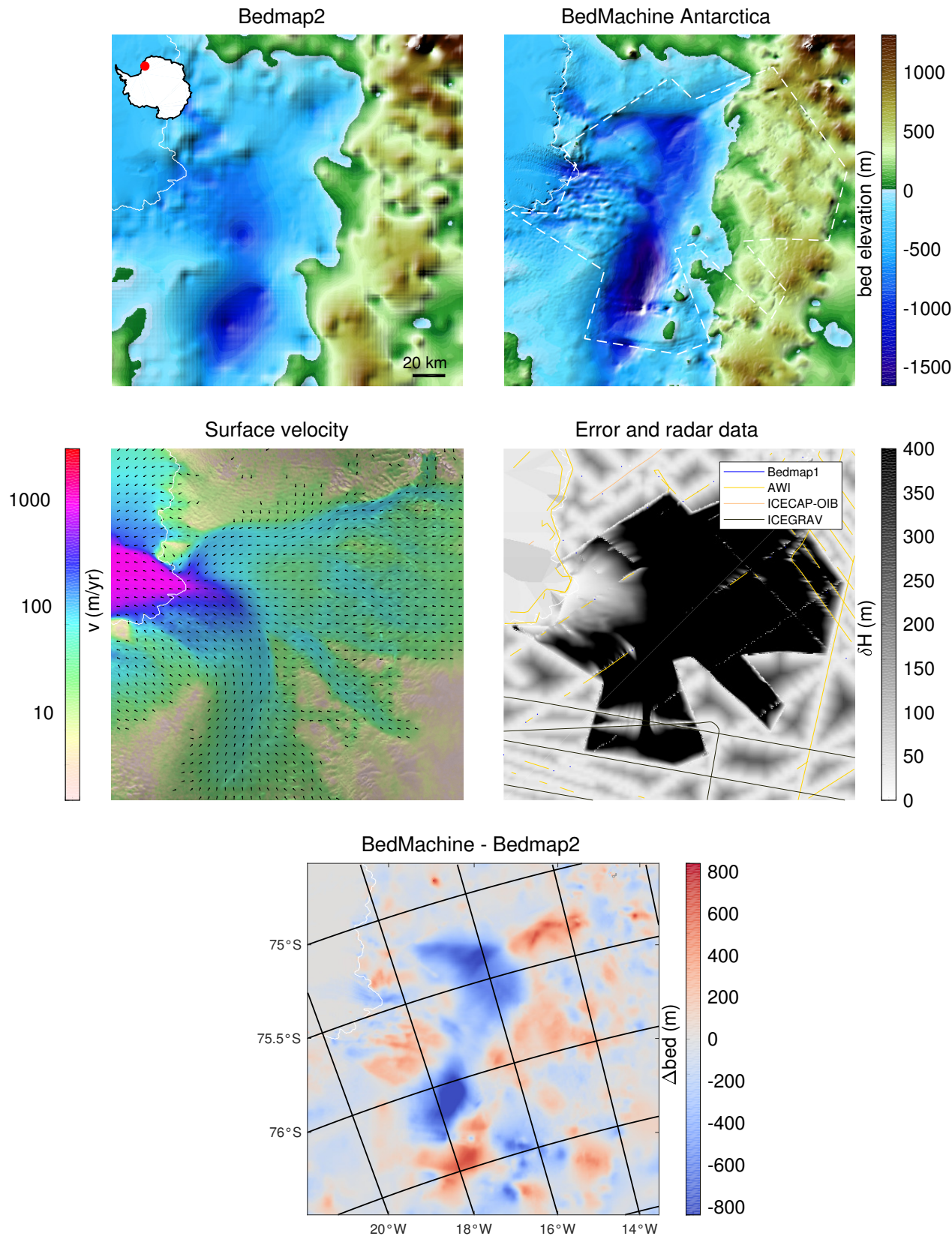


Figure S44: Stancomb-Wills Glacier

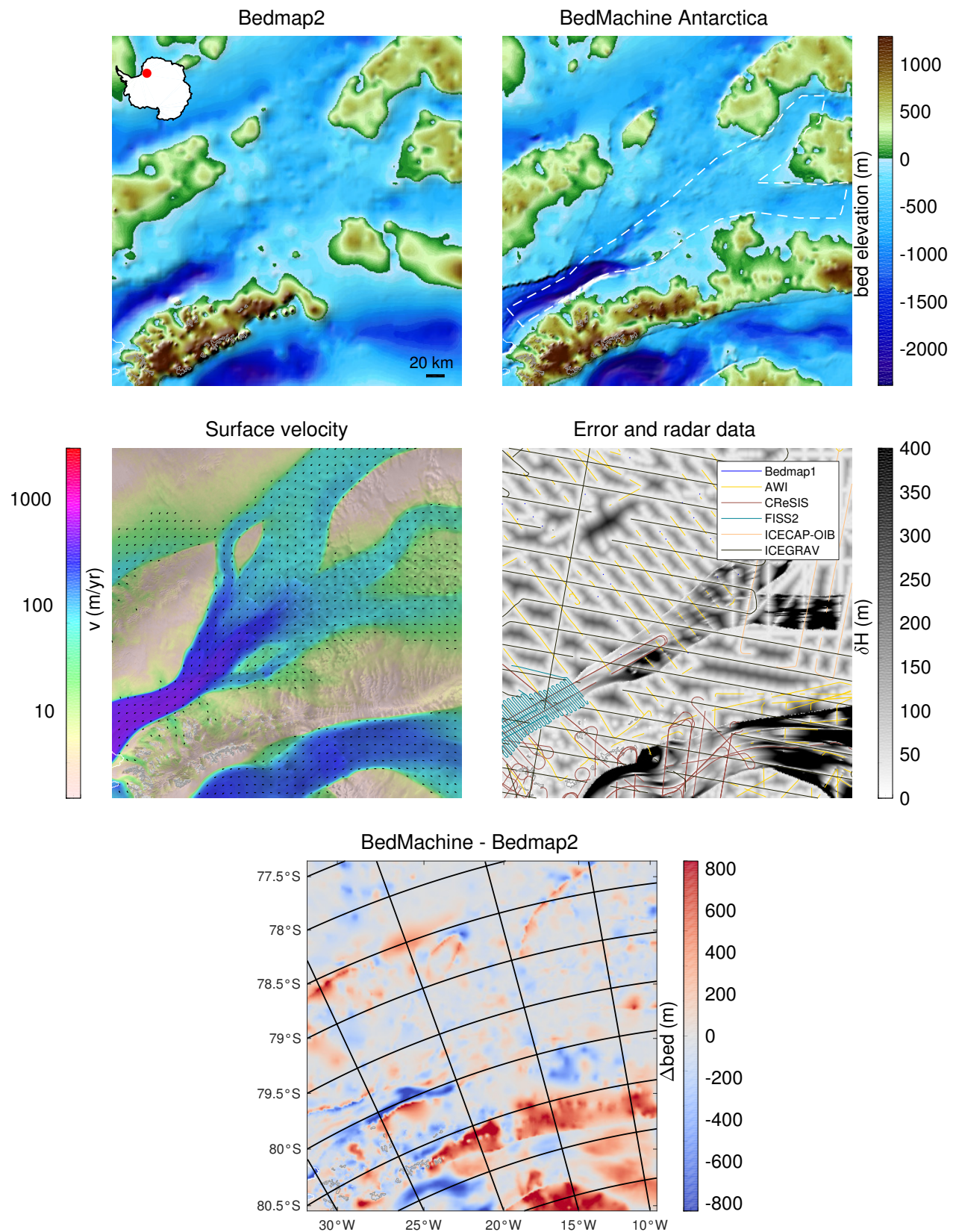


Figure S45: Slessor Ice Stream

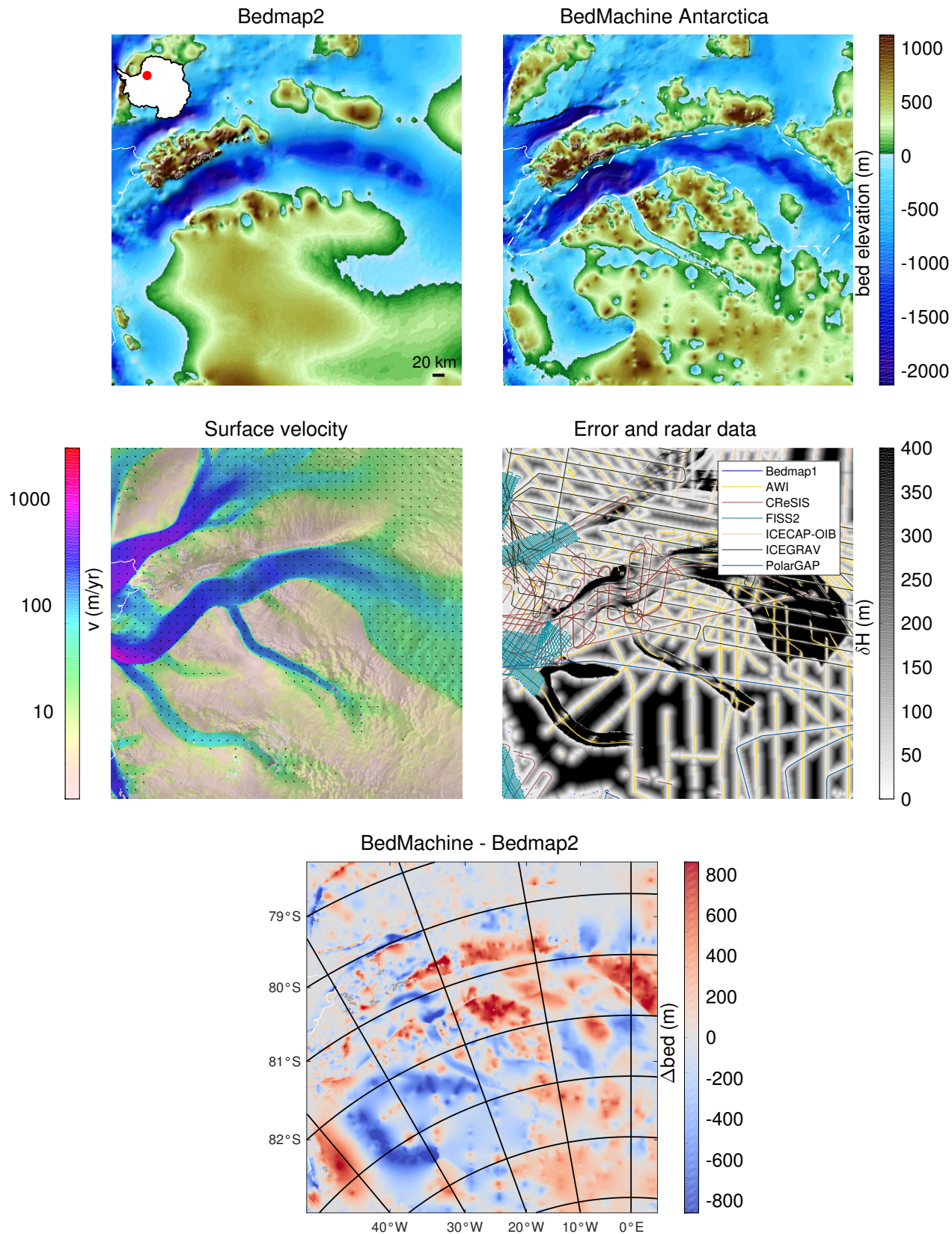


Figure S46: Recovery Ice Stream

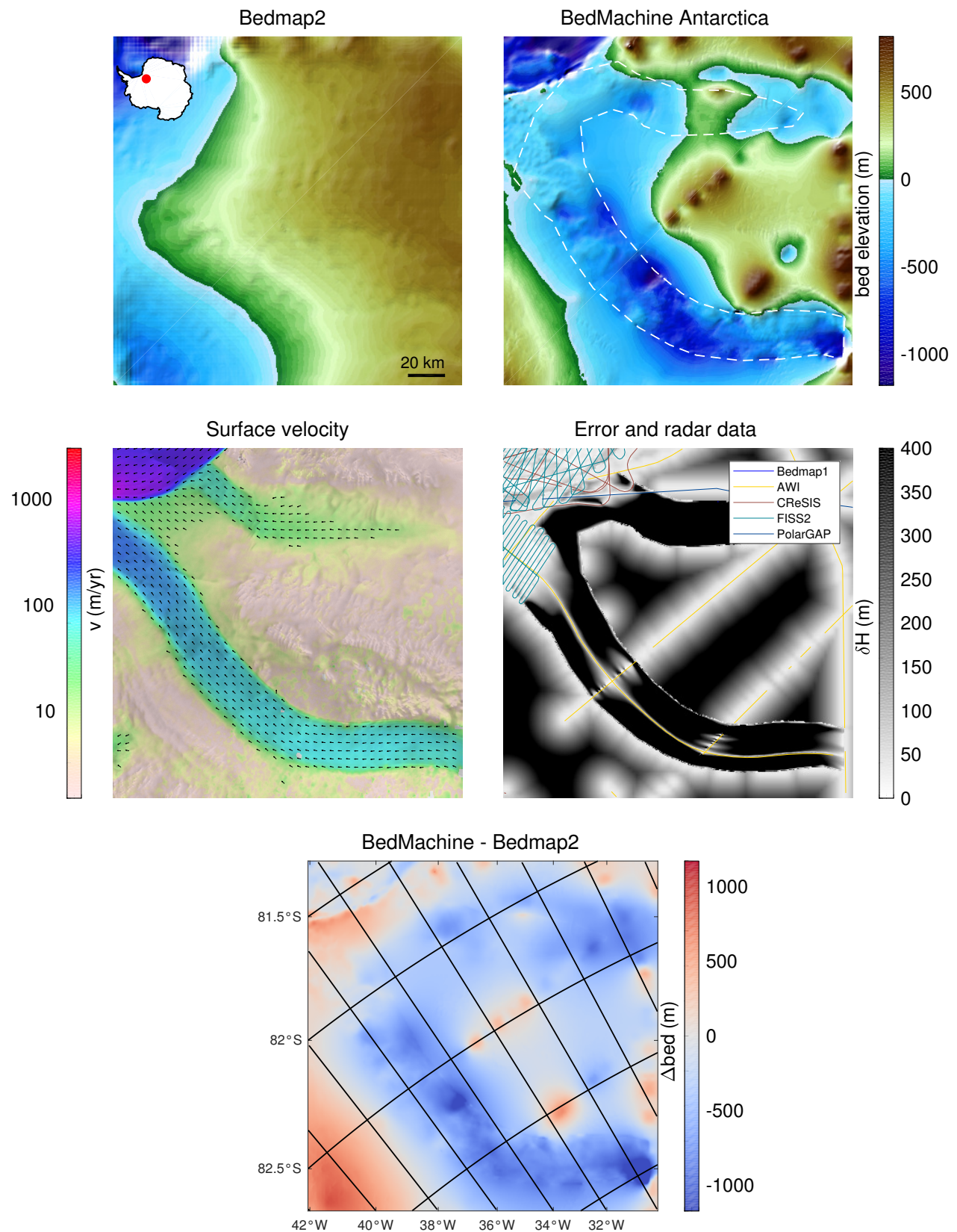


Figure S47: Blackwall Glacier

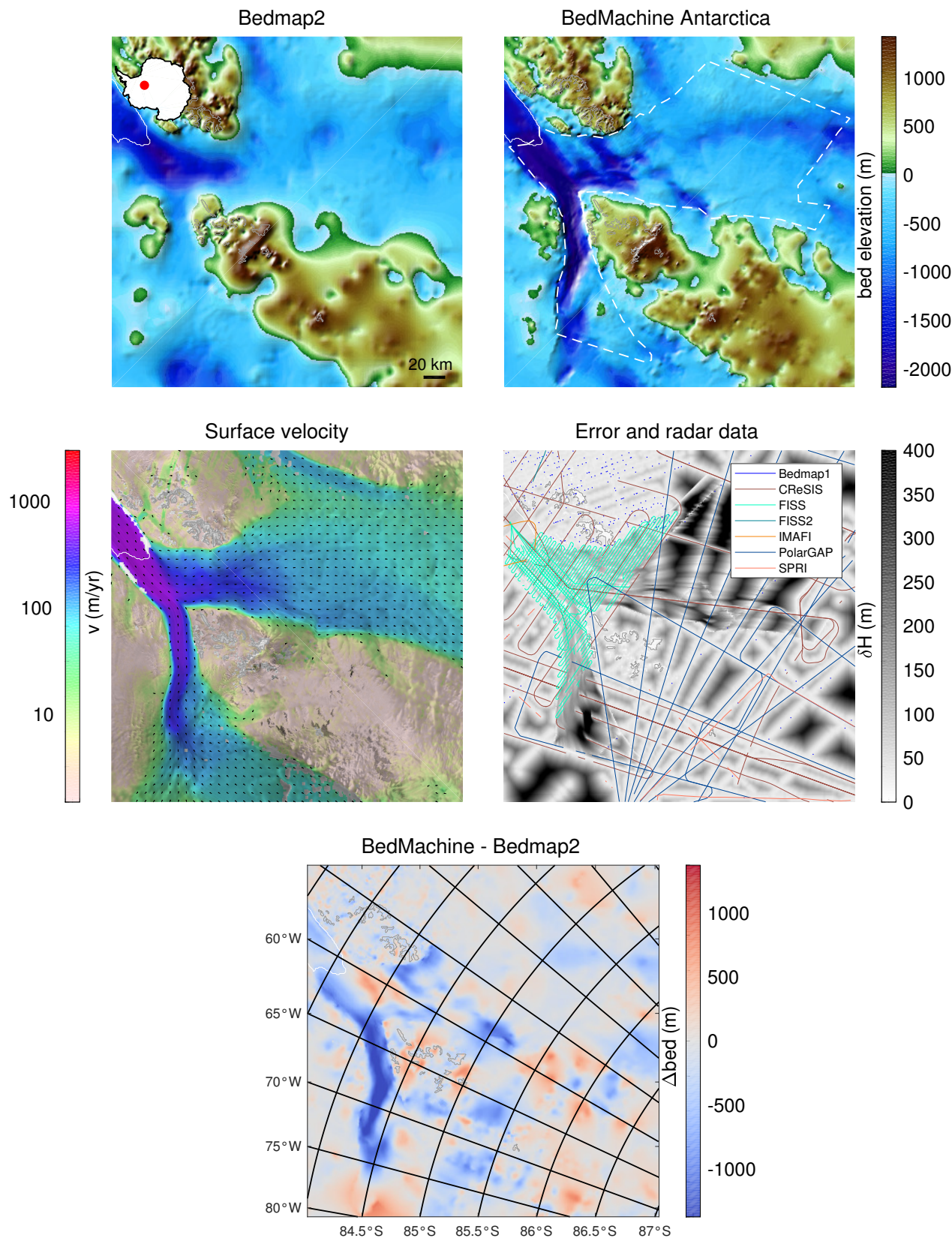


Figure S48: Foundation Ice Stream

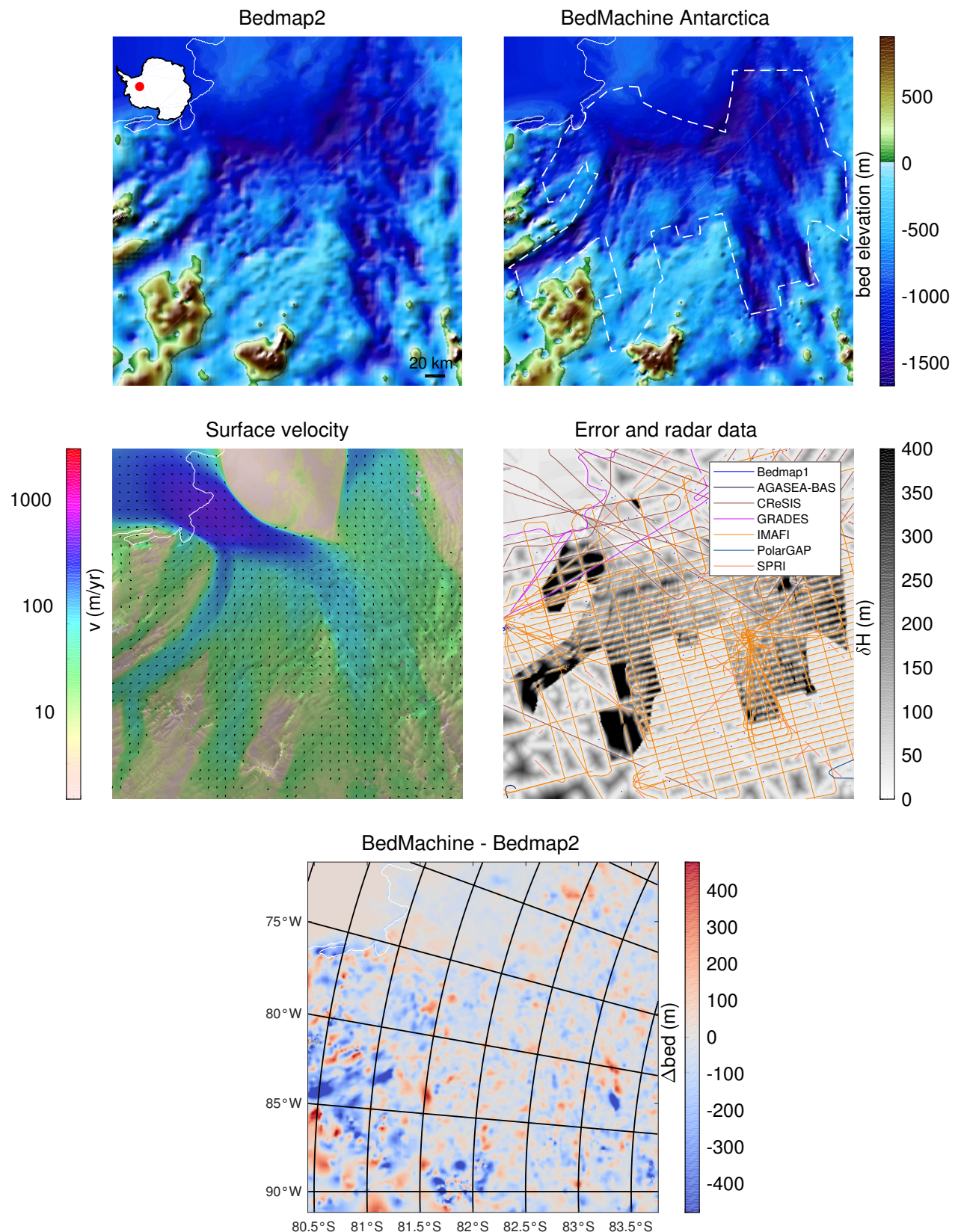


Figure S49: Institute Ice Stream

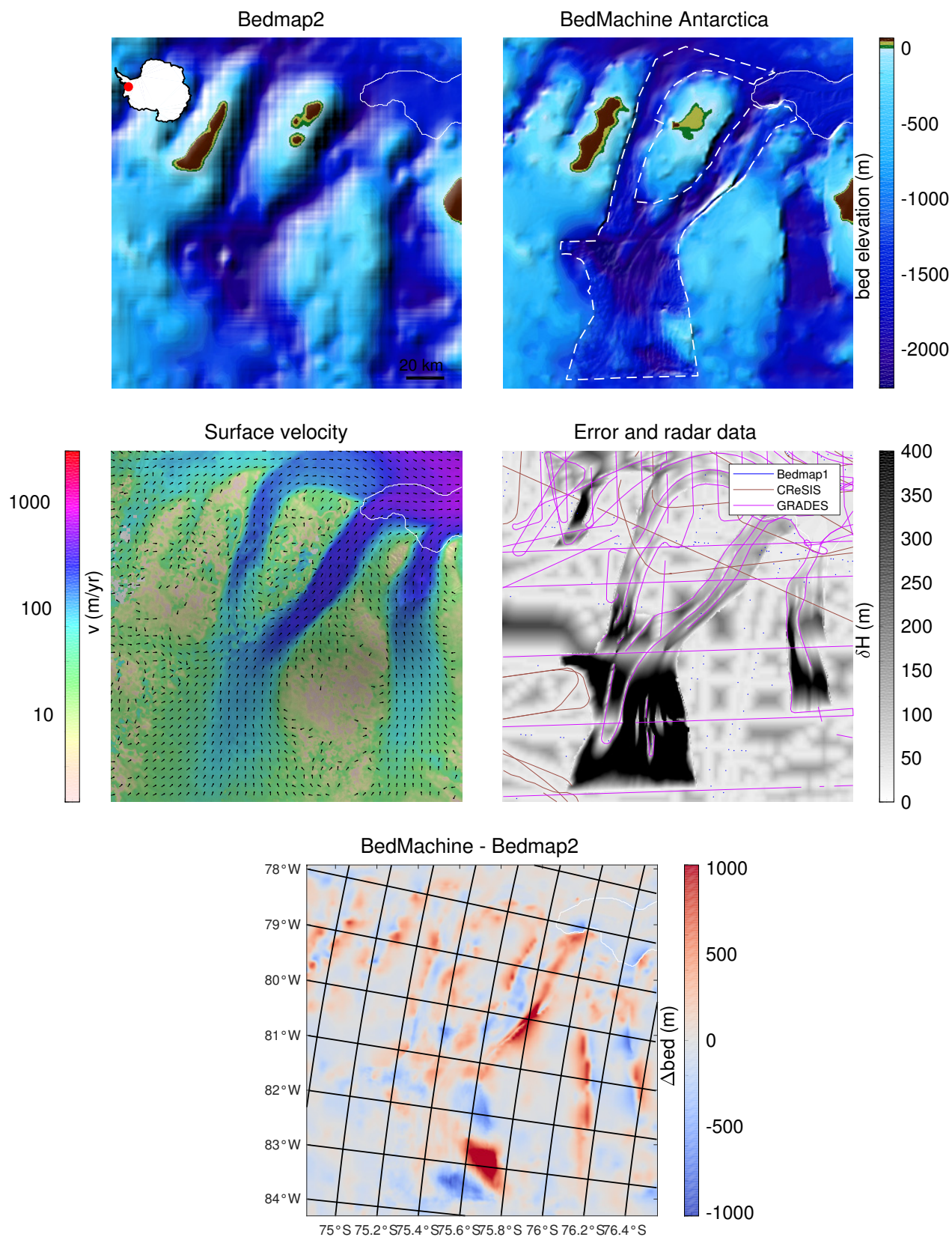


Figure S50: Berg

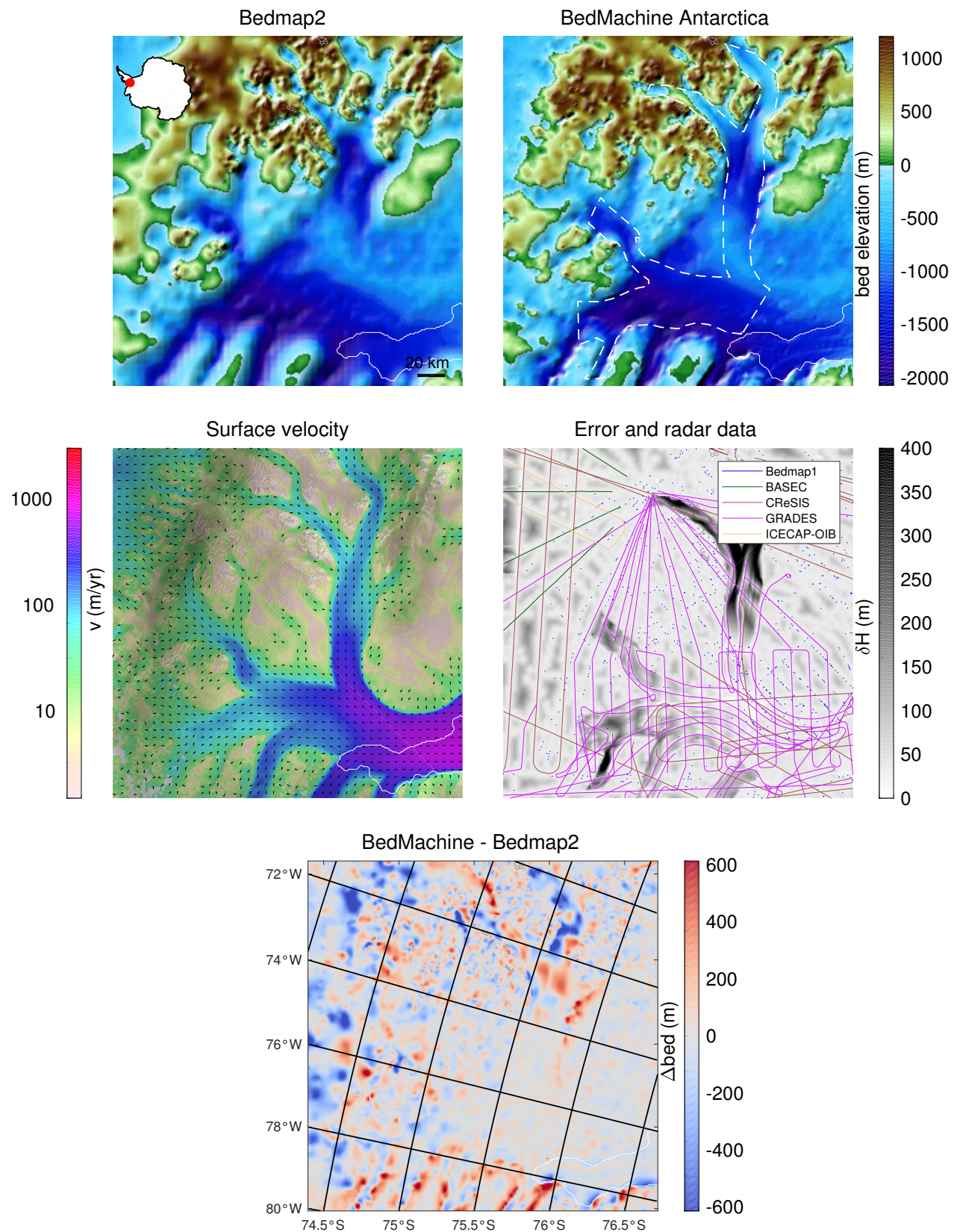


Figure S51: Evans Ice Stream

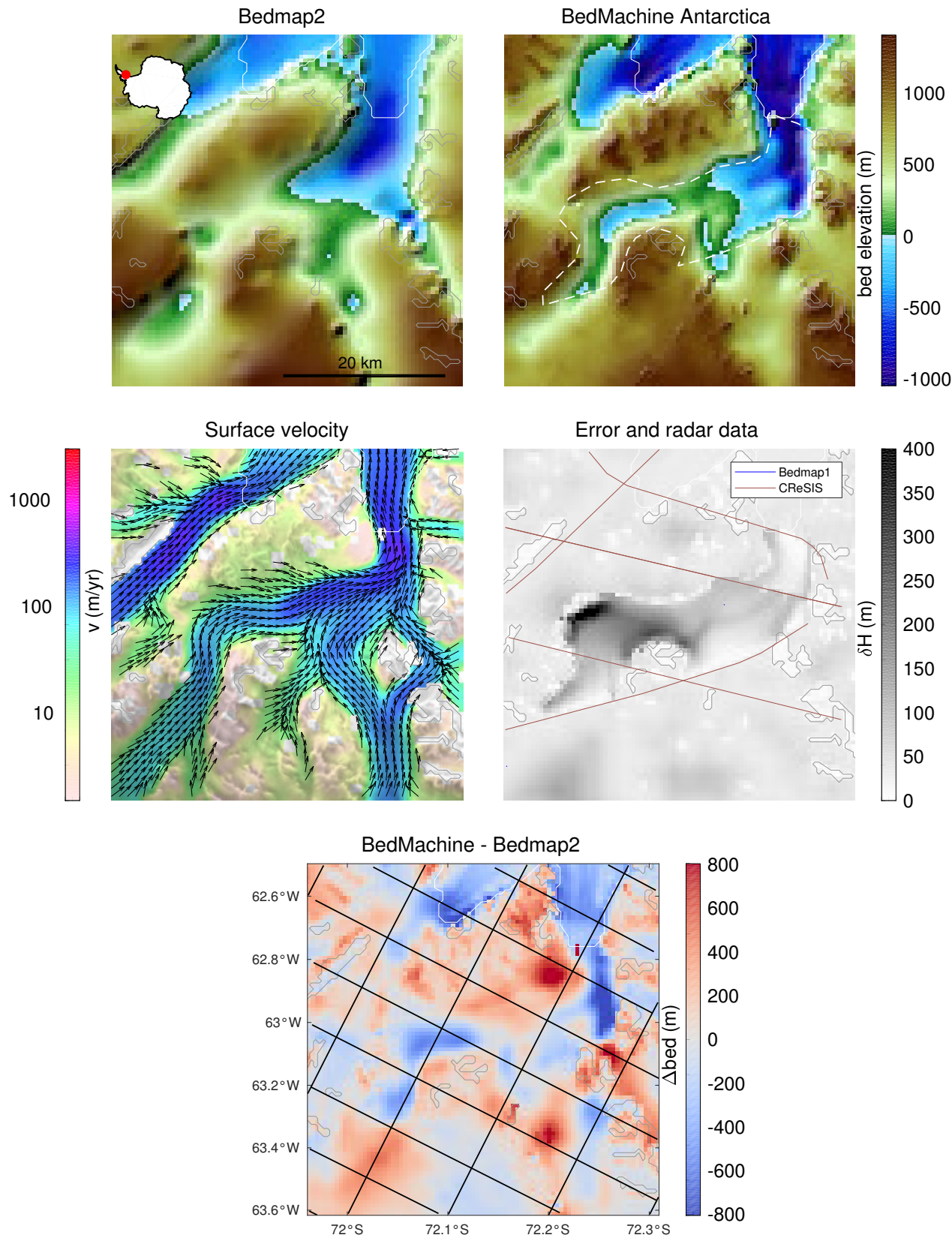


Figure S52: Beaumont Glacier

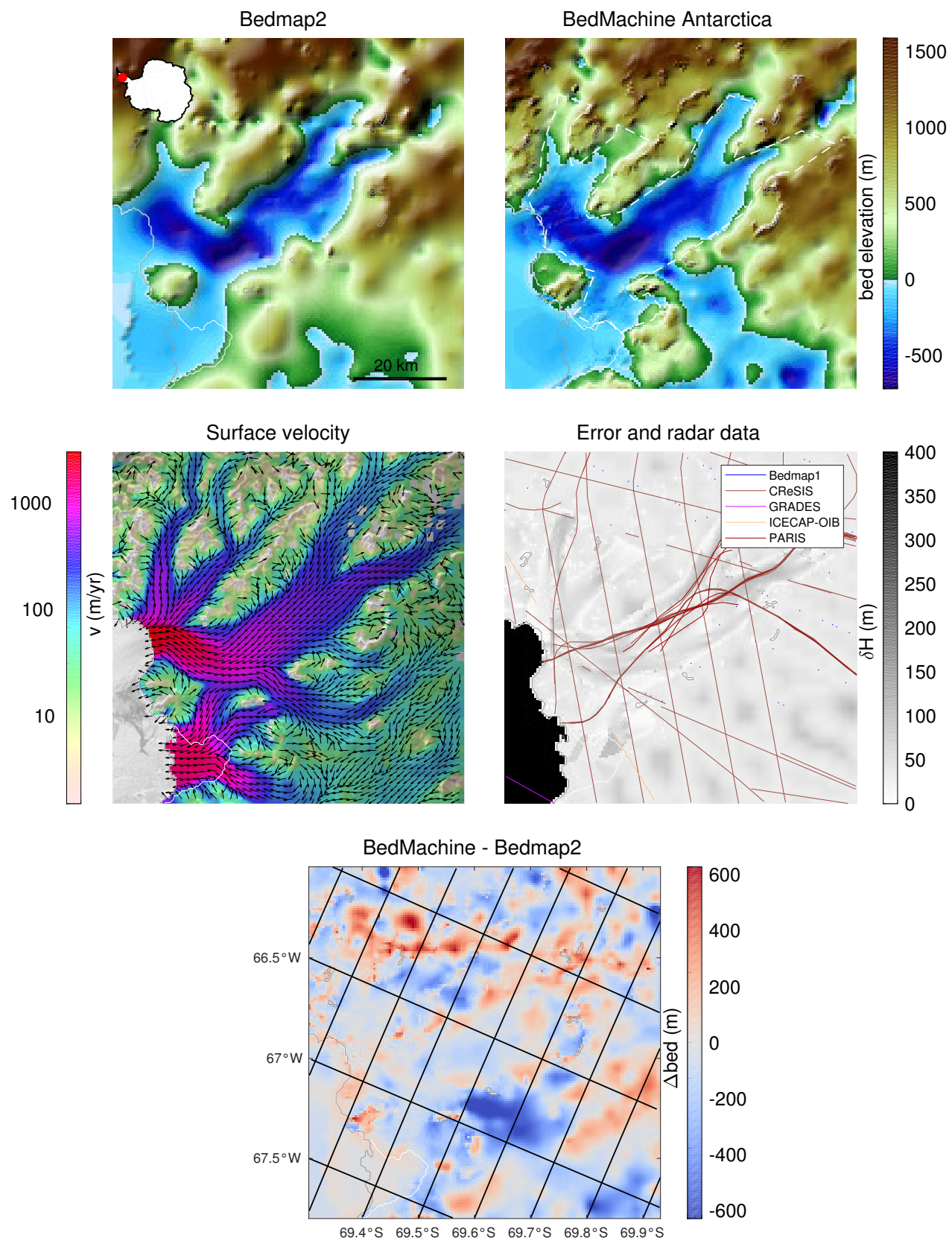


Figure S53: Fleming Glacier

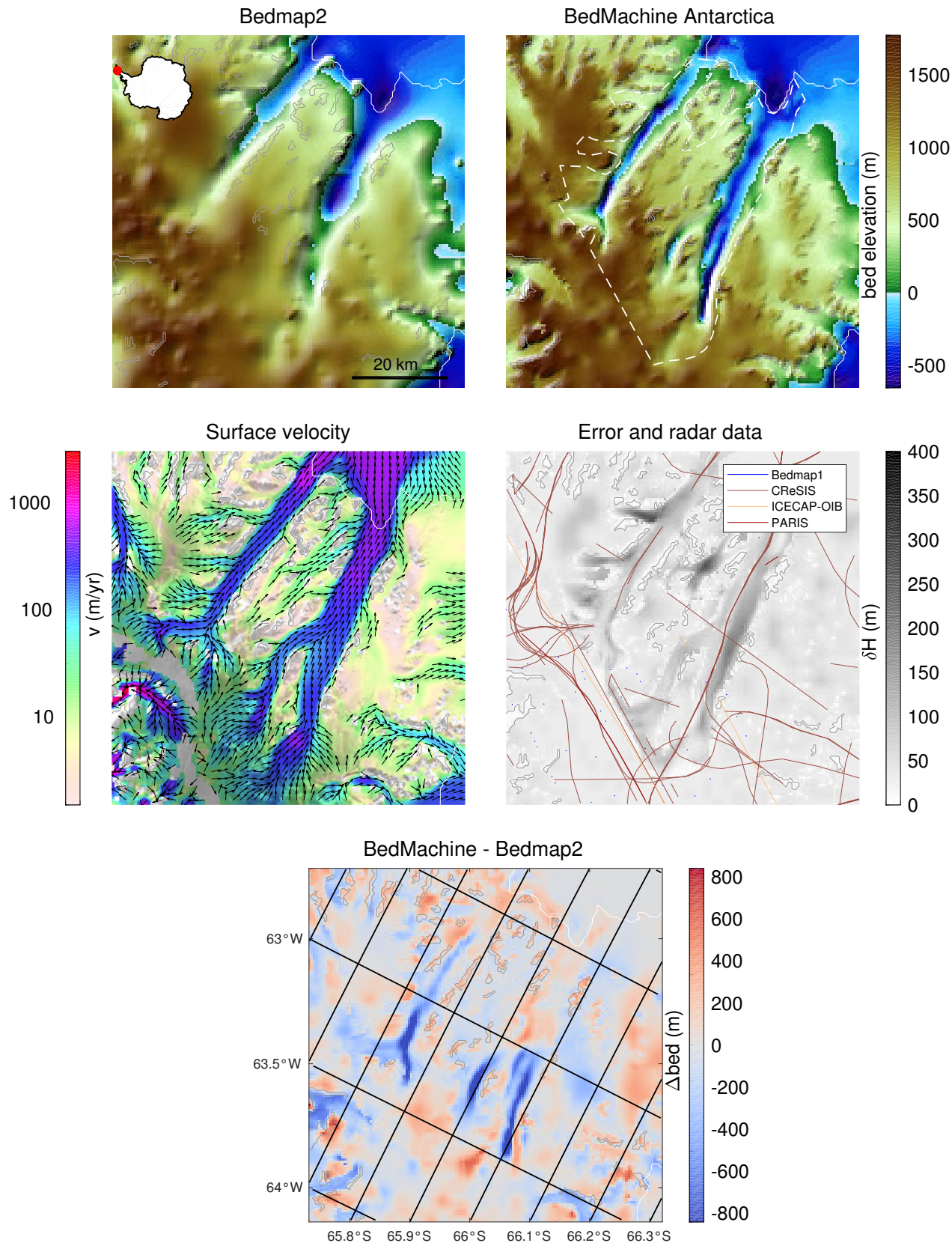


Figure S54: Leppard Glacier

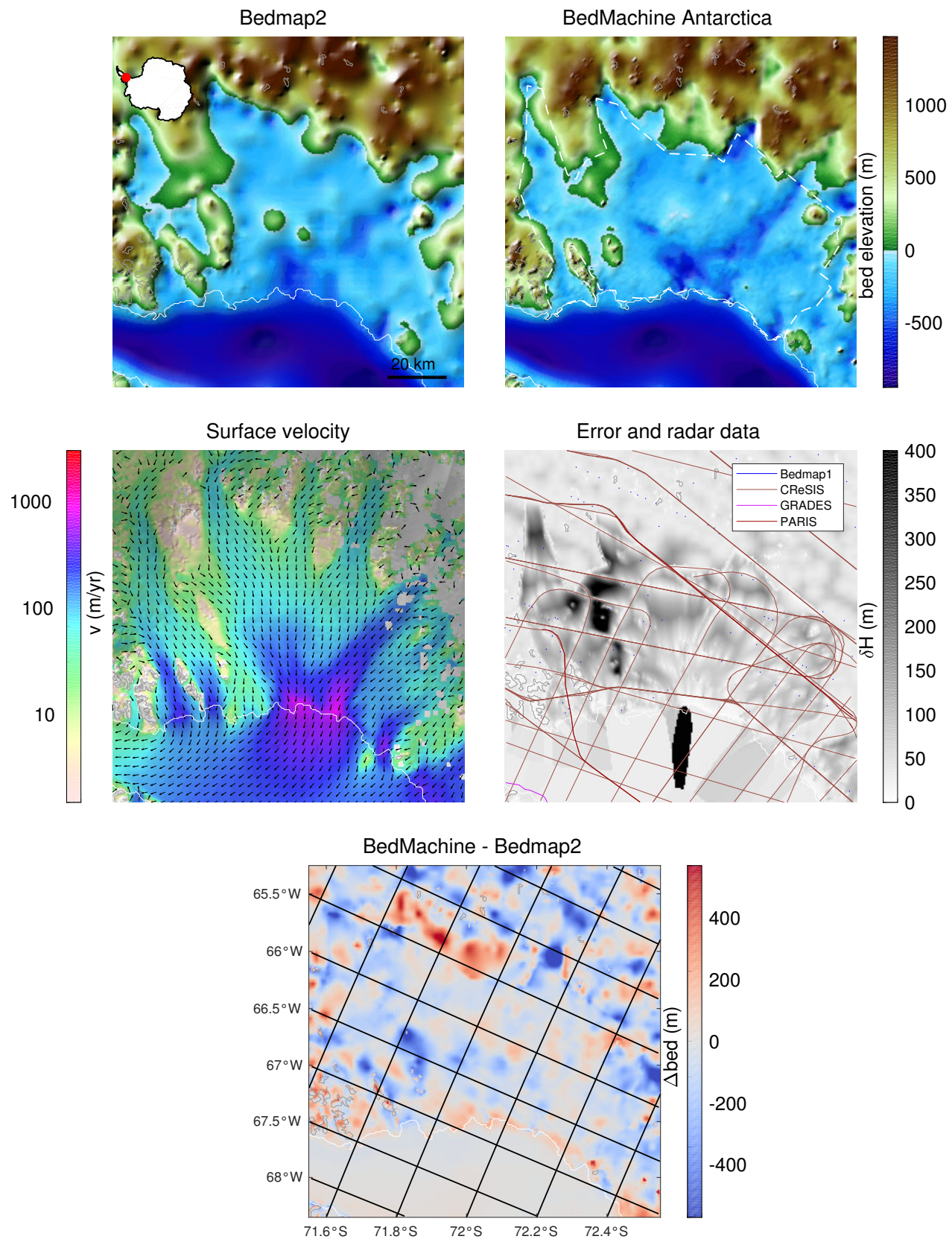


Figure S55: George VI Ice Shelf

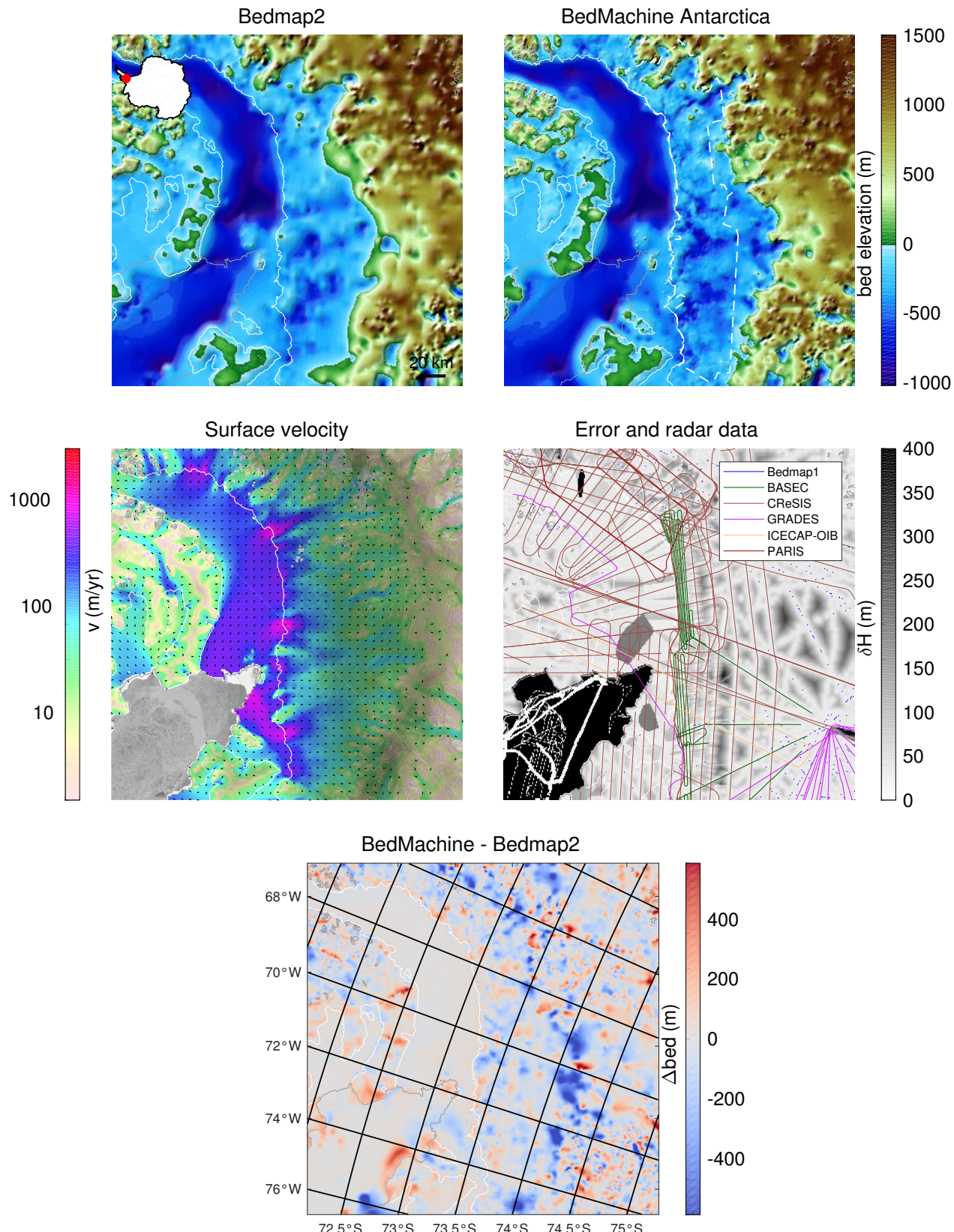


Figure S56: George VI Ice Shelf (2)

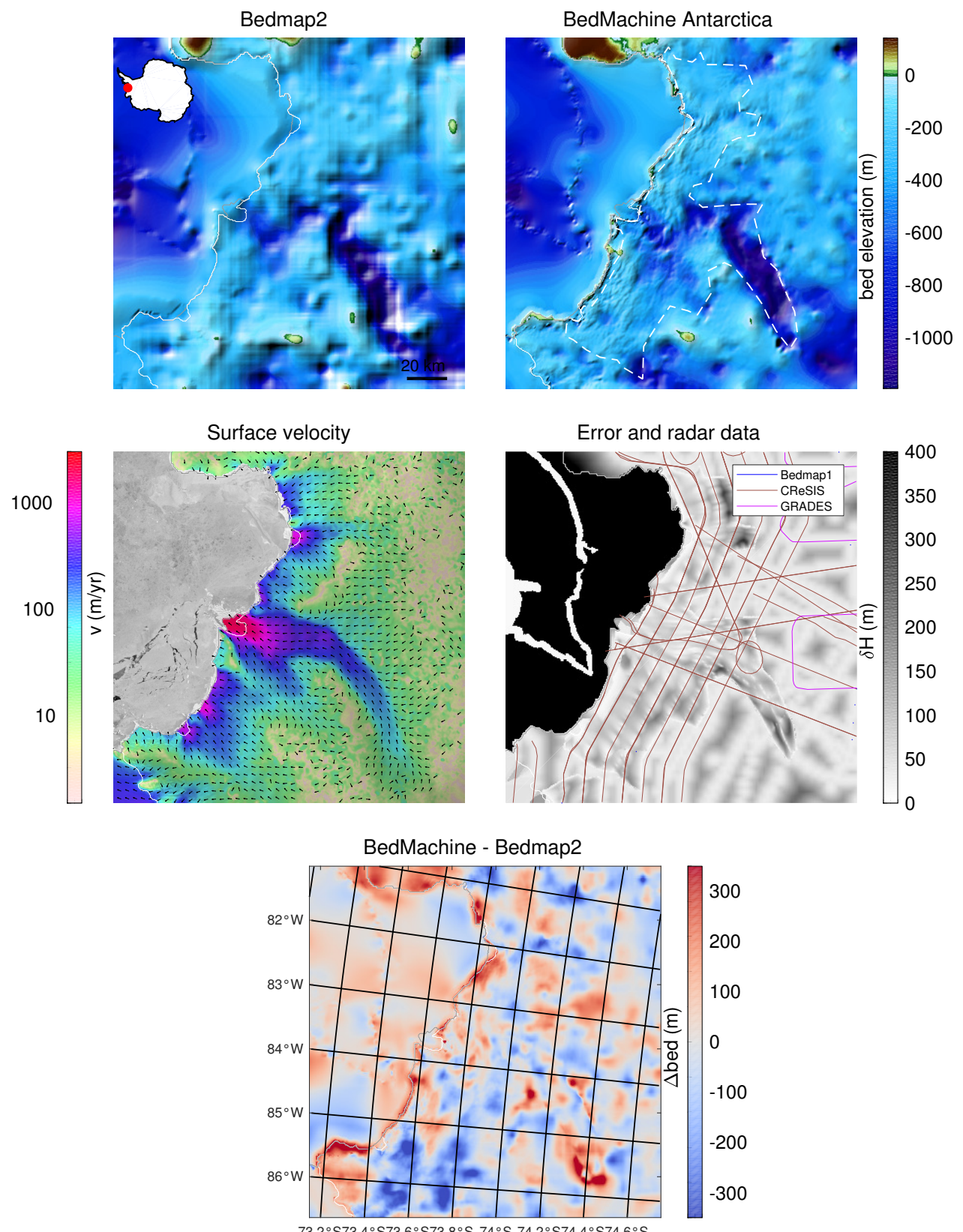


Figure S57: Ferrigno Ice Stream

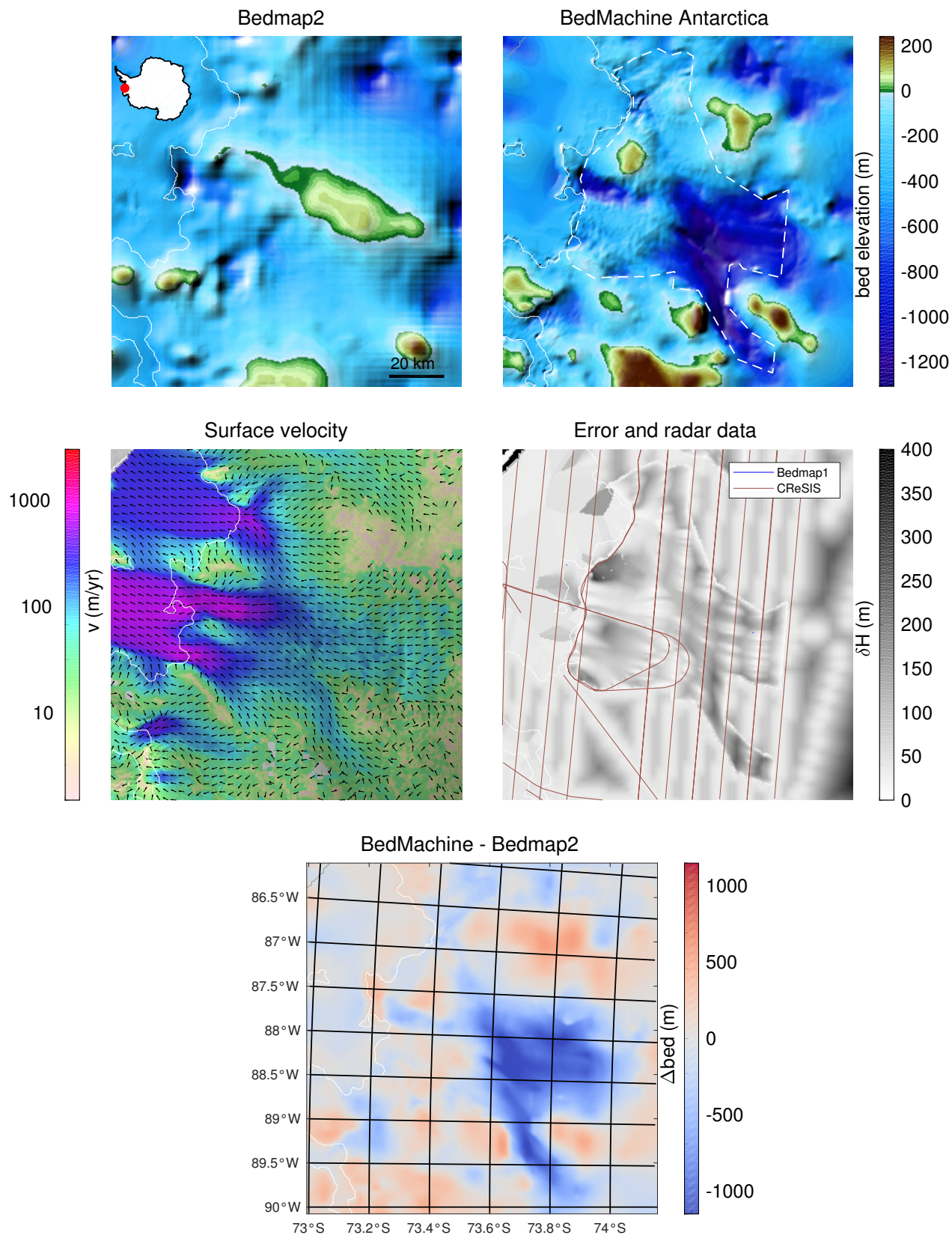


Figure S58: Venable Ice Shelf

5.2 Local slopes and roughness

Figure S59 shows a histogram of the slopes (calculated as $\|\nabla b\|$) for all the regions of BedMachine where the bed is mapped using mass conservation.

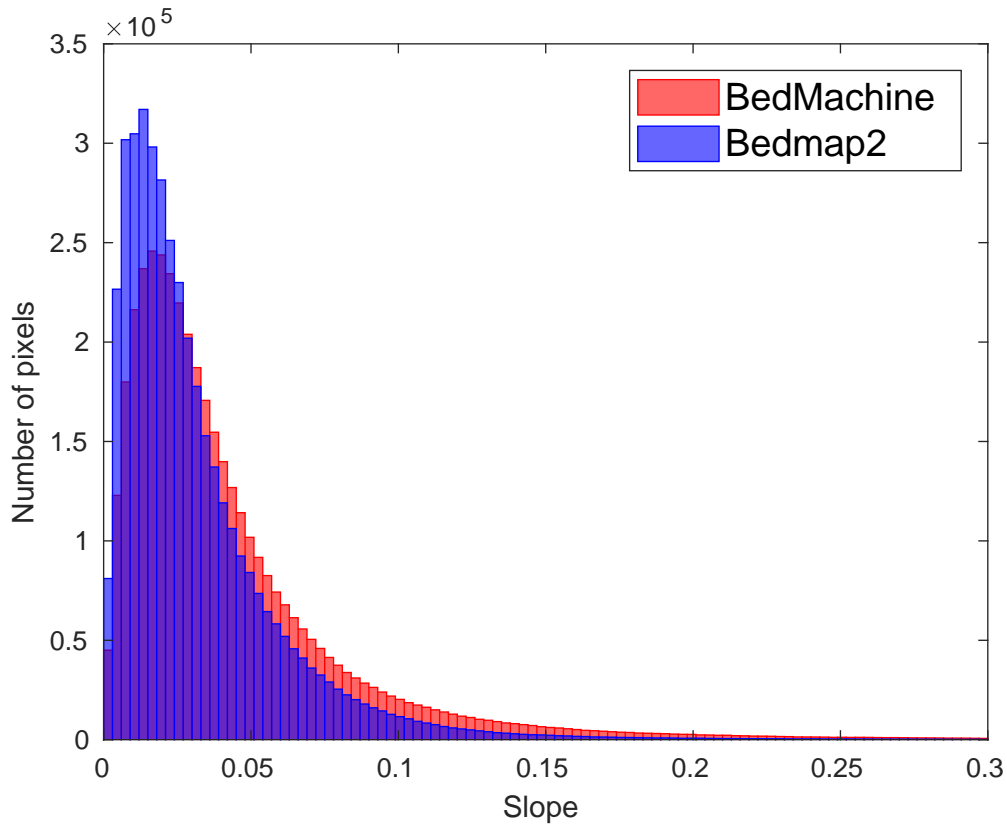


Figure S59: Bed slope histograms for the regions mapped with MC

5.3 Marine Ice Sheet Instability

To locate the regions that may be susceptible to the Marine Ice Sheet Instability (MISI), we use surface velocities from *Rignot et al.* [2011] and look at where

$$\nabla b \cdot \mathbf{v} > 0 \quad \text{and} \quad b < 0. \quad (\text{S20})$$

We compute the slopes at a resolution of 2 km, close to the mean ice thickness. These regions are shown in red in Figure S60.

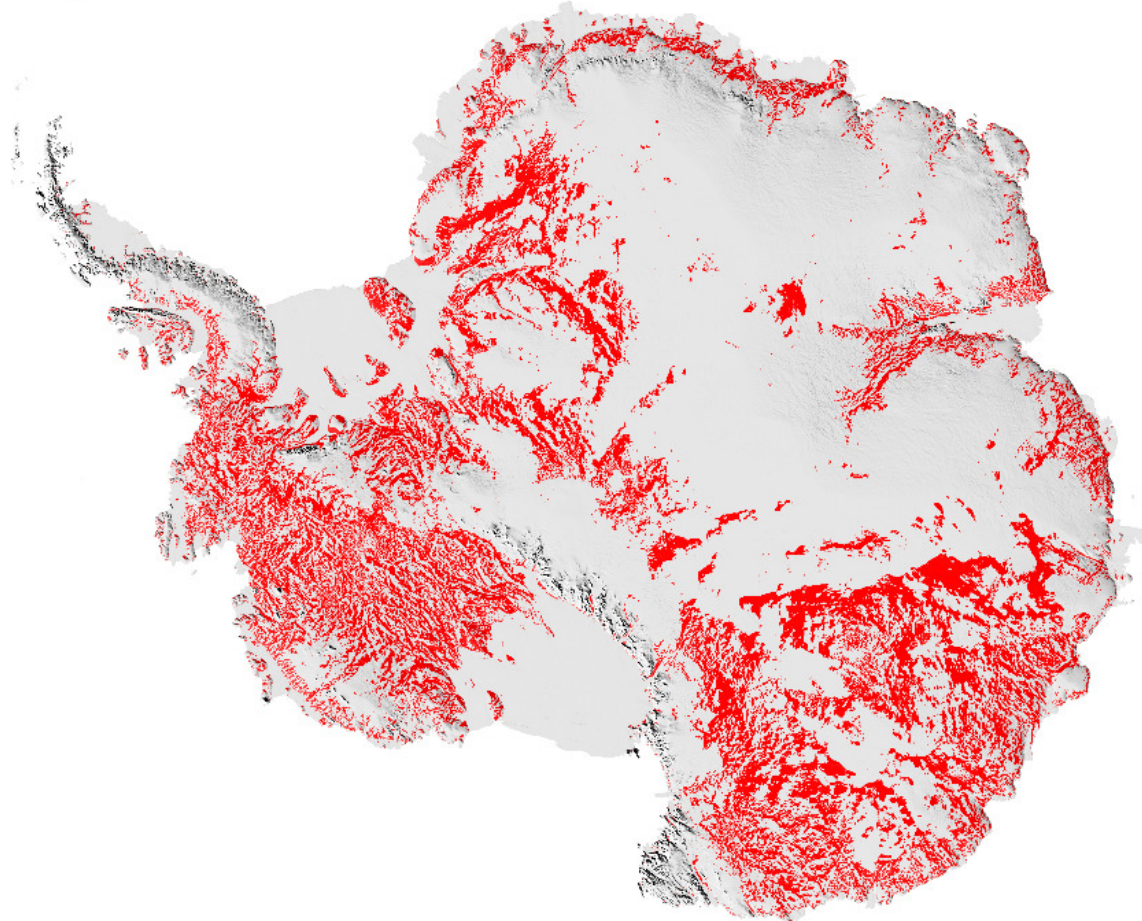


Figure S60: The regions in red are the sectors that may be subject to Marine Ice Sheet Instability according to BedMachine Antarctica.

Bibliography

- Allison, I., and G. Hyland, Amery Ice Shelf compiled and merged ice thickness datasets Australian Antarctic Data Centre - CAASM Metadata, 2010, updated 2017.
- An, L., E. Rignot, R. Millan, K. Tinto, and J. Willis, Bathymetry of Northwest Greenland Using “Ocean Melting Greenland” (OMG) High-Resolution Airborne Gravity and Other Data, *Remote Sens.*, 11(2), doi: 10.3390/rs11020131, 2019.
- Arndt, J. E., et al., The International Bathymetric Chart of the Southern Ocean (IBCSO) Version 1.0:A new bathymetric compilation covering circum-Antarctic waters, *Geophys. Res. Lett.*, 40(12), 3111–3117, doi: 10.1002/grl.50413, 2013.
- Bamber, J. L., R. L. Layberry, and S. Gogineni, A new ice thickness and bed data set for the Greenland Ice Sheet 1. Measurement, data reduction, and errors, *J. Geophys. Res.*, 106(D24), 33,773–33,780, 2001.
- Bamber, J. L., et al., A new bed elevation dataset for Greenland, *Cryosphere*, 7, 499–510, doi:10.5194/tc-7-499-2013, 2013.
- Bell, R. E., et al., Widespread Persistent Thickening of the East Antarctic Ice Sheet by Freezing from the Base, *Science*, 331(6024), 1592–1595, doi:10.1126/science.1200109, 2011.
- Berger, S., L. Favier, R. Drews, J.-J. Derwael, and F. Pattyn, The control of an uncharted pinning point on the flow of an Antarctic ice shelf, *J. Glaciol.*, 62(231), 37–45, doi:10.1017/jog.2016.7, 2016.
- Blankenship, D. D., et al., *Geologic Controls on the Initiation of Rapid Basal Motion for West Antarctic Ice Streams: A Geophysical Perspective Including New Airborne Radar Sounding and Laser Altimetry Results*, pp. 105–121, American Geophysical Union (AGU), doi:10.1029/AR077p0105, 2013a.
- Blankenship, D. D., et al., *Geologic Controls on the Initiation of Rapid Basal Motion for West Antarctic Ice Streams: A Geophysical Perspective Including New Airborne Radar Sounding and Laser Altimetry Results*, pp. 105–121, American Geophysical Union (AGU), doi:10.1029/AR077p0105, 2013b.
- Callens, D., N. Thonnard, J. T. M. Lenaerts, J. M. Van Wessem, W. J. Van de Berg, K. Matsuoka, and F. Pattyn, Mass balance of the Sør Rondane glacial system, East Antarctica, *Ann. Glaciol.*, 56(70), 63–69, doi:10.3189/2015AoG70A010, 2015.
- CReSIS, CReSIS Radar Depth Sounder Data, Lawrence, Kansas, USA. Digital Media, 2016.
- Damm, V., Ice Thickness and Bedrock Map of Matusevich Glacier Drainage System (Oates Coast), *Terra Antarctica*, 11, 85–90, 2004.
- Deutsch, C. L., and A. G. Journel, *GSLIB. Geostatistical Software Library and User's Guide*, 2nd ed., Oxford Univ. Press, New York, 1997.
- Diez, A., K. Matsuoka, F. Ferraccioli, T. A. Jordan, H. F. Corr, J. Kohler, A. V. Olesen, and R. Forsberg, Basal settings control fast ice flow in the Recovery/Slessor/Bailey Region, East Antarctica, *Geophys. Res. Lett.*, 45, doi:10.1002/2017GL076601, 2018.
- Diez, A., K. Matsuoka, T. A. Jordan, J. Kohler, F. Ferraccioli, H. F. Corr, A. V. Olesen, R. Forsberg, and T. G. Casal, Patchy lakes and topographic origin for fast flow in the recovery glacier system, east antarctica, *J. Geophys. Res. - Earth Surface*, doi:10.1029/2018JF004799, 2019.
- Drewry, D. J., D. T. Meldrum, and E. Jankowski, Radio echo and magnetic sounding of the Antarctic ice sheet, 1978–79, *Polar Rec.*, 20(124), 43–51, doi:10.1017/S0032247400002916, 1980.

Drews, R., K. Matsuoka, C. Martín, D. Callens, N. Bergeot, and F. Pattyn, Evolution of Derwael Ice Rise in Dronning Maud Land, Antarctica, over the last millennia, *J. Geophys. Res. - Earth Surface*, 120(3), 564–579, doi:10.1002/2014JF003246, 2015.

Eagles, G., N. B. Karlsson, A. Ruppel, D. Steinhage, W. Jokat, and A. Läufer, Erosion at extended continental margins: Insights from new aerogeophysical data in eastern Dronning Maud Land, *Gondwana Res.*, 63, 105 – 116, doi:<https://doi.org/10.1016/j.gr.2018.05.011>, 2018.

Ferraccioli, F., E. Armadillo, T. Jordan, E. Bozzo, and H. Corr, Aeromagnetic exploration over the East Antarctic Ice Sheet: A new view of the Wilkes Subglacial Basin, *Tectonophysics*, 478(1), 62 – 77, doi: <https://doi.org/10.1016/j.tecto.2009.03.013>, magnetic Anomalies, 2009.

Ferraccioli, F., C. A. Finn, T. A. Jordan, R. E. Bell, L. M. Anderson, and D. Damaske, East Antarctic rifting triggers uplift of the Gamburtsev Mountains, *Nature*, 479, 2011.

Forsberg, R., A. V. Olesen, F. Ferraccioli, T. A. Jordan, K. Matsuoka, A. Zakrajsek, M. Ghidella, and J. S. Greenbaum, Exploring the Recovery Lakes region and interior Dronning Maud Land, East Antarctica, with airborne gravity, magnetic and radar measurements, *Geological Society, London, Special Publications*, 461(1), 23–34, doi:10.1144/SP461.17, 2018.

Fretwell, P., et al., Bedmap2: improved ice bed, surface and thickness datasets for Antarctica, *Cryosphere*, 7(1), 375–393, doi:10.5194/tc-7-375-2013, 2013.

Goel, V., J. Brown, and K. Matsuoka, Glaciological settings and recent mass balance of Blåskimen Island in Dronning Maud Land, Antarctica, *Cryosphere*, 11(6), 2883–2896, doi:10.5194/tc-11-2883-2017, 2017.

Greenbaum, J. S., et al., Ocean access to a cavity beneath Totten Glacier in East Antarctica, *Nat. Geosci.*, 8, 294–298, doi:10.1038/NGEO2388, 2015.

Griggs, J. A., and J. L. Bamber, Ice shelf thickness over Larsen C, Antarctica, derived from satellite altimetry, *Geophys. Res. Lett.*, 36, 1–5, doi:10.1029/2009gl039527, 2009.

Hansen, P. C., The L-Curve and its Use in the Numerical Treatment of Inverse Problems, in *Computational Inverse Problems in Electrocardiology*, ed. P. Johnston, *Advances in Computational Bioengineering*, pp. 119–142, WIT Press, Southampton, 2000.

Holt, J. W., D. D. Blankenship, D. L. Morse, D. A. Young, M. E. Peters, S. D. Kempf, T. G. Richter, D. G. Vaughan, and H. F. J. Corr, New boundary conditions for the West Antarctic Ice Sheet: Subglacial topography of the Thwaites and Smith glacier catchments, *Geophys. Res. Lett.*, 33(9), 1–4, doi: 10.1029/2005GL025561, 2006a.

Holt, J. W., T. G. Richter, S. D. Kempf, D. L. Morse, and D. D. Blankenship, Airborne gravity over lake vostok and adjacent highlands of east antarctica, *Geochem. Geophys. Geosyst.*, 7(11), doi:10.1029/2005GC001177, 2006b.

Howat, I., P. Morin, C. Porter, and M.-J. Noh, The Reference Elevation Model of Antarctica, *Tech. rep.*, Harvard Dataverse, V1, accessed Sept. 2018, doi:<https://doi.org/10.7910/DVN/SAIK8B>, 2018.

Howat, I. M., C. Porter, B. E. Smith, M.-J. Noh, and P. Morin, The Reference Elevation Model of Antarctica, *Cryosphere*, 13(2), 665–674, doi:10.5194/tc-13-665-2019, 2019.

Humbert, A., D. Steinhage, V. Helm, S. Beyer, and T. Kleiner, Missing Evidence of Widespread Subglacial Lakes at Recovery Glacier, Antarctica, *J. Geophys. Res.*, 123(11), 2802–2826, doi:10.1029/2017JF004591, 2018.

- Jordan, T. A., F. Ferraccioli, H. Corr, A. Graham, E. Armadillo, and E. Bozzo, Hypothesis for mega-outburst flooding from a palaeo-subglacial lake beneath the East Antarctic Ice Sheet, *Terra Nova*, 22(4), 283–289, 2010.
- Jordan, T. A., C. Martin, F. Ferraccioli, K. Matsuoka, H. Corr, R. Forsberg, A. Olesen, and M. Siegert, Anomalous high geothermal flux near the South Pole, *Sci. Rep.*, 8(1), 16,785, doi:10.1038/s41598-018-35182-0, 2018.
- Karlsson, N. B., T. Binder, G. Eagles, V. Helm, F. Pattyn, B. Van Liefferinge, and O. Eisen, Glaciological characteristics in the Dome Fuji region and new assessment for “Oldest Ice”, *Cryosphere*, 12(7), 2413–2424, doi:10.5194/tc-12-2413-2018, 2018.
- King, E. C., H. D. Pritchard, and A. M. Smith, Subglacial landforms beneath Rutford Ice Stream, Antarctica: detailed bed topography from ice-penetrating radar, *Earth Syst. Sci. Data*, 8(1), 151–158, doi:10.5194/essd-8-151-2016, 2016.
- Kristoffersen, Y., C. Hofstede, A. Diez, R. Blenkner, A. Lambrecht, C. Mayer, and O. Eisen, Reassembling gondwana: A new high quality constraint from vibroseis exploration of the sub-ice shelf geology of the East Antarctic continental margin, *J. Geophys. Res.*, 119(12), 9171–9182, doi:10.1002/2014JB011479, 2014.
- Langley, K., J. Kohler, K. Matsuoka, A. Sinisalo, T. Scambos, T. Neumann, A. Muto, J.-G. Winther, and M. Albert, Recovery Lakes, East Antarctica: Radar assessment of sub-glacial water extent, *Geophys. Res. Lett.*, 38, 1–5, doi:10.1029/2010GL046094, 2011.
- Larour, E., H. Seroussi, M. Morlighem, and E. Rignot, Continental scale, high order, high spatial resolution, ice sheet modeling using the Ice Sheet System Model (ISSM), *J. Geophys. Res.*, 117(F01022), 1–20, doi:10.1029/2011JF002140, 2012.
- Le Brocq, A. M., A. J. Payne, and A. Vieli, An improved Antarctic dataset for high resolution numerical ice sheet models (ALBMAP v1), *Earth System Science Data*, 2(2), 247–260, doi:10.5194/essd-2-247-2010, 2010.
- Ligtenberg, S. R. M., M. M. Helsen, and M. R. van den Broeke, An improved semi-empirical model for the densification of Antarctic firn, *Cryosphere*, 5, 809–819, doi:10.5194/tc-5-809-2011, 2011.
- Lough, A. C., et al., Seismic detection of an active subglacial magmatic complex in Marie Byrd Land, Antarctica, *Nat. Geosci.*, 6(12), 1031–1035, doi:10.1038/ngeo1992, 2013.
- Luyendyk, B. P., D. S. Wilson, and C. S. Siddoway, Eastern margin of the Ross Sea Rift in western Marie Byrd Land, Antarctica: Crustal structure and tectonic development, *Geochemistry, Geophysics, Geosystems*, 4(10), doi:10.1029/2002GC000462, 2003.
- Lythe, M. B., and D. G. Vaughan, BEDMAP: Anew ice thickness and subglacial topographic model of Antarctica., *J. Geophys. Res.*, 106 (B6), 11,335–11,351, 2001.
- Millan, R., E. Rignot, V. Bernier, M. Morlighem, and P. Dutrieux, Bathymetry of the Amundsen Sea Embayment sector of West Antarctica from Operation IceBridge gravity and other data, *Geophys. Res. Lett.*, 44(3), 1360–1368, doi:10.1002/2016GL072071, 2017.
- Morlighem, M., E. Rignot, H. Seroussi, E. Larour, H. Ben Dhia, and D. Aubry, A mass conservation approach for mapping glacier ice thickness, *Geophys. Res. Lett.*, 38(L19503), 1–6, doi:10.1029/2011GL048659, 2011.
- Morlighem, M., E. Rignot, J. Mouginot, H. Seroussi, and E. Larour, High-resolution ice thickness mapping in South Greenland, *Ann. Glaciol.*, 55(67), 64–70, doi:10.3189/2014AoG67A088, 2014a.

- Morlighem, M., E. Rignot, J. Mouginot, H. Seroussi, and E. Larour, Deeply incised submarine glacial valleys beneath the Greenland Ice Sheet, *Nat. Geosci.*, 7(6), 418–422, doi:10.1038/ngeo2167, 2014b.
- Morlighem, M., et al., BedMachine v3: Complete bed topography and ocean bathymetry mapping of Greenland from multi-beam echo sounding combined with mass conservation, *Geophys. Res. Lett.*, 44(21), 11,051–11,061, doi:10.1002/2017GL074954, 2017GL074954, 2017.
- Mouginot, J., E. Rignot, Y. Gim, D. Kirchner, and E. Le Meur, Low-frequency radar sounding of ice in East Antarctica and southern Greenland, *Ann. Glaciol.*, 55(67), 138–146, doi:10.3189/2014AoG67A089, 2014.
- Nogi, Y., W. Jokat, K. Kitada, and D. Steinhage, Geological structures inferred from airborne geophysical surveys around Lützow-Holm Bay, East Antarctica, *Precamb. Res.*, 234, 279 – 287, doi:<https://doi.org/10.1016/j.precamres.2013.02.008>, crossing of Neoproterozoic orogens, 2013.
- Paxman, G. J. G., et al., Subglacial Geology and Geomorphology of the Pensacola-Pole Basin, East Antarctica, *Geochem. Geophys. Geosys.*, 20(6), 2786–2807, doi:10.1029/2018GC008126, 2019.
- Raney, K., IceBridge PARIS L2 Ice Thickness. Version 1.0, doi:10.5067/OMEAKG6GIJNB, boulder, Colorado USA: NASA DAAC at the National Snow and Ice Data Center, 2010.
- Riedel, S., W. Jokat, and D. Steinhage, Mapping tectonic provinces with airborne gravity and radar data in Dronning Maud Land, East Antarctica, *Geophys. J. Int.*, 189(1), 414–427, 2012.
- Rignot, E., I. Velicogna, M. R. van den Broeke, A. Monaghan, and J. Lenaerts, Acceleration of the contribution of the Greenland and Antarctic ice sheets to sea level rise, *Geophys. Res. Lett.*, 38, 1–5, doi:10.1029/2011GL046583, 2011.
- Rignot, E., J. Mouginot, B. Scheuchl, M. van den Broeke, M. J. van Wessem, and M. Morlighem, Four decades of Antarctic Ice Sheet mass balance from 1979–2017, *Proc. Natl. Acad. Sci.*, 116(4), 1095–1103, doi:10.1073/pnas.1812883116, 2019.
- Rosier, S. H. R., et al., A New Bathymetry for the Southeastern Filchner-Ronne Ice Shelf: Implications for Modern Oceanographic Processes and Glacial History, *J. Geophys. Res. - Oceans*, 123(7), 4610–4623, doi:10.1029/2018JC013982, 2018.
- Ross, N., et al., Steep reverse bed slope at the grounding line of the Weddell Sea sector in West Antarctica, *Nat. Geosci.*, 5(6), 393–396, doi:10.1038/NGE01468, 2012.
- Seroussi, H., et al., initMIP-Antarctica: an ice sheet model initialization experiment of ISMIP6, *Cryosphere*, 13(5), 1441–1471, doi:10.5194/tc-13-1441-2019, 2019.
- van Wessem, J. M., et al., Modelling the climate and surface mass balance of polar ice sheets using RACMO2: Part 2: Antarctica (1979-2016), *Cryosphere*, 12(4), 1479–1498, doi:10.5194/tc-12-1479-2018, 2018.
- Vaughan, D. G., et al., New boundary conditions for the West Antarctic Ice Sheet: Subglacial topography beneath Pine Island Glacier, *Geophys. Res. Lett.*, 33(9), 1–4, doi:10.1029/2005GL025588, 2006.
- Winter, A., D. Steinhage, T. T. Creyts, T. Kleiner, and O. Eisen, Age stratigraphy in the East Antarctic Ice Sheet inferred from radio-echo sounding horizons, *Earth Syst. Sci. Data*, 11(3), 1069–1081, doi:10.5194/essd-11-1069-2019, 2019.
- Winter, K., N. Ross, F. Ferraccioli, T. A. Jordan, H. F. J. Corr, R. Forsberg, K. Matsuoka, A. V. Olesen, and T. G. Casal, Topographic Steering of Enhanced Ice Flow at the Bottleneck Between East and West Antarctica, *Geophys. Res. Lett.*, 45(10), 4899–4907, doi:10.1029/2018GL077504, 2018.

Young, D. A., D. M. Schroeder, D. D. Blankenship, S. D. Kempf, and E. Quartini, The distribution of basal water between Antarctic subglacial lakes from radar sounding, *Phil. Trans. R. Soc. A*, 374(20140297), doi: 10.1098/rsta.2014.0297, 2016.

Young, N. E., J. P. Briner, Y. Axford, B. Csatho, G. S. Babonis, D. H. Rood, and R. C. Finkel, Response of a marine-terminating Greenland outlet glacier to abrupt cooling 8200 and 9300 years ago, *Geophys. Res. Lett.*, 38, L24701, 1–4, doi:10.1029/2011GL049639, 2011.